LABORATORY FOR SOLID STATE PHYSICS

ETH Zurich
Department of Physics

Annual Report 2009

Eidgenössische Technische Hochschule Zürich
Swiss Federal Institute of Technology Zurich

JAHRESBERICHT
2009

Laboratorium für Festkörperphysik
der
Eidgenössischen Technischen Hochschule
Zürich

PREFACE

The Laboratory for Solid State Physics at ETH Zurich is pleased to present the Annual Report documenting a successful and productive year 2009. In addition to pursuing a the broad range of scientific themes leading to achievments detailed in the report, members of the Laboratory are highly dedicated to teachiing students at all levels: introductory and laboratory courses for physicists and non-physicists alike, advanced and specialty courses and seminars, and hands-on paticipation in research groups. Furthermore, members of the Laboratory continue their service in various other ways to the Physics Department, to ETH as a whole, and to the scientific community.

The Laboratory continues the path of expansion and diversification, and is delighted to welcome Prof. Werner Wegscheider and Prof. Andrey Zheludev. Prof. Wegscheider's research focuses on the production, by molecular-beam-epitaxy, and the study of semiconductor multilayer structures of highest chemical and structural quality. Prof. Zheludev employs neutron scattering techniques to elucidate structural and magnetic properties of condensed matter. In addition to his research at ETH, Prof. Zheludev has also taken on broad responsibilities for neutron scattering at the Paul Scherrer Institute. We wish our new colleagues all the best in their endeavors.

Experimental condensed matter research depends and relies in a critical way on a broad range of support and infractructure. We are very grateful to all the numerous dedicated people in the Laboratory, the Physics Department, and at ETH in general for their expert technical and administrative support.

The solid financial basis for the Laboratory's research and teaching activities continues to be provided by the ETH Schulleitung, which we gratefully acknowledge. We would like to thank also all other sources of financial support, including the Swiss National Science Foundation, KTI, industrial partners, and European programs for research funding.

For preparing this Annual Report, we would like to thank Mr. Ph. Moll, Ms. A. Eisenhut and Prof. L. Degiorgi.

Zürich, May 2010

Der Vorsteher

Bertram Batlogg

Prof. Dr. B. Batlogg

Contents

Chapter 1

Physics of new materials

(http://www.pnm.ethz.ch/)

Head
Prof. Dr. B. Batlogg

Academic Staff
C. Falub
J. Hanselmann
R. Häusermann
W. Kalb
J. Kanter
T. Mathis
P. Moll
H. von Känel
T. Zimmerling

Technical Staff
K. Mattenberger

Administrative Staff
G. Strahm

High Pressure Synthesis

Head
Dr. Janusz Karpinski

Academic Staff
A. Belousov
Dr. Z. Bukowski
Dr. S. Katrych
Dr. N. Zhigadlo

Academic Guests
Dr. Roman Puzniak, Polish Academy of Sciences, Warsaw(Poland)
Dr. Krzysztof Rogacki, Polish Academy of Sciences, Wroclaw(Poland)

1.1 Na_xCoO_2: Reversible Switching Magnetic Ground States by tuning the Coulomb potential background

J. Kanter, Ch. Niedermayer, D. Sheptyakov, V. Wittwer, K. Mattenberger, and B. Batlogg

The sodium cobaltates (Na_xCoO_2) have emerged as an interesting candidate to study correlated electron phenomena. The layered structure of this compound and the mobile dopant ions render Na_xCoO_2 a model system to study a possible coupling between the spatial modulation of electronic states and sodium vacancy orderings. The rich phase diagram as a function of sodium content, including superconductivity (when hydrated), a metal-insulator-transition, one of the highest Seebeck coefficient known, and various magnetic orderings underline the subtle dependence of the Co-O derived electronic states on the sodium concentration. We could show that different sodium orderings can be induced by a defined cooling protocol resulting in distinct magnetic transitions at low temperatures. Neutron scattering experiments, probing the structural differences of the sodium arrangements hinted to a difference in the stacking sequence of sodium vacancies. This is in agreement with studies of precisely controlled sample stoichiometries conducted by Shu *et al.* which could link the inter-plane distance of sodium vacancies to different magnetic transitions.

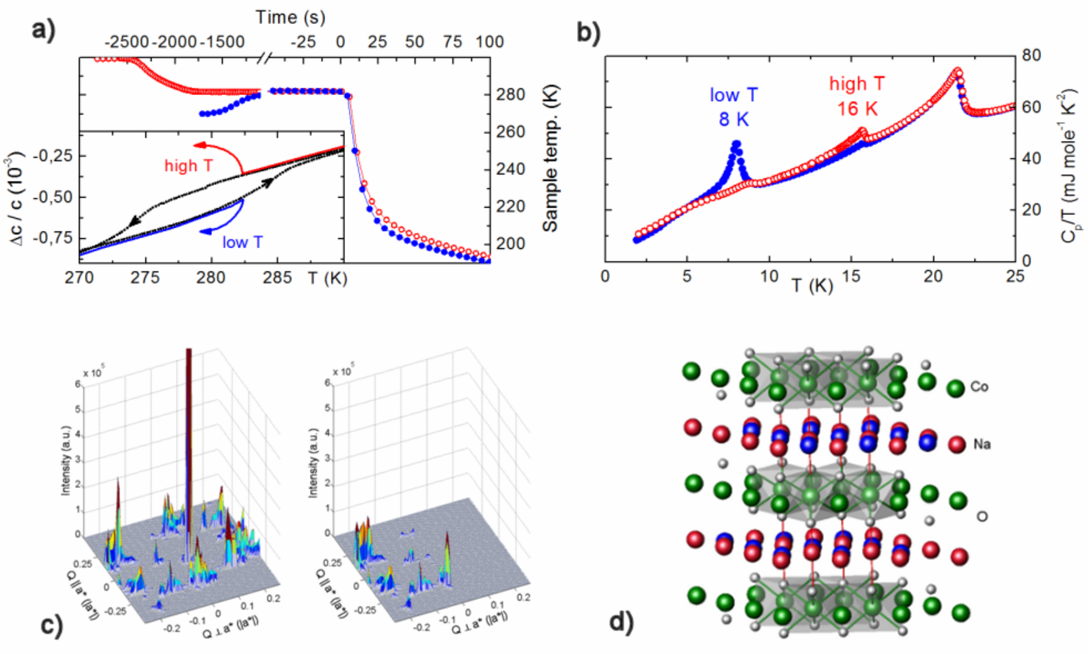

Figure 1.1: **a)** Temperature vs. time of the defined cooling protocol inducing different sodium arrangements. **b)** Distinct magnetic transitions at 8 K and 16 K as a result of the different sodium arrangements. **c)** Neutron scattering data. In the slowly cooled state, a Bragg peak at (009) is visible which is absent in the quenched state, hinting to a higher order in the stacking sequence along the c direction of the crystal. **d)** The layered structure of Na_xCoO2 shows a strong intra-plane sodium ordering due to electrostatic forces but only a weak inter-plane coupling mediated by the buckling of the CoO_2 sheets.

1.2 Near-Isotropy of electronic transport in Iron Pnictide Superconductors

Philip J.W. Moll, Roman Puzniak, Fedor Balakirev, Krzysztof Rogacki, Janusz Karpinski, Nikolai D. Zhigadlo, Bertram Batlogg

We grow single crystals of the recently discovered iron pnictide superconductor SmFeAs(O,F) and study their magnetic and electronic transport properties to assess their potential for applications, most prominently the possible use in high-field magnets. SmFeAs($O_{0.7}F_{0.3}$) single crystals are grown in high pressure and form small ($\approx$ 100 μm in the ab-plane) and very thin ($\approx$ 5-10 μm along the c-axis) platelets. This shape complicates electronic transport experiments, especially perpendicular to the plates, and required the development new contacting techniques. We employ a Focused Ion Beam (FIB) as a powerful tool for shaping and contacting on sub-μm dimensions. A Ga^{2+} ion beam is accelerated by 30 kV and focused onto the target, where it ablates the crystal without collateral damage. In addition to ablation, the FIB is also used to deposit μm-sized electric leads by ion-assisted chemical vapor deposition of Pt contained in a precursor gas.

Figure 1.2 shows a microstructured sample for high precision resistivity measurements. It features bar-shaped legs with a very large geometrical factor $\frac{cross-section}{length}$ 5-35/μm . Due to the high absolute resistance of these long and thin legs (>110 Ω in 4-probe above T_c), measurements on these samples show excellent signal-to-noise ratios, even on the short timescales and rough conditions of a strong magnetic field pulse. To study the materials potential in superconducting applications, high field experiments were performed at the National High Magnetic Field Laboratory (LANL/NHMFL) in pulsed fields up to 65 T. In Figure 1.3, the magnetoresistance of $SmFeAsO_{0.7}F_{0.25}$ is given for field orientations parallel and perpendicular to the c-axis and for current along both orientations. The four panels capture the main qualitative results: The over-all feature and field-scale of the resistive transition is mainly determined by the orientation of the magnetic field with respect to the crystal axes, and is essentially independent of the current direction. At a given temperature, the low dissipation region ('ρ=0') extends to higher magnetic fields when the field is parallel to ab (Right panels of Fig.1.3). Such dependence of the resistivity on the orientation of the magnetic field is typical for layered superconductors, but is least pronounced in the nearly isotropic pnictides.

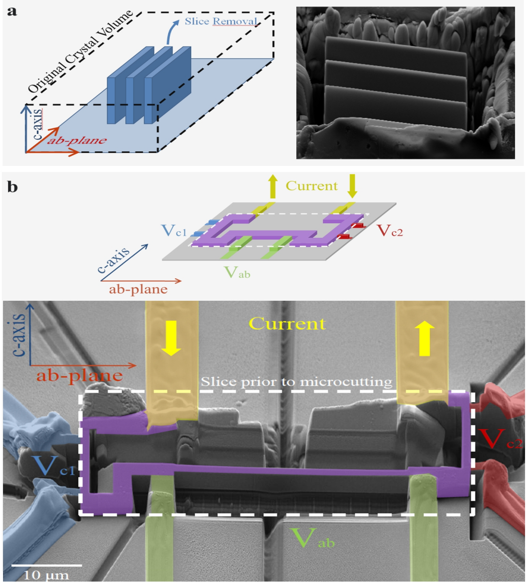

Figure 1.2: A SmFeAs($O_{0.7}F_{0.25}$) crystal before micropatterning b) Lamella after micropatterning: Eight platinum leads are deposited onto the crystal edges (all other colors) that are connected to the resistance bars by narrow (800 nm for c-axis) crystal bridges. Dimensions of resistance bars: length 35 μm (ab-plane), 5 μm (c-axis), cross-section 1.5 μm^2.

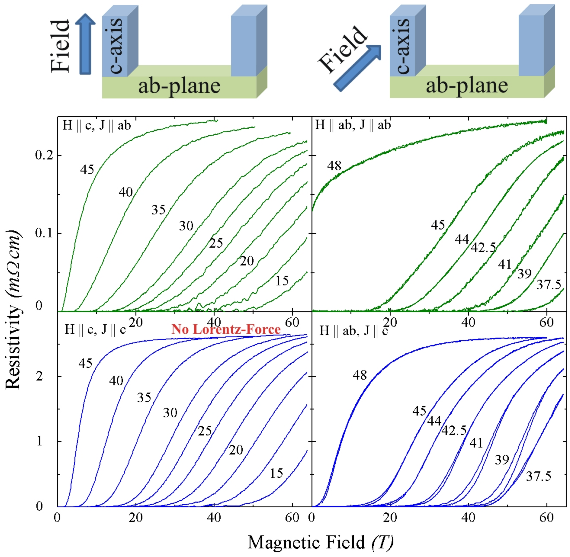

Figure 1.3: The four panels correspond to the various combinations of currents and fields oriented along or perpendicular to the crystallographic c-axis. For the lowest temperatures with j||c, a small hysteresis is observed if the field is applied in the FeAs planes. The hysteretic width depends on the field sweep rate and vanishes at low rates, indicating irreversible vortex trapping.

1.3 High critical current density in SmFeAs($O_{0.7}F_{0.25}$)

Philip J.W. Moll, Roman Puzniak, Fedor Balakirev, Krzysztof Rogacki, Janusz Karpinski, Nikolai D. Zhigadlo, Bertram Batlogg

For applications in superconducting magnets, high critical current densities j_c are required. We found a large, nearly-isotropic intragrain j_c in the range of $10^6 \frac{A}{cm^2}$, employing the following two methods: Direct transport through a small cross-section nanotstructure and magnetization loops M(H) analysis of macroscopic crystals (Bean-Method). In transport, the applied current through a superconducting sample is increased until a potential drop can be observed. Such experiments require extremely large currents for usual cross-sections, and thereby endanger the sample and cause significant heating at the contacts. We have employed the FIB to carve a structure featuring two free-standing nanoscopic bridges out of the same $SmFeAsO_{0.7}F_{0.25}$ single crystal lamella, one bridge along the c-axis and one in the ab-plane (Fig.1.4, cross-section: 608 nm x 768 nm, length 800 nm (c-axis), 566 nm x 860 nm, length 2 μm (ab-plane), 1 Ω contact resistance). This structure enabled us to directly measure current densities up to 1.6 x $10^6 \frac{A}{cm^2}$ without exceeding 7 mA.

The results for j_c from both methods are given in 1.5, and each of them emphasizes different aspects. Starting at low temperature, particularly noteworthy are: (1) j_c exceeds $10^6 \frac{A}{cm^2}$, (2) j_c is essentially independent of the field and only weakly field and current orientation dependent up to 14 T, and (3) the two methods applied to different crystals from different growth runs yield very similar results. The large values of j_c reflect the highly effective pinning in this materials class and give reason to expect that j_c can be further enhanced by proper material design and treatment. Even at the present level, j_c reaches values that are generally considered a minimal requirement for technical applications. Furthermore, the transport measurements directly show that the critical current density $j_c||c$ along the c-axis is very similar to the ab-plane value at lowest temperatures, giving a critical current ratio of $\frac{j_c||c}{j_c||ab} \approx 1.5$. Following these highly promising intra-grain transport properties, grain boundary current suppression and metallurgical issues will have to be addressed.

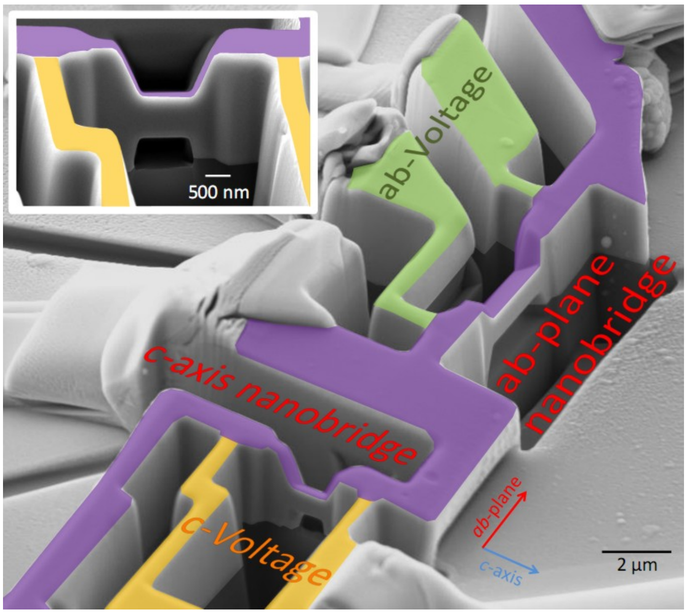

Figure 1.4: Two $SmFeAsO_{0.7}F_{0.25}$ nanobridges (cross-section 600 nm x 600 nm, length of narrow part 1 - 3 μm) cut into a single crystal lamella for direct measurements of critical currents j_c along different axes(similar to Fig. 1.2).

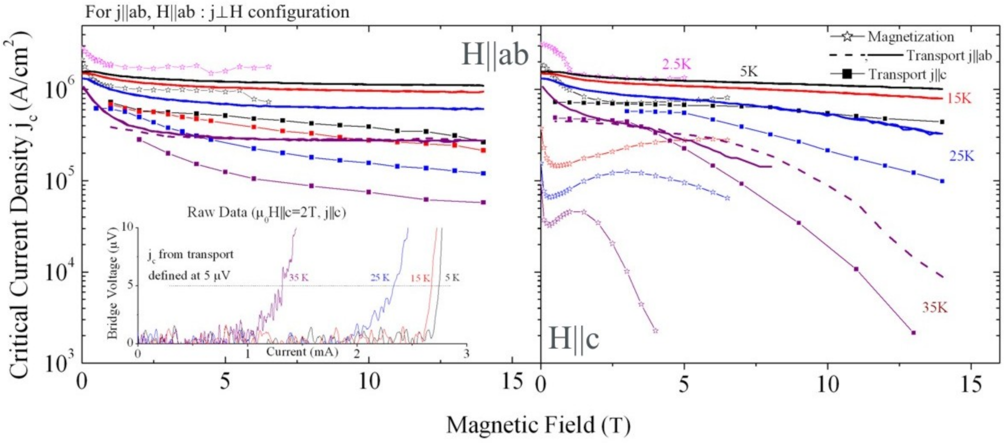

Figure 1.5: Critical current density of $SmFeAsO_{0.7}F_{0.25}$ determined from magnetic hysteresis loops and from direct critical transport experiments across the nanobridge shown in Fig.1.4

1.4 Calculating the trap density of states in organic field-effect transistors from experiment: A comparison of different methods

W. L. Kalb and B. Batlogg

World-wide research on organic field-effect transistors is at a high level as this new technology is poised to enter the market. The transistor parameters and stability of organic field-effect transistors are intimately related to the efficiency of the charge transport mechanism and the extend of charge carrier trapping in extrinsic traps. Field-effect transistors can be used to determine the underlying spectral density of localized states in the band gap, i.e. the trap densities as a function of energy (trap DOS).

In order to eventually clarify the microscopic origin of charge carrier traps in organic field-effect transistors, it is highly desirable to quantitatively compare trap DOS data from various experiments and from various research groups. However, several different methods have been used to calculate the trap DOS from transfer characteristics of organic field-effect transistors. Consequently, an important prerequisite for a systematic comparison of trap DOS data in the literature is to test if the different calculation methods lead to comparable results.

The trap DOS was thus determined with a pentacene-based thin-film transistor from measurements of the temperature dependence and gate-voltage dependence of the contact-corrected field-effect conductivity. Several analytical methods to calculate the trap DOS from the measured data were used. We also used computer simulations to further test the results from the analytical methods. Most methods predict a trap DOS close to the valence band edge that can be very well approximated by a single exponential function with a slope in the range of $50 - 60\,\mathrm{meV}$ and a trap density at the valence band edge of $\approx 2 \times 10^{21}\,\mathrm{eV}^{-1}\mathrm{cm}^{-3}$. Interestingly, the trap DOS is always slightly steeper than exponential. An important finding is that the choice of the method to calculate the trap DOS from the measured data can have a considerable effect on the final result. We identify two specific simplifying assumptions that lead to significant errors in the trap DOS. The temperature-dependence of the band mobility should generally not be neglected. Moreover, the assumption of a constant effective accumulation layer thickness leads to a significant underestimation of the slope of the trap DOS.

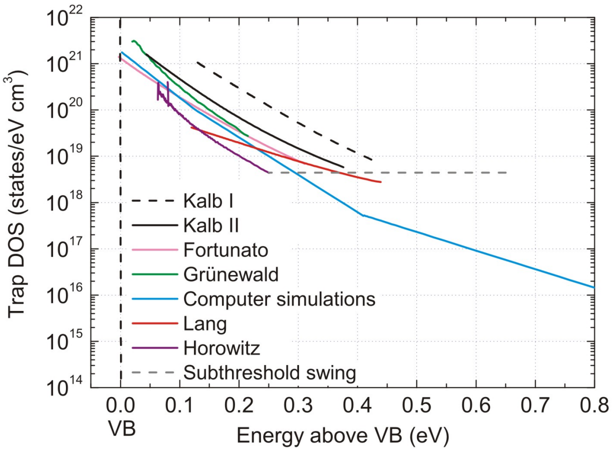

Figure 1.6: Spectral density of localized states in the band gap of pentacene (trap DOS) as calculated with several methods from the same set of measured transistor characteristics. The energy is relative to the valence band edge (VB). The estimate from the subthreshold swing (dashed grey line) assumes the trap DOS not to depend on energy and can only be regarded as a rough estimate for the traps slightly above the Fermi energy. All other methods result in a trap DOS that increases slightly faster than exponentially with energy. The choice of the method to calculate the trap DOS has a considerable effect on the final result.

1.5 The trap DOS in small molecule organic semiconductors: A quantitative comparison of thin-film transistors with single crystals

W. L. Kalb, S. Haas, C. Krellner, T. Mathis and B. Batlogg

Organic semiconductors are envisioned to revolutionize display and lighting technology. To support a sustainable market entry, however, it is important to further deepen the understanding of organic semiconductors and organic semiconductor devices. Electronic trap states in organic semiconductors severely affect the performance of such devices.

In order to help clarify the microscopic origin of charge carrier traps in organic semiconductors we compared the spectral density of localized states in the band gap (trap DOS) in various samples of small molecule organic semiconductors including thin-film transistors (TFT's) where the active layer generally is polycrstalline and organic single crystal field-effect transistors (SC-FET's). These data are also compared with the trap DOS in the bulk of single crystals made of small molecule semiconductors as derived from space-charge-limited-current measurements. Trap DOS data were taken from publications and we also add to the compilation unpublished data from experiments in our laboratory.

The compilation shows that it is possible to reach one of the ultimate goals of organic electronics: producing organic field-effect transistors with trap densities as low as in the bulk of single crystals. Moreover, the collection of all data strongly suggests that structural defects associated with grain boundaries are the main cause of "fast" hole traps in TFT's made with vacuum-evaporated pentacene. For high-performance transistors made with small molecule semiconductors such as rubrene the chemistry of the gate dielectric's surface and in particular water adsorbed on the gate dielectric surface and it is essential to reduce this cause by employing a suitable gate dielctric. In samples with very low trap densities, we sometimes observe a steep increase of the trap DOS very close ($< 0.15\,\mathrm{eV}$) to the mobility edge with a characteristic slope of $10-20\,\mathrm{meV}$. This may be due to band broadening due to the thermal fluctuation of the intermolecular transfer integral, i.e. the thermal motion of the molecules is reflected in this steep increase of the trap DOS close to the mobility edge. Moreover, the trap DOS in TFT's with small molecule semiconductors is very similar to the trap DOS in hydrogenated amorphous silicon even though polycrystalline films of small molecules with van der Waals-type interaction on the one hand are compared with covalently bound amorphous silicon on the other hand.

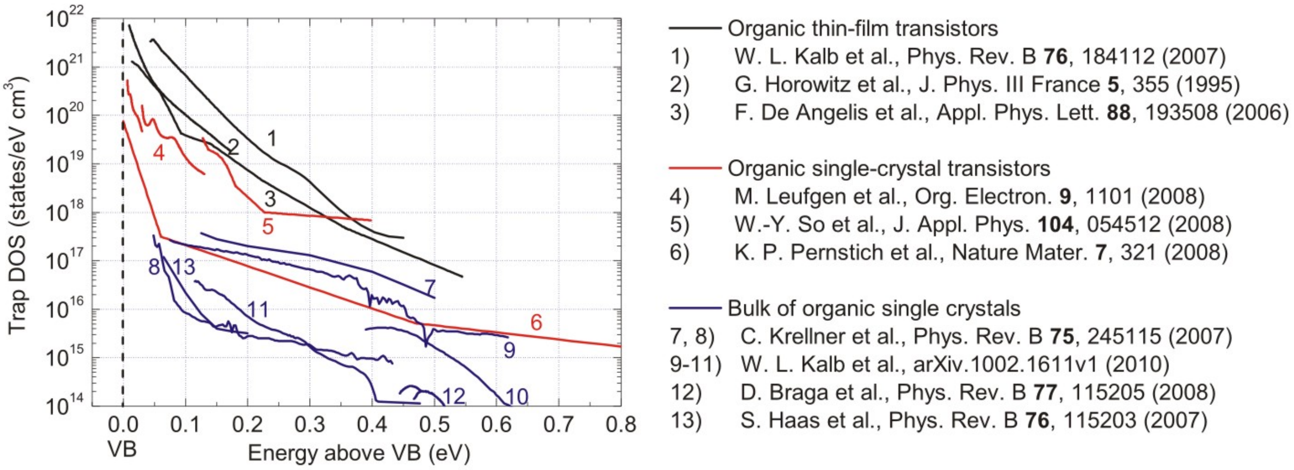

Figure 1.7: Representative trap DOS data in small molecule organic semiconductors from TFT's (black lines), SC-FET's (red lines) and in the bulk of single crystals (blue lines) as taken from the literature. The trap densities from SC-FET's can be much lower than the trap densities from the best TFT's. The trap densities in the bulk of single crystals are typically lower than the trap densities from SC-FET's. Importantly, if a Cytop^{TM} fluoropolymer gate dielectric is used, bulk trap densities can be reached in organic field-effect transistors made with small molecule semiconductors. Thus, water adsorbed on the gate dielectric appears to be the dominant cause of traps if the semiconductor has a low density of traps due to structural defects (e.g. single crystals). A steep increase of the trap DOS very close to the valence band edge ($< 0.15\,\mathrm{eV}$) can sometimes be observed (data no. 2, 6, 8, 13). These states are attributed to the thermal fluctuations of the intermolecular transfer integral.

1.6 Organic single crystal growth and characterization

Tino Zimmerling

Organic electronics is a rapidly growing technology. New cellphones featuring displays based on organic light emitting diode (OLED) displays are probably only the first of many commercial applications in the near future. A key to advance the development of this technology is a better understanding of the underlying physics of organic materials. Single crystals are well suited to investigate intrinsic material properties, as they have the lowest trap density possible, that is, fewer structural defects and impurities. We grow single crystals from different source materials by means of physical vapor transport: The source material sublimes and is subsequently transported by a controlled gas flow from the hot sublimation region to a colder region where it recrystallizes, resulting in crystals of different sizes and shapes.

By sandwiching such a crystal between two electrodes, it is possible to investigate the physics of charge transport and the trap distribution in these crystals by means of space-charge-limited current (SCLC) measurements, for instance. In addition, transistors based on single crystals allow us to investigate interface effects between different device layers. Thin crystals of the order of 1μm are well suited for various experiments such as SCLC measurements. These crystals have less structural defects and impurities giving rise to a very low trap density and high charge carrier mobilities.

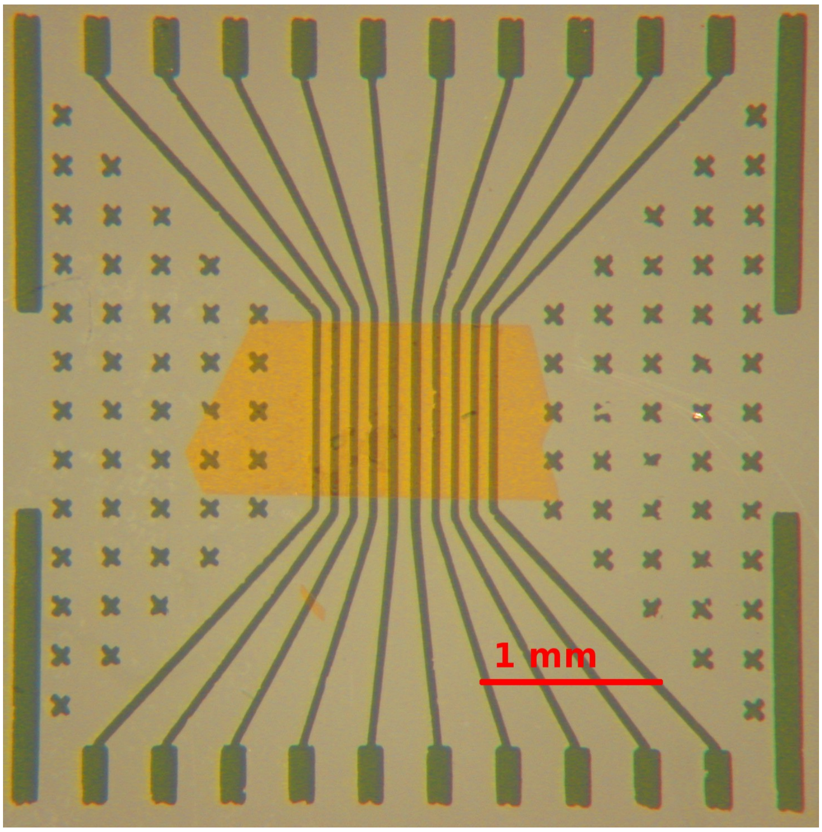

Figure 1.8: Rubrene single crystal on top of bottom gold contacts before the top contact is applied.

1.7 Low-voltage organic transistors and inverters with ultra-thin fluoropolymer gate dielectric

Mathias Walser, Thomas Mathis, Wolfgang Kalb, Bertram Batlogg

We succeeded in the fabrication of hysteresis-free and electrically stable organic field-effect transistors (OFETs) and inverters operating at voltages $<$ 1-2V, enabled by the almost trap-free interface between the organic semiconductor and an ultra-thin ($<$20 nm) and highly insulating single layer fluoropolymer gate dielectric (Cytop). OFETs with PTCDI-C13 (N,N'-ditridecylperylene-3,4,9,10-tetracarboxylicdiimide) as semiconductor exhibit outstanding transistor characteristics: very low threshold voltage (0.2V), onset at 0V, steep sub threshold swing (0.1-0.2V/decade), no hysteresis and excellent stability against gate bias stress. Particularly noteworthy is the fact that such small OFET operating voltages can be achieved with the relatively simple processing techniques used in fabricating this device.

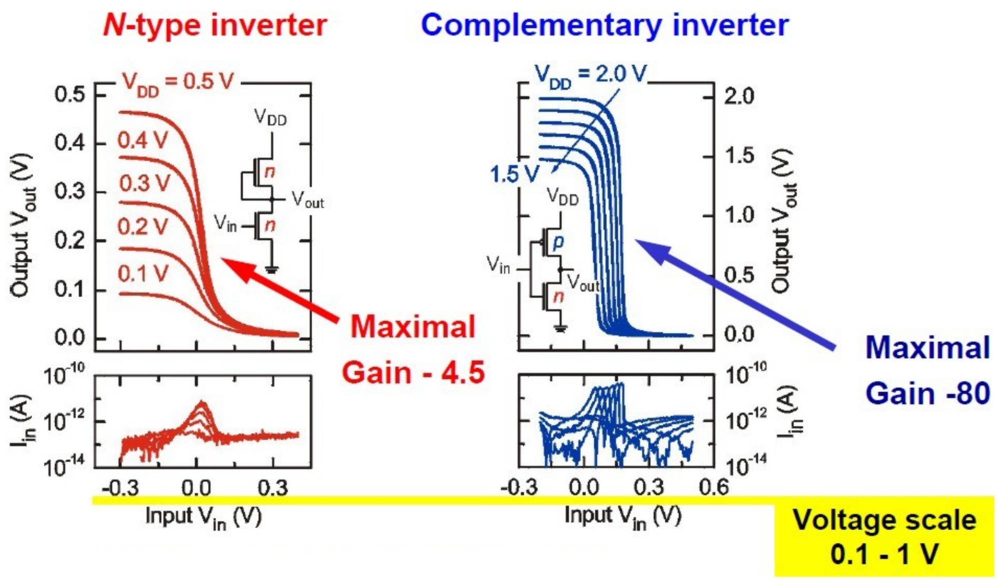

Figure 1.9: Inverters with ultra-thin flouropolymere gate dielectric, leading to very low operating voltage.

1.8 Superconductivity above 50 K in Th-substituted SmFeAsO

Nikolai Zhigadlo, Sergiy Katrych, Stephen Weyeneth, Roman Puzniak, Philip Moll, Zbigniew Bukowski, Janusz Karpinski, Hugo Keller, Bertram Batlogg

Superconducting poly- and single-crystalline samples of the $Sm_{1-x}Th_xFeAsO$ with partial substitution of Sm^{3+} by Th^{4+} with a sharp diamagnetic onset at T_c up to 53 K were synthesized using high pressure technique. The samples are characterized by a full diamagnetic response in low magnetic field, by a high intergrain critical current density for polycrystalline samples, and by critical current density of the order of 8 x 10^5 A/cm^2 for single crystals at 2 K in 7 T. It was found that the magnetic penetration depth anisotropy γ_λ exhibits a pronounced increase with decreasing temperature, in agreement with the already reported behavior for single crystals of $SmFeAsO_{1-x}F_y$. A Focus Ion Beam (FIB) based contacting method was employed to contact (Sm,Th)FeAsO single crystals. The inset in upper panel of Fig. 1.10 shows a typical cooldown curve.

The resistivity in zero field decreases by a factor of 3.7 from room temperature upon cooling down to T_c (onset - 49.7 K; 50% - 48.9 K; zero - 47.4 K), defining the so-called resistivity ratio of the sample studied. From this data, the

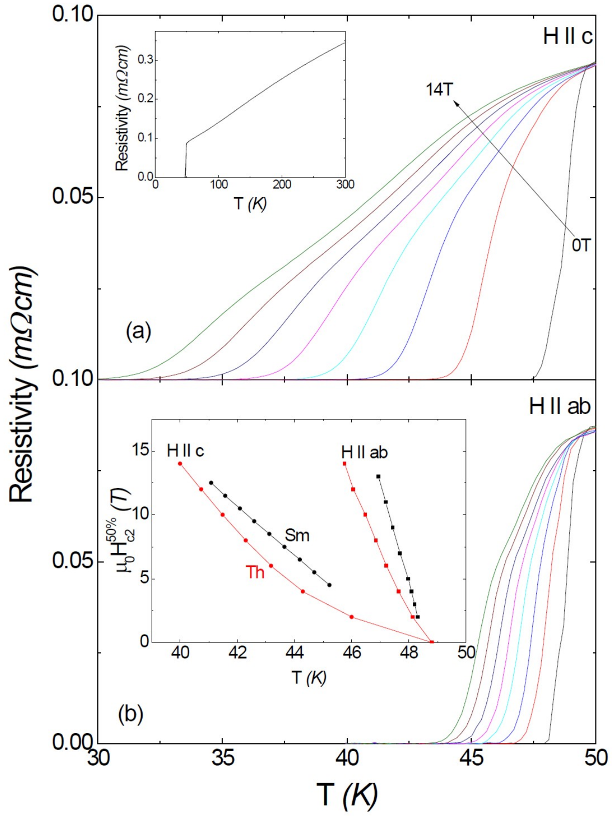

Figure 1.10: Temperature dependences of the resistivity for (Sm,Th)FeAsO single crystal measured with the field applied parallel to the (Fe$_2$As$_2$) layers (H||ab) (a) and perpendicular to them (H||c) (b) at various magnetic fields from 0 to 14 T. Inset of (a) shows the resistivity in the temperature range of 2 - 300 K. Inset of (b) shows the temperature dependence of the upper critical field with H||ab and H||c for the (Sm,Th)FeAsO system. To determine H$_{c2}$ the 50% ρ_n criterion was used. For comparison data for SmFeAs(O,F) crystal are presented (marked with Sm).

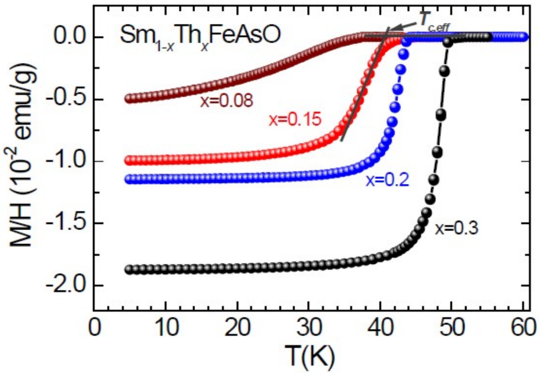

Figure 1.11: Temperature dependence of the magnetic susceptibility for Sm$_{1-x}$Th$_x$FeAsO samples measured at 0.5 mT in zero-field-cooled (ZFC) mode. The determination of T$_{c,eff}$ is illustrated.

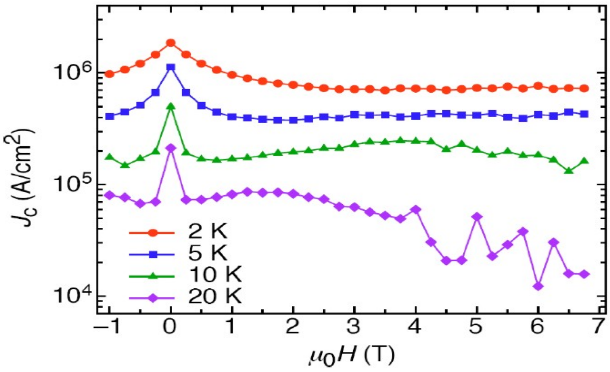

Figure 1.12: Critical current density of a Sm$_{0.89}$Th$_{0.11}$FeAsO single crystal calculated from the width of the hysteresis loops.

upper critical field was estimated, defined as the magnetic field, where 50% of the resistivity is suppressed (see inset in lower panel of Fig. 1.10).

1.9 Superconductivity in SmFe(As,P)O

Nikolai Zhigadlo, Janusz Karpinski

Polycrystalline samples and single crystals of SmFeAs$_{1-x}$P$_x$O were synthesized using high-pressure techniques. Figure 1.13 shows the temperature dependence of the magnetic susceptibility of SmFeAs$_{1-x}$P$_x$O polycrystalline samples in a magnetic field of 10 Oe. Polycrystalline samples with x = 0.5 and 0.45 show bulk superconductivity with a superconducting transition at $\approx$ 23 and 18 K, respectively. Single crystals of P substituted SmFeAsO (T_c = 17K) were also grown using NaCl/KCl as a flux. Though conditions of crystal growth and doping still require further optimization we have grown crystals with a size of 100x100 μm^2 and refined composition SmFeAs$_{0.66}$P$_{0.34}$O. Fig. 1.14 displays the temperature dependence of electrical resistivity ρ of a polycrystalline sample of SmFeAs$_{0.5}$P$_{0.5}$O. The transition is rather sharp, suggesting a homogeneous. Fig. 1.14 right Inset shows the resistive measurements at various magnetic field strengths. The Left Inset of Fig. 1.14 shows the temperature dependence of the upper critical field calculated using the 50% ρ_n criterion.

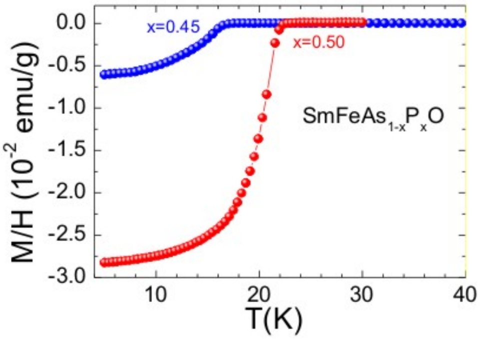

Figure 1.13: Temperature dependence of the magnetic susceptibility for SmFeAs$_{1-x}$P$_x$O samples measured at 1 mT in zero-field-cooled (ZFC) mode.

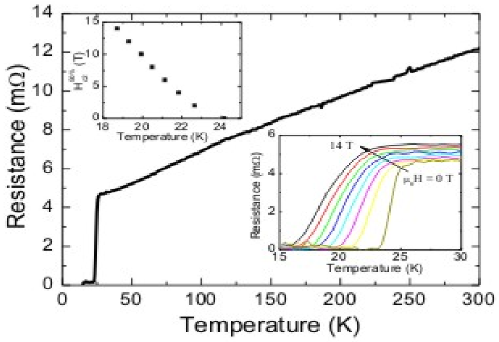

Figure 1.14: Temperature dependence of electrical resistivity of SmFeAs$_{0.5}$P$_{0.5}$O polycrystalline sample. The Right Inset shows the resistive measurements at various magnetic field strengths. The Left Inset shows the temperature dependence of the upper critical field.

1.10 First attempt to grow SmFeAsO single crystals from NaAs flux

Sergiy Katrych, Janusz Karpinski, Nikolai Zhigadlo

In order to increase the size and surface quality of LnFeAsO type single crystals, different kind of fluxes were investigated. Preliminary single crystal growth experiments show that the NaAs flux could be a good candidate for increasing the size and x-ray quality of 1111 single crystals. First grown single crystals were studied on a four-circle diffractometer equipped with CCD detector. Structure investigation confirmed high structural perfection with very low mosaicity (less than 1 degree) in c direction. Further experiments are in the progress. Fig. 1.15 shows as grown superconducting Sm1111 crystals.

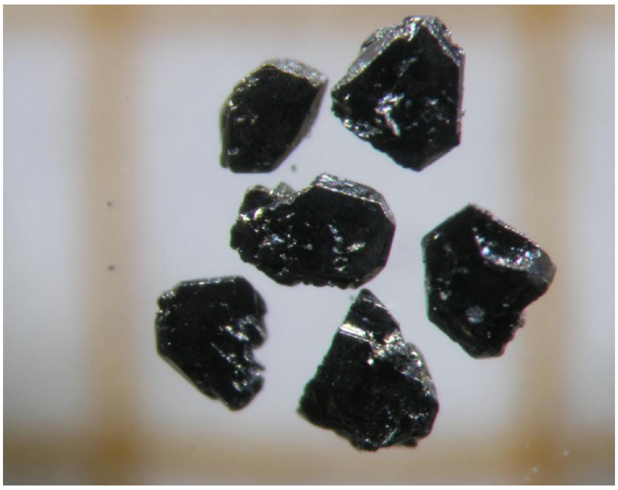

Figure 1.15: First single crystals of Sm1111 grown from NaAs flux at 1380 C within 40 h (on mm scale).

1.11 Single crystals of $CaFe_{2-x}Co_xAs_2$ and $EuFe_{2-x}Co_xAs_2$

Zbigniew Bukowski

Single crystals of pure $CaFe_2As_2$, $EuFe_2As_2$ and Co substituted $CaFe_{2-x}Co_xAs_2$ and $EuFe_{2-x}Co_xAs_2$ were grown out of Sn flux in alumina crucibles sealed under reduced Ar pressure in quartz ampoules. Typical crystals were of plate-like shape with the crystallographic c-axis perpendicular to the plate of a size up to 7x5 mm^2 (Fig 1.16). An interesting feature of $EuFe_2As_2$ is an antiferromagnetic ordering of magnetic moments localized on Eu^{+2} ions (T_N = 18 K). This ordering is not affected by Co substitution. Magnetization and resistivity data for $EuFe_{2-x}Co_xAs_2$ show suppression of the SDW state with Co substitution and finally the appearance of superconductivity (Fig. 1.16). The effect of Eu^{+2} magnetic ordering on superconductivity leads to the re-entrant behaviour. Magnetization and resistivity measurements of $CaFe_{2-x}Co_xAs_2$ single crystals show that the SDW transition in is gradually suppressed by Co doping leading to superconductivity at x=0.08 (Fig. 1.17). Undoped $CaFe_2As_2$ revealed a substantial increase of the Nernst coefficient and Seebeck coefficient in the SDW state.

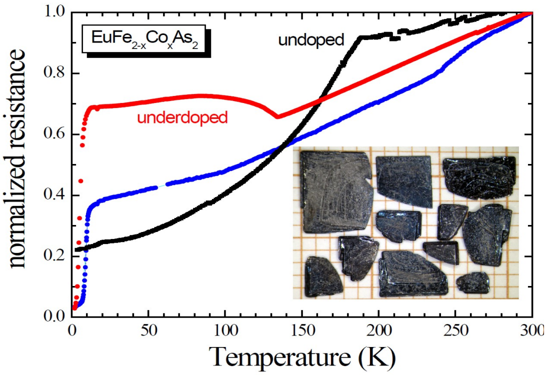

Figure 1.16: Temperature dependence of the resistance for $EuFe_{2-x}Co_xAs_2$ single crystals. Inset shows single crystals of $EuFe_2As_2$.

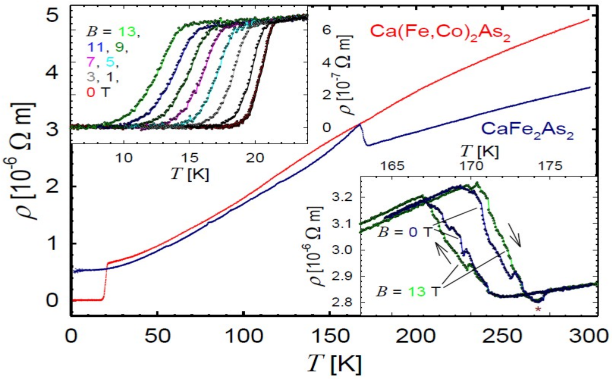

Figure 1.17: Temperature dependence of resistivity for $CaFe_{2-x}Co_xAs_2$ single crystals.

Chapter 2

Physics of semiconductor nanostructures

(http://www.nanophys.ethz.ch)

Head
Prof. Dr. Klaus Ensslin
Prof. Dr. Thomas Ihn
Prof. Dr. Rene Monnier

Academic Staff
Dr. Ilona Blatter
Theodore Choi
Dr. Miklos Csontos
Susanne Dröscher
Tobias Frey
Urszula Gasser
Johannes Güttinger
Sarah Hellmüller
Magdalena Hüfner
Dr. Clemens Rössler
Yashar Komijani
Bruno Küng
Francoise Molitor
Thomas Müller
Dr. Preden Roulleau
Arnhild Jacobsen
Stephan Schnez
Dr. Christoph Stampfer
Matthias Studer

Technical Staff
Cecil Barengo
Paul Studerus

Academic Guests
Prof. Dr. Thomas Heinzel, Universität Düsseldorf, Germany (1.10.2008-31.3.2009)
Prof. Dr. Yigal Meir, Ben Gurion University, Israel (1.4.2009-2.4.2009)
Takuya Noguchi, University of Tokyo, Japan (2.11.2009-31.1.2010)

Administrative Staff
Claudia Vinzens

2.1 Transport gap in graphene constrictions

F. Molitor, A. Jacobsen, C. Stampfer, J. Güttinger, T. Ihn, and K. Ensslin

Graphene has unique electronic properties due to its special band structure and Dirac-type behavior of the electronic quasiparticles. However, this specific structure has one main drawback: because of the absence of a band gap and the prediction of Klein tunneling, it is difficult to confine carriers electrostatically. Recently this problem has been overcome by cutting a graphene flake into narrow ribbons, which has been shown to open a gate voltage region of suppressed conductance, called transport gap. This method can be used to confine carriers in quantum dots. However, even if by now graphene constrictions are regularly used in combination with quantum dots, either to form the tunnel barriers or as a charge readout detector, the origin of the formation of the transport gap is still not well understood.

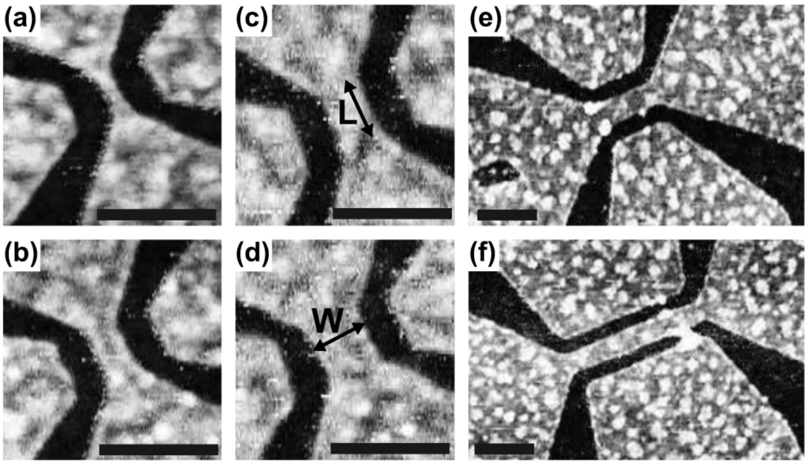

Figure 2.1: Scanning force micrographs of several constrictions. The length of the scale bars is 200 nm. The dimensions are the following: (a) W=30 nm and L=100 nm, (b) W=65 nm and L=100 nm, (c) W=75 nm and L=100 nm, (d) W=100 nm and L=100 nm, (e) W=85 nm and L=200 nm, and (f) W=85 nm and L=500 nm.

Figure 2.1 displays scanning force micrographs of several graphene constrictions. The graphene flakes are produced by mechanical exfoliation of graphite and deposition on a highly doped Si substrate covered with 295 nm of silicon dioxide. Raman spectroscopy is used in order to confirm the single-layer nature of the flakes. The structure is defined by electron-beam lithography followed by reactive ion etching. Finally, contacts are added using a second electron-beam lithography step and Cr/Au evaporation. Each structure consists of source and drain leads connected by the constriction and has two lateral side gates located $\approx$ 50 nm from the constriction. Structures (a)-(d) from Fig. 2.1 have the same constriction length, but different widths, and are etched out of the same graphene flake. Structures (e) and (f) have the same width and different lengths and originate from a second flake on the same substrate.

Figure 2.2(a) shows the conductance through the W =85 nm and L=500 nm constriction as a function of applied back-gate voltage. Around V$_{BG}$ $\approx$0 V, there is a region of strongly suppressed conductance, the so-called transport gap. However, it is not a real energy gap because it is full of sharp resonances. The size of this transport gap in back-gate voltage can be quantified by the procedure shown in Fig. 2.2(b). The conductance trace is smoothened over a back-gate voltage range large enough to eliminate the resonances without affecting the general shape. The regions of a linear increase in conductance at both sides of the transport gap are selected by hand and a linear fit is performed (black lines). The gap size in back-gate voltage is then defined as the distance between the intersection points of the fitted traces with the G = 0 line (V$_{gap,BG}$= 3.4 V). This is a reasonable approach since the conductance values are much smaller than the minimal conductivity observed for extended graphene systems which is on the order of $4e^2/h$.

Figure 2.2(c) displays the conductance as a function of V$_{bias}$ and V$_{BG}$. A region of suppressed conductance can again be observed, with an extension E_{gap}/e in V_{bias} direction and V$_{gap,BG}$ along the direction of V$_{BG}$. By recording a higher-resolution measurement of the region where the transport gap is most pronounced, Figure 2.2(d), one can see that the region of suppressed conductance is composed of individual diamonds, which are sometimes overlapping as

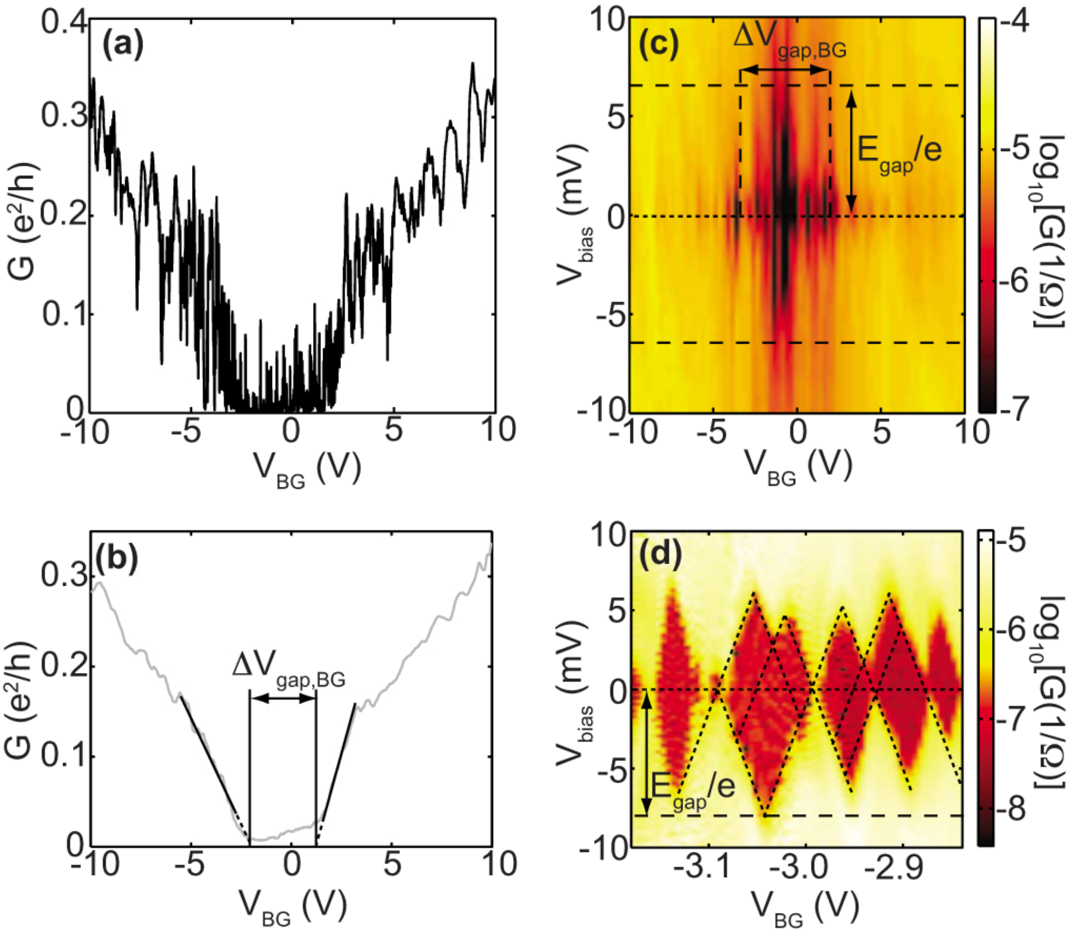

Figure 2.2: Transport gap measurements for the constriction with dimensions W=85 nm and L=500 nm. (a) Conductance versus back-gate voltage V_{BG}. The measurement is performed with a bias voltage of 300 μ V. (b) Procedure used to determine the size of the transport gap in back-gate voltage Vgap,BG. The trace from (a) is smoothened over 2.5 V in V_{BG}. The black lines indicate the linear fits used to determine the gap size. (c) Conductance as a function of applied back-gate and bias voltages. (d) Zoom of the gap measured in (c).

in the case of statistical Coulomb blockade. We establish a way to describe the transport gap by its width in back-gate voltage and compare it to the usual measurements of the conductance as a function of bias and back-gate voltages for different constriction geometries. This method is used to study the effect of an applied side-gate voltage on the transport gap formed in a constriction. We find that in the case of a voltage applied to both side gates, there is still a region of reduced conductance, but the conductance is no longer completely suppressed. In the presence of a high enough magnetic field, we observe the formation of Landau levels in the constriction.

2.2 Electron-Hole Crossover in Graphene Quantum Dots

J. Güttinger, C. Stampfer, T. Frey, T. Ihn, and K. Ensslin; in collaboration with F. Libisch and J. Burgdörfer, TU Vienna

It is an important goal in quantum-dot physics to understand the quantum mechanical energy spectra and the corresponding orbital and spin states of these man-made artificial atoms. This knowledge is necessary for designing and operating quantum dots in regimes relevant for particular applications, for example, for the implementation of qubits. It has been shown in various material systems that usually the measured spectra can only be easily understood, and related to theoretical models, in the few-electron (or hole) limit.

The 50 nm wide and 80 nm long quantum dot [scanning force microscope image, Fig. 2.3(a)] is connected to source (S) and drain (D) via two 25 nm wide and 10 nm long constrictions, acting as tunneling barriers [Fig. 2.3(b)]. The dot and the leads can be tuned by an in-plane graphene plunger gate (PG) and the highly doped silicon substrate is used as a back gate (BG).

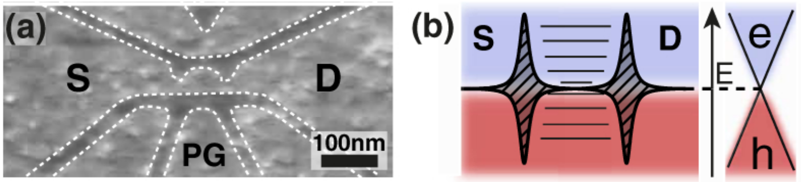

Figure 2.3: (a) Scanning force microscope image of the graphene quantum dot device with source (S) and drain (D) leads, and lateral plunger gate (PG). (b) Schematic level structure of the QD device highlighting the constriction induced tunneling barriers and the electron-hole crossover.

About 50 Coulomb resonances as a function of a magnetic field B perpendicular to the sample plane were investigated. We tune from hole to electron transport since we cover the whole transport gap [see bottom of Fig. 2.4]. The evolution of Coulomb resonances in perpendicular magnetic field shows a common trend at lower PG voltages to bend for increasing B field towards higher energies (higher Vpg). In contrast, we find for higher PG voltage regimes the opposite trend, where resonances tend to shift to lower energies for increasing B field.

To elucidate the evolution of the Coulomb resonances with magnetic field, numerical calculations of the eigenenergies of a graphene QD in a perpendicular B field are performed [see top of Fig. 2.4]. We use a third-nearest neighbor tight-binding approximation to simulate a 50x80 nm graphene QD containing 150 000 carbon atoms. The magnetic field is included by a Peierls phase factor. To eliminate contributions from edge states localized at the zigzag-boundaries an on-site potential of 2 eV on all carbon atoms with dangling bonds is employed.

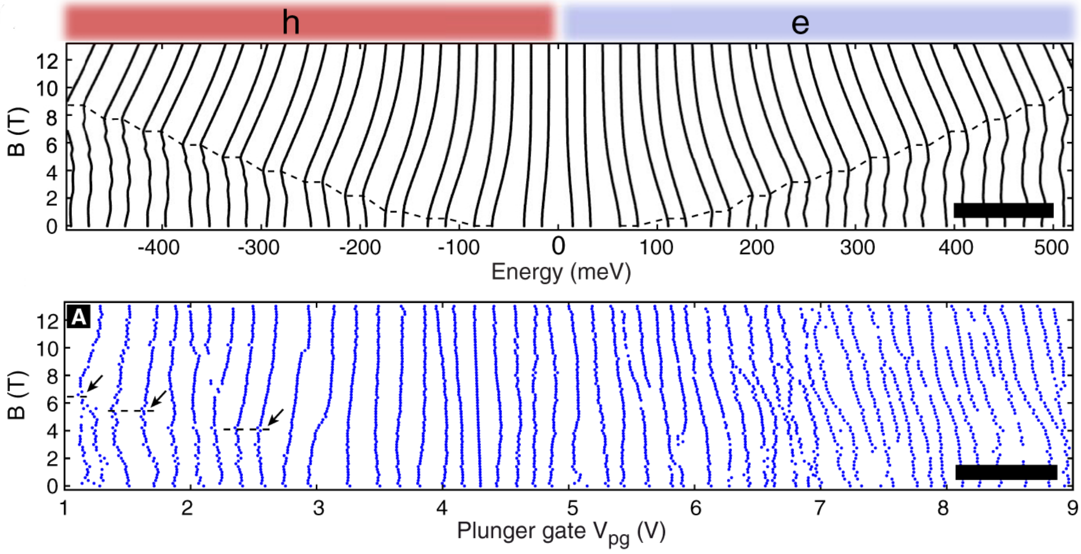

Figure 2.4: Top: Calculated quantum dot level position where spin, Zeeman splitting and a constant charging energy of 18 meV are included. Bottom: Experimental data. The peak positions are extracted from Coulomb blockade measurements. The scale bar corresponds to 100 meV.

Detailed studies of the electron-hole crossover in the addition spectrum of a graphene quantum dot in a perpendicular magnetic field have been performed. We observe unique features in the evolution of the spectrum as a function of the magnetic field of both the linear dispersion and of the edge confinement of the graphene QD. One prominent example is the development of the graphene specific E=0 Landau level around the charge neutrality point. The overall tendency of states converging towards the zero-energy Landau level is accompanied by kinks which we attribute to crossings with higher Landau levels. Coulomb diamond measurements in this transition regime show a rich spectrum of excited states and cotunneling. These measurements open the way for more detailed studies of the electron-hole transition including a better understanding of the addition spectra and spin states in graphene quantum dots.

2.3 Transport through graphene double dots

F. Molitor, S. Dröscher, J. Güttinger, A. Jacobsen, C. Stampfer, T. Ihn, and K. Ensslin

The control of individual electrons and spins has been achieved in semiconductor quantum dots. Graphene as a material system lends itself for small and well controlled quantum systems with the additional possible benefit of increased spin coherence times. Controlled coupling of quantum dots is a prerequisite for the envisioned implementation of spin qubits in such systems. An important ingredient is the observation of Coulomb blockade of a graphene double dot system.

Figure 2.5 (a) shows a scanning force micrograph of the double dot structure. The structure consists of two central graphene islands forming the dots labeled L and R in Fig. 2.5 (a). They are mutually connected by a 30 nm wide constriction. Each dot has a diameter of about 90 nm. The dots are connected by 20 nm wide constrictions to source and drain contacts. In addition to the doped substrate, which acts as a global back gate, there are five graphene in-plane gates allowing to fine tune the structure. The gates GL and GR can be used to change the number of carriers in the dots, while the gates CL, CR, and GC are used to tune the transmission of the constrictions and the coupling between the dots.

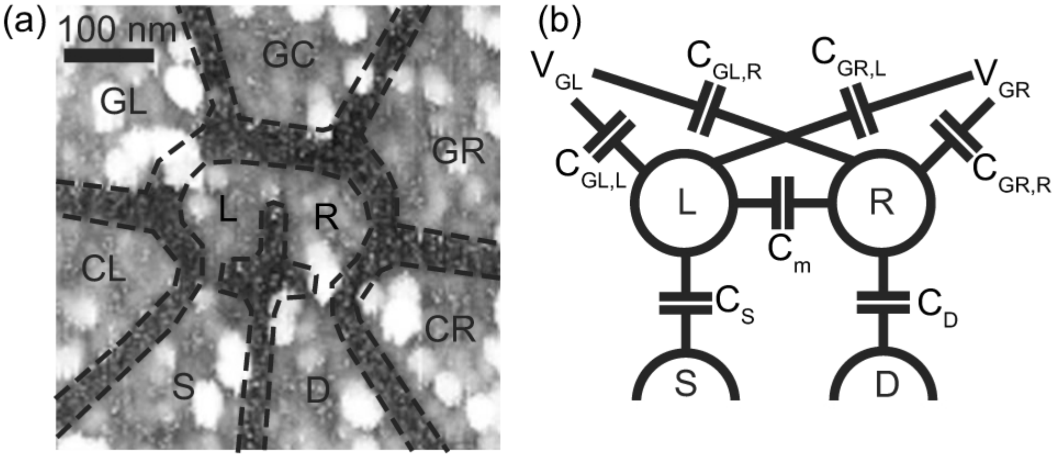

Figure 2.5: (a) Scanning force microscope image of the graphene quantum dot device with source (S) and drain (D) leads, and lateral plunger gate (PG). (b) Schematic level structure of the QD device highlighting the constriction induced tunneling barriers and the electron-hole crossover.

Figure 2.6 shows a measurement of the current through the double dot as a function of the voltages applied to gates GR and GL. The honeycomb pattern characteristic for the charge stability diagram of a double dot can be observed. Elastic transport through the double dot is only possible in the case where the electrochemical potentials in both dots are aligned mutually and with the Fermi energy in the leads. This is the case at the so-called triple points in the corners of the hexagons of constant charge configuration. The current is displayed on a logarithmic scale making the connecting lines between the triple points visible. Along these lines, only one of the dot levels is aligned with the Fermi energy in the leads, leading to current by cotunneling processes. The current through the edges of the hexagons can be suppressed by changing the voltages applied to gates CL and CR in such a way that the barriers are less transparent.

The coupling between both dots, as well as the transmission of the constrictions connecting the dots to the leads, can be tuned by graphene in-plane gates. We have shown that the coupling between the dots is a non-monotonic function of the applied gate voltage. Finally, a model of purely capacitively coupled dots allowed to extract the relevant energy scales of the system. The presented results may be seen as a promising development toward the realization of spin qubits in graphene.

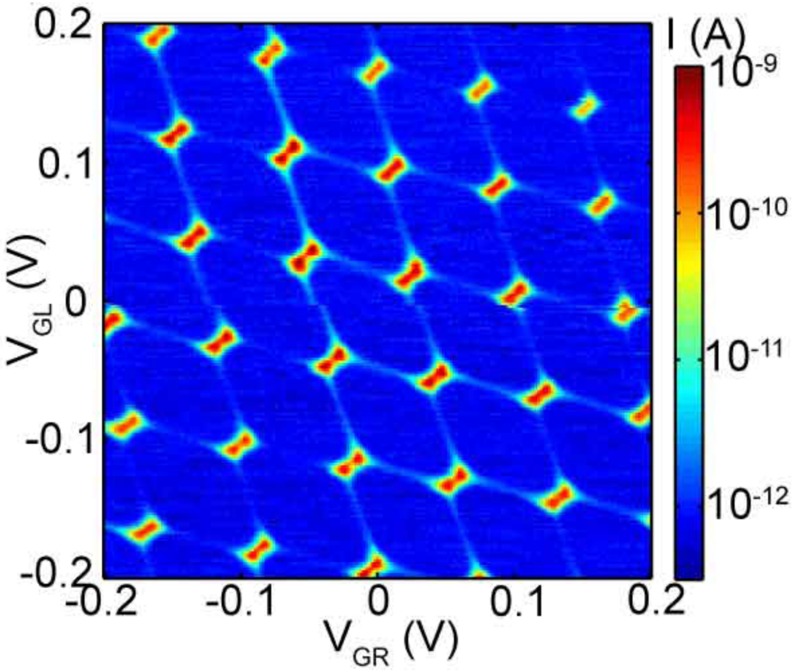

Figure 2.6: Current through the double dot as a function of the voltages VGR and VGL.

2.4 Aharonov-Bohm effect in a side-gated graphene ring

M. Huefner, F. Molitor, A. Jacobsen, A. Pioda, C. Stampfer, K. Ensslin and T. Ihn

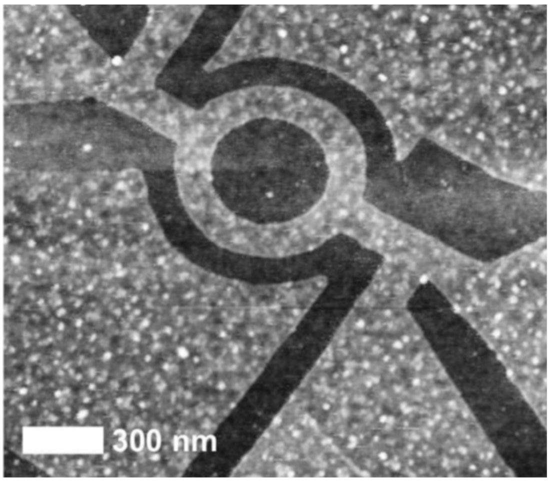

Figure 2.7: Scanning force micrograph of the ring structure. The ring has an inner radius of about 200 nm and an outer radius of about 350 nm. On each end of the ring structure, there are two graphene contact pads allowing us to perform four-terminal resistance measurements. The side gates lare located 100 nm away from the structure.

Nanoscale rings have been studied in nanostructures of a variety of different materials including carbon-materials such as carbon nanotubes. Only recently the Aharonov-Bohm effect has been observed for the first time in a two-terminal graphene ring structure. In this experiment the visibility of the Aharonov-Bohm oscillations was found to be less than 1% at low magnetic fields. It was speculated that this small value might be due to inhomogeneities in the two interferometer arms leading to a tunneling constriction that suppressed the oscillations.

Figure 2.7 displays a scanning force micrograph of the graphene ring studied in our group. The graphene flakes are produced by mechanical exfoliation of natural graphite, and deposited on a highly doped Si wafer covered by 295nm of silicon dioxide. Thin flakes are detected by optical microscopy, and Raman spectroscopy is used to confirm the single layer nature of the selected graphitic flakes. Electron beam lithography, followed by reactive ion etching is used to define the structure. The contacts are added in a second electron beam lithography step, followed by the evaporation of Cr/Au (2 nm/40 nm).

Standard low-frequency lock-in techniques are used to measure the resistance by applying a constant current. Figure 2.8 displays the resistance of the ring as a function of applied back gate voltage measured in a four terminal configuration. A smoothly varying background was subtracted. The ring itself is connected via two graphene ribbons of a size of 150x350 nm (graphene-leads) to a branching which ends in larger graphene areas, where four gold contacts are used to measure the resistance. The measured resistance is composed of the ring resistance itself and the resistance of the graphene leads.

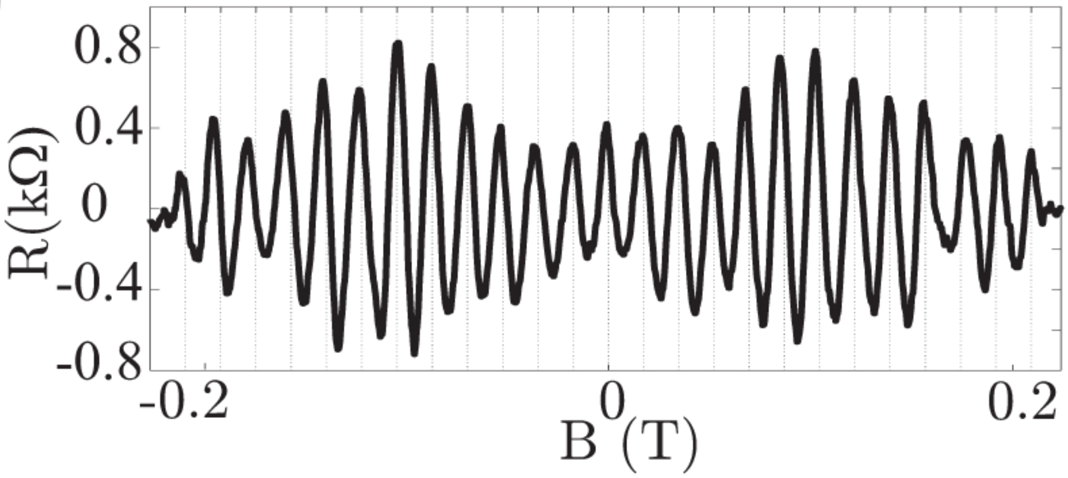

Figure 2.8: Four-terminal resistance across the ring as a function of magnetic field, recorded with a constant current of 5 nA. A smoothly varying background resistance has been subtracted.

The visibility of the oscillations is found to be about 5%. The main advantage of graphene compared to metals for Aharonov-Bohm studies is the reduced screening. This makes it possible to use external gates for locally tuning the density and the Fermi wave vector in one of the arms. We have shown that by changing the voltage applied to one of the side gates, we can induce a phase jump in the oscillations by changing the phase accumulated along this path. By changing the voltage applied to the lateral side gate, or the back gate, we observe phase jumps of π compatible with the generalized Onsager relations for two- terminal measurements. The observations are in good agreement with an interpretation in terms of diffusive metallic transport in a ring geometry.

2.5 Franck-Condon blockade in suspended carbon nanotube quantum dots

R. Leturcq, C. Stampfer, K. Inderbitzin, and K. Ensslin; in collaboration with L. Durrer, C. Hierold, Depaterment of Mechanical Engineering, ETH Zurich; E. Mariani, M. G. Schultz, F. v. Oppen, FU Berlin

In a polar semiconductor, a conduction electron deforms the surrounding lattice to form a polaron state. The formation of this quasi-particle, by combining an electron and a cloud of lattice vibrations, or phonons, strongly influences the transport properties. The possibility for localization of strongly coupled polarons was suggested by Landau more than 70 years ago. It was predicted that a related trapping of heavy polarons can occur in a quantum dot formed in a mechanically suspended nanostructure. In such a nanoelectromechanical system, the vibrational modes of the nanostructure can be strongly affected by the presence of electrons in the quantum dot, as they deform the embedding medium. For strong electron-phonon coupling, the deformation effectively blocks electronic transport, termed Franck-Condon blockade. By analyzing electronic transport through a suspended carbon nanotube (CNT) quantum dot over a wide range of electronic states, we are able to highlight generic features of vibron-assisted electronic transport, and unambiguously confirm the Franck-Condon blockade scenario.

A scanning electron microscope images of the suspended carbon nanotube (CNT) quantum dot device is shown in Fig. 2.9. The CNT is electrically and mechanically connected to both source (S) and drain (D) contacts, and the central electrode acts as a suspended top-gate. A quantum dot in the CNT is formed between defects15, which are presumably created during the release process and act as local barriers. The double top- and back-gate configuration enables us to determine the location of the quantum dot below the top-gate.

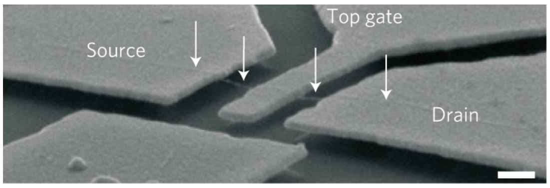

Figure 2.9: Electron microscope micrograph in tilted view of the suspended carbon nanotube (white arrows) with the source (S) and drain (D) electrodes and the central top-gate (TG) electrode.

The exceptional quality of this sample, which is crucial for this investigation, is revealed by the well-resolved observation of multiple four-fold degeneracies of electronic states in the large-scale presentation of our data (Fig. 2.10). This stems from the combined spin and valley degeneracies in clean CNTs, and enables the full characterization of the electronic properties of the device, including the electronic confinement energy.

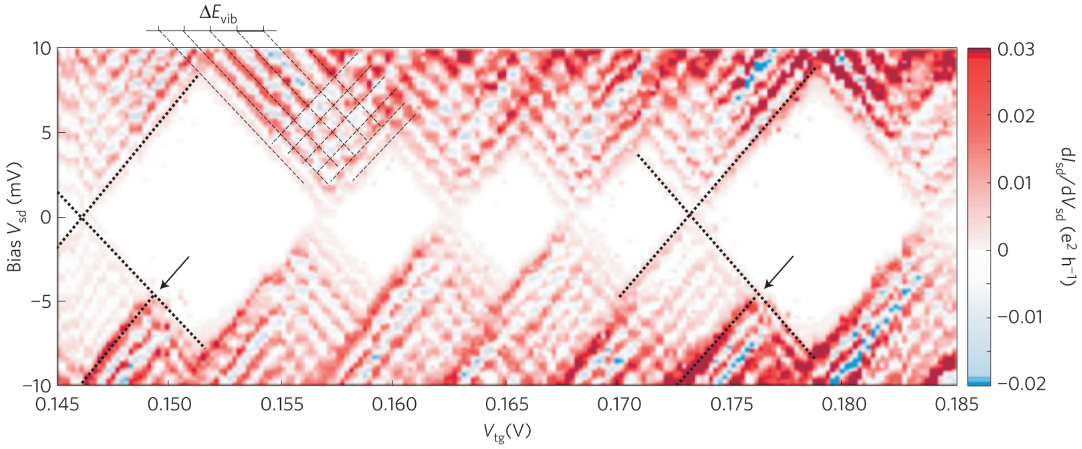

Figure 2.10: Differential conductance for a subset of Coulomb diamonds, showing quasi-periodic excited vibronic states (see dotted lines). The arrows point to electronic excited states, visible at higher energy.

At a finer energy scale (see Fig. 2.10), all of the probed Coulomb diamonds show several striking generic features. (1) Quasi-periodic lines running parallel to the edges of the Coulomb diamonds appear ubiquitously corresponding to excited vibronic states. (2) For increasing temperatures, the appearance of absorption sideband peaks within the Coulomb blockaded regions is observed. (3) At the edge of the diamonds, there is a pronounced current suppression compared with the current magnitude for excited vibronic states. (4) Most diamonds show a significant apparent shift of their tip between positive and negative bias. (5) Finally, all of the probed diamonds show ubiquitous negative differential conductance appearing in between the excited vibronic states. Most of these features are generic for transport-induced vibron excitations and are signatures of the strong electron-vibron coupling in this system.

Of the strongly coupled vibrons, only the longitudinal stretching modes are in a frequency range compatible with our experimental observations. The relevant dimensionless coupling constant g for the occurrence of the Franck-Condon blockade is given by (the square of) the shift of the equilibrium coordinate measured in units of the amplitude (oscillator length) of the vibronic quantum fluctuations.

2.6 Breaking of phase symmetry in nonequilibrium Aharonov-Bohm oscillations through a quantum dot

M. Sigrist, K. Ensslin, and T. Ihn; in collaboration with V. Puller, and Y. Meir, Ben-Gurion University, Israel

The Aharonov-Bohm (AB) effect allows for studying the transmission phase through a mesoscopic structure, e.g., a quantum dot (QD), by placing it in one of the arms of an AB interferometer. In a two-terminal interferometer the phase of the AB oscillations in the linear-response conductance can only assume the values 0 or π i.e., the oscillations have either maximum or minimum at zero magnetic field, even though the transmission phase through the QD can change continuously. This phase symmetry, i.e., the property that the linear-response conductance of a two-terminal device is an even function of magnetic flux, can be understood within a one-particle picture and is, in fact, a manifestation of more general linear-response Onsager-Büttiker symmetries.

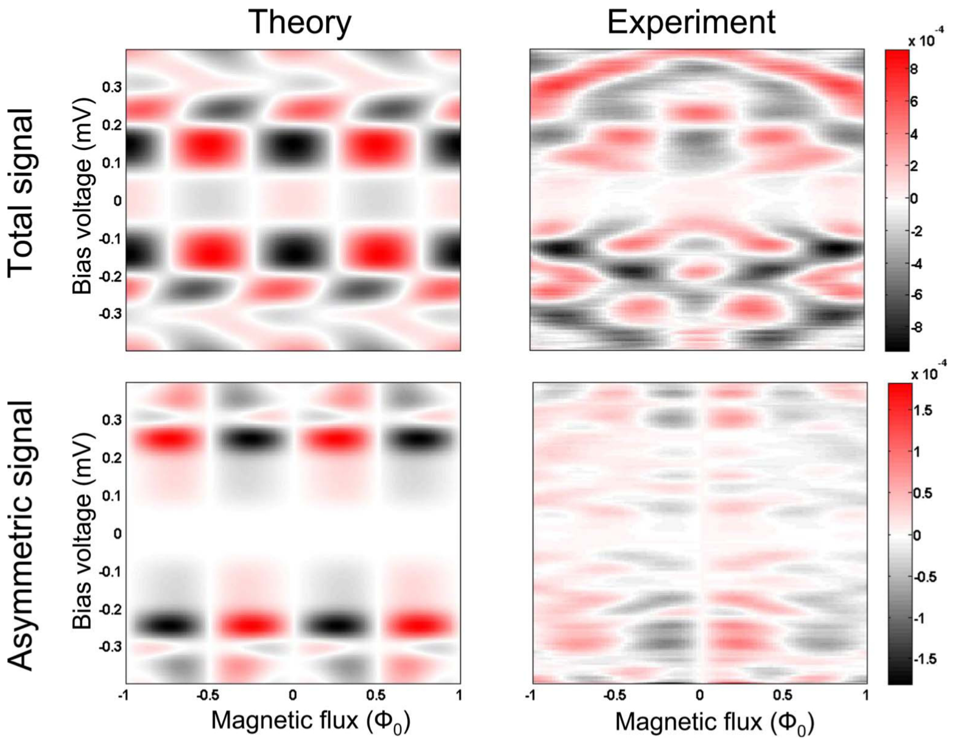

Figure 2.11: Color plots of the differential conductance obtained from the theoretical model (left panels) and from the experimental data (right panels). The upper and lower panels show, respectively, full and asymmetric components of the conductance.

We have addressed the phase asymmetry of AB oscillations in a QD interferometer with a Coulomb blockaded dot by systematically analyzing transport processes of different order in lead-to-lead tunnel coupling. We demonstrate that the bias dependence of the AB phase is highly non-monotonous.

The AB component of the differential conductance obtained within the perturbation framework described above is shown in the upper left panel of Fig. 2.11. One can see that the phase of the AB oscillations changes between 0 and π. The lower left panel of Fig. 2.11 depicts the asymmetric component of AB oscillations extracted from the data shown in the upper left. The right part of Fig. 2.11 presents, respectively, the corresponding experimental data.

The AB oscillations remain strictly symmetric up to the onset of inelastic cotunneling. As the asymmetric component of the AB oscillations is of higher order in lead-to-lead tunneling than the symmetric one, the AB phase remains close to the values 0 and π. The exception are the bias values where phase switching occurs and the asymmetric component of the AB oscillations becomes dominant. Altogether this results in the AB phase changing sharply but continuously between values 0 and π.

2.7 Gate-Controlled Spin-Orbit Interaction in a Parabolic GaAs=AlGaAs Quantum Well

M. Studer and K. Ensslin; in collaboration with G. Salis, IBM Zurich; D. C. Driscoll, and A. C. Gossard, University of California, Santa Barbara

Spin-orbit (SO) interaction is one of the key ingredients for future spintronic devices. In a two-dimensional electron gas (2DEG), SO interaction manifests itself as a spin splitting, and two different asymmetries can be responsible for it: The inversion asymmetry of a zinc blende crystal leads to the so-called Dresselhaus spin splitting, and an electric field E_{QW} along the growth direction enables Rashba-type spin splitting. E_{QW} is either generated by an asymmetrically grown layer structure (e.g., doping profile) or can be controlled externally by appropriate gating. The latter allows for a very efficient and scalable approach to control spins.

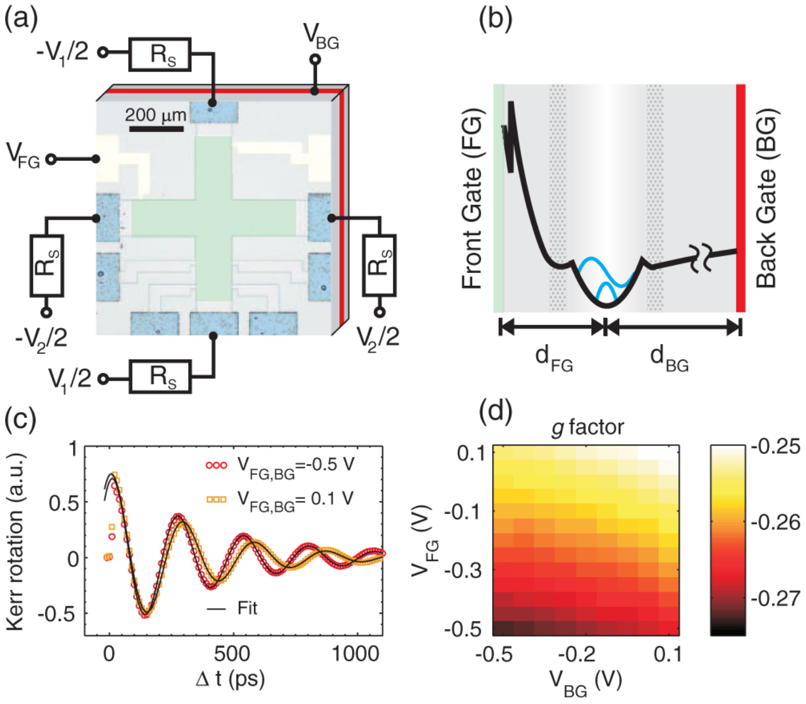

Figure 2.12: False color image as seen in an optical microscope: cross-shaped mesa structure covered by a front gate (FG, green) and Ohmic contacts on each end (blue). The back gate (BG) is indicated in red. (b) Schematic conduction band profile of the grown layer structure including gate electrodes and wave functions of the two occupied subbands. (c) Time-resolved Kerr rotation for $V_{FG} = V_{BG} = 0.5$V and 0.1V, respectively. (d) g factor of the electrons confined in the QW as a function of the gate voltages.

The structure measured is a molecular-beam epitaxy-grown AlGaAs quantum well (QW) with parabolic confinement. The QW is 100 nm thick, and the Al concentration varies from x=0 in the center of the well (located 105 nm below the surface) to x=0.4 at the edges. By using photolithography and wet etching, a cross-shaped mesa structure [see Fig. 2.12 (a)] with standard AuGe Ohmic contacts to the electron gas and the back gate is defined. A semitransparent front gate (FG) consisting of a 2 nm Ti adhesion layer and 6 nm of Au covers the cross. Time-resolved Kerr rotation is used to probe the spin dynamics of the carriers confined in the QW. The measurement of the SO interaction relies on the fact that the SO field and thus the total magnetic field depend on the direction and magnitude of the electron drift, induced by applied voltages V_1 and V_2 symmetrically to the four arms of the cross; Fig. 2.12(a).

The SO field originating from the Dresselhaus and the Rashba SO interactions has been measured in a system where an electric field perpendicular to the QW plane as well as the carrier sheet density can be controlled with a front gate and a back gate. A small Dresselhaus SO field and a Rashba-induced SO field that linearly depends on the external are found. By taking into account the two occupied subbands, the small values of the Dresselhaus SO field can be understood qualitatively.

2.8 Correlated counting of single electrons in a nanowire double quantum dot

T. Choi, I. Shorubalko, S. Gustavsson, T. Ihn, and K. Ensslin; in collaboration with S. Schön, FIRST lab, ETH Zurich

Probing the electronic state of quantum dots (QDs) by charge detection with quantum point contacts (QPCs) represents an elaborate method for investigating tunnel processes of single charges. The high sensitivity of the conductance of a QPC to its electrostatic environment allows to measure transitions in QDs in a regime where conventional transport measurements are impeded by the limited resolution of standard current meters. However, charge detection measurements are usually based on monitoring the average conductance of the QPC and thus measuring only the change of the average population of the QDs. In this respect, time-resolved charge detection marks a significant improvement since it offers the ability to count tunnel processes of individual single charges in real-time.

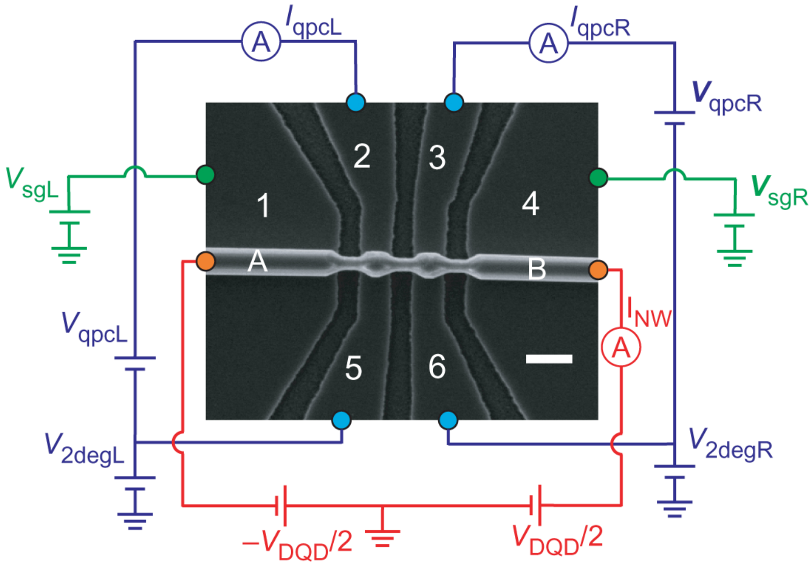

Figure 2.13: Scanning electron microscope image of the etched double quantum dot (DQD) structure with quantum point contacts (QPCs) and lateral side gates. A circuit scheme with the voltages and currents used in the measurement is shown in addition. A/B are the source/drain contacts of the NW. The source/drain contacts of the QPCs are the contacts 2/5 and 3/6 for the left and right QPC, respectively. The electronic width of the QPCs can be changed by applying voltages to the side gates on contacts 1/4. The current is measured through both QPCs and the NW. The bias voltage on the DQD is applied symmetrically to source and drain. Scale bar: 200 nm.

The nanowires (NWs) are grown by metal organic vapor-phase epitaxy (MOVPE) using colloidal Au particles as catalysts. The NWs have wurtzite crystal structure and are typically 100 nm in diameter and 10 μm long. The NWs are deposited on a predefined Hall bar of an AlGaAs/GaAs heterostructure with standard ohmic contacts. The heterostructure is grown by molecular beam epitaxy (MBE) and contains a two-dimensional electron gas (2DEG) 37 nm below the surface. The NW is furnished with Ti/Au ohmic contacts. Electron beam lithography (EBL)-patterned polymethyl methacrylate (PMMA) is used as an etching mask to define the DQD and the QPCs. The structure is etched with the same etching rate for both the NW and the heterostructure substrate. Typical etching times are around 15 s. The structure is designed in such a way that the trenches in the 2DEG forming the QPCs by depletion of the 2DEG underneath and the constrictions in the NW forming tunnel barriers of the DQD are defined in a single-step etching process. The fact that both trenches of the 2DEG and constrictions of the NW are defined simultaneously by the same etching areas ensures perfect alignment of the QPCs and the QDs.

A scanning electron microscope (SEM) image of the etched DQD structure and self- aligned QPCs together with a circuit scheme is shown in Fig. 2.13. The QPCs operate as local gates to change the electron population in each QD and as sensitive charge detectors for transitions in the DQD. Compensation voltages $V_{sgL/R}$ were applied to the side gates in order to keep both QPCs at a constant operation point. For the presented measurements, the QPCs are operated at a slope of the conductance close to pinch-off, where we get a desirable sensitivity to transitions in the DQD.

Time-resolved measurements of the tunneling processes in the DQD become possible as soon as the tunnel rates of the barriers defining the DQD are below the bandwidth of 20 kHz of the measurement setup. We tune the tunnel rates of the barriers in the NW by moving to different gate voltage regions until the tunnel processes occur on a sufficiently slow timescale. Single electrons tunneling through the three barriers defining the DQD can then be counted one by one in real-time. In contrast with previous experiments, we measure the two QPC signals simultaneously whose (anti-) correlation gives additional information on the electron tunneling processes.

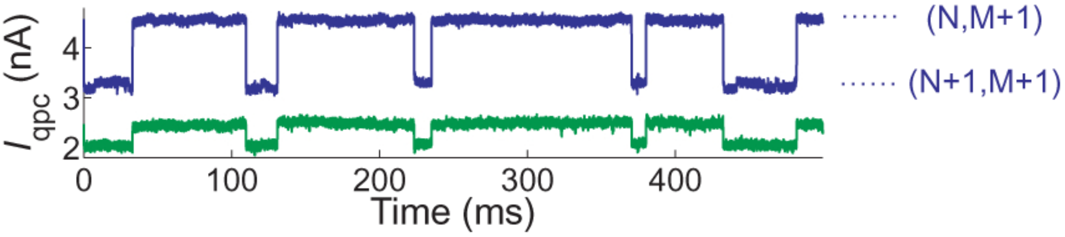

Figure 2.14: Time traces of both quantum point contacts (QPCs). Current traces of the right QPC are shown in green, the traces of the left QPC in blue.

Simultaneous to the charge detection with the right QPC, counting was also performed with the left QPC. Time traces of the current of both left and right QPCs allow a more comprehensive analysis of the tunnel processes across the DQD. Figure 2.14 shows a time trace of the QPC signals at a position where the electrochemical potential of the left QD is aligned with the source lead and tunneling thus occurs across the left barrier. The green traces are the current traces of the right QPC, whereas the left QPC traces are shown in blue. Both the left and the right QPC signals can clearly resolve two current levels corresponding to the charge states (N , M + 1) and (N + 1, M + 1).

We have presented time-resolved charge detection measurements which allow to track unambiguously individual electrons tunneling through the DQD in real-time and to determine the direction of the tunneling electrons. Both QPCs can detect all tunnel processes in the DQD exhibiting perfect correlation/anticorrelation of the signals. This enables us to distinguish clearly between QD-lead and interdot transitions. From the recorded time traces, all the tunnel rates of the involved tunnel processes can be extracted.

2.9 Noise-induced spectral shift measured in a double quantum dot

B. Küng, S. Gustavsson, T. Choi, I. Shorubalko, T. Ihn, and K. Ensslin; in collaboration with S. Schön, FIRST lab, ETH Zurich; F. Hassler and G. Blatter, Theoretical Physics, ETH Zurich

Charge detection with on-chip sensors provides a powerful tool for investigating the electronic properties of mesoscopic circuits. By performing the detection with sufficient bandwidth, the observation of single-electron charging events in real time becomes possible, which has been used, e.g., to read out the spin of quantum dots, to investigate the transport statistics of interacting electrons, or to measure small currents. Charge detection therefore comes with a considerable amount of back-action of the QPC on the QD to which both photons and phonons have been shown to contribute. One way of describing the photonic part of the back-action is in terms of the shot noise of the QPC which couples capacitively to the QD system and generates photon-assisted tunneling (PAT). From this viewpoint, the QD system can serve as a measurement device for the QPC noise. Since it works on chip, it is inherently fast and when using a double quantum dot (DQD), frequency-tunable noise detection becomes possible via control of the interdot level detuning.

Along a detuning line we continuously vary the energy difference between the charge configurations (1,0) and (0,1), as illustrated in the level diagram in Fig. 2.15 (a). Both dots are occupied by many electrons and the numbers ”0” and ”1” are used to simplify the presentation. The energies required for doubly occupying the DQD are higher by the mutual charging energy ≈ 0.8 meV, which was determined by finite-bias spectroscopy. An electron in the lower-energy dot can tunnel to the higher-energy dot by absorbing an energy quantum from the environment. The DQD system therefore acts as a tunable and frequency-selective probe for electrical noise in its vicinity.

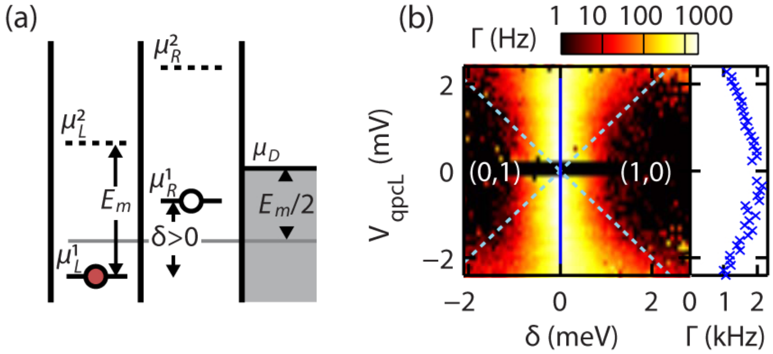

Figure 2.15: (a) Energy-level diagram of the double quantum dot (DQD) system and the drain lead. Upon adding a second electron to the DQD, the levels 1L, 1R shift by the mutual charging energy Em to the new positions 2L, 2R. (b) Colorscale plot of the interdot tunneling rate Γ as a function of level detuning (dashed line) and source-drain voltage across the left quantum point contact (QPC). Photons with energies bounded by the voltage applied across the QPC are emitted by the QPC and can drive inelastic tunneling events which leads to a broadening of the main peak (dashed lines indicate the cutoff). The plot on the right is a cut through zero detuning (solid line).

By applying a voltage across one of the QPCs, we generate broadband noise with a high-frequency cutoff, meaning that the electrons passing through the QPC have an exponentially small probability to emit photons with energies higher than the bias energy. Due to the capacitive coupling, the generated photons can be absorbed by the DQD and drive inelastic transitions. In measuring the interdot tunneling rate for increasing QPC bias, we therefore expect the equilibrium tunneling peak to become broadened due to photon absorption. In Fig. 2.15 (b), we plot the corresponding measurement for bias applied across the left QPC. A small region, where the signal-to-noise ratio of the counting signal is not sufficient, is excluded from the data.

Due to the full tunability of the DQD, we could observe the expected suppression of tunneling for zero dot detuning with increasing noise strength compensating for the increase in tunneling for nonzero detuning. Our data can be understood by treating the QPC as a high-frequency noise source. Finally, by measurements with two separate emitter QPCs we confirm that their effects add up independently.

Chapter 3

Condensed matter at low temperatures

(http://www.solid.phys.ethz.ch/ott)

Head

Prof. Dr. Joel Mesot
Prof. Dr. Hans-Rudolf Ott

Academic Staff

Dr. Toni Shiroka
Dr. Krunoslav Prša
Francesco Casola

Technical Staff

Academic Guests

Administrative Staff

Gabriela Strahm
Claudia Vinzens

3.1 Magnetism in doped 2-leg spin ladders

T. Shiroka, F. Casola, J. Mesot, and H.-R. Ott
in collaboration with S. Wang, K. Conder, E. Pomjakushina (PSI, Villigen)

Pure and doped low-dimensional Heisenberg antiferromagnets display a variety of exotic ground states, as e.g.: spin dimers, resonating valence bonds, spin-Peierls transitions, etc., whose magnetic properties are not only well described by theoretical models, but can be also directly investigated by experimental methods. $\mathrm{BiCu_2PO_6}$ is a frustrated 1-D spin system, where the spin-bearing ($S = 1/2$) Cu atoms are arranged in zig-zag shaped 2-leg ladders running along the b direction of the orthorhombic crystal structure. The antiferromagnetic exchange interaction along the rungs favours the formation of dimers with a singlet-type spin arrangement. Since experimental investigations able to detect changes in the magnetic properties upon replacing small amounts of Cu by divalent $S = 0$ zinc ions are particularly revealing, we have undertaken detailed ^{31}P nuclear magnetic resonance and magnetometry measurements on high-quality single crystals of $\mathrm{BiCu_2PO_6}$ and its Zn doped versions.

The availability of single crystals was essential in detecting distinct impurity-induced signals, whose presence is directly related to the local magnetic field distribution. We observe an intriguing temperature dependence for both the main and the impurity-related signals, in contrast with the broad and mostly featureless resonances reported in previous NMR studies on powder samples of the same or similar spin-ladder systems. Detailed spin-lattice relaxation measurements not only indicate a gap in the excitation spectrum up to room temperature for all the samples, but they clearly reflect a transition to an enhanced correlation regime among the uncompensated spins at 3.2 K for the 5% Zn-doped case. Most of the reported experimental results were tested by employing different state-of-the-art numerical calculations, which revealed the generic nature of the features of the measured resonance spectra.

Direct evidence for local cluster formation

For $x = 0$, the $\chi(T)$ data reveal the expected features of a low-dimensional dimerized spin $S = 1/2$ arrangement and confirm the very low concentration of defects. The temperature induced shift of the magnetic resonance signal reflects the generic magnetization of the spin system which is very well described by a model calculation employing an exact diagonalization method on an appropriate ensemble of 20 spins. For $x = 0.01$, evidence for impurity-induced local magnetization is obtained again from $\chi(T)$ data at low temperatures and from NMR spectra. In addition to the main NMR line, which broadens considerably in the low-T regime, we observe an impurity-induced peak which exhibits a logarithmic temperature dependence and moves across the main line (from the low- to the high-frequency region) as the temperature changes.

These findings are summarized in Fig. 4.3 where the broadening of the main line and the intriguing temperature dependence of the impurity peak are clearly seen. Preliminary QMC calculations using reasonable values for the exchange interactions along and perpendicular to the ladder legs confirmed the generic character of these features. An increase of x to 0.05 produces essentially the same features, except that the line broadening at low temperatures prevents the direct observation of the impurity peak below 70 K.

Impurity-induced spin freezing from NMR relaxation data

NMR spin-lattice relaxation rates $T_1^{-1}(T)$ were measured in samples with $x = 0$, 0.01 and 0.05. Above 25 K, $T_1^{-1}(T)$ is approximately the same for all three Zn concentrations and the exponential dependence reflects a spin gap Δ in the dimer excitation spectrum with $\Delta/k_\mathrm{B} \simeq 55$ K. This does not change visibly with increasing x and persists up to temperatures above 200 K, compatibly with the assumption that the spin-ladder system is thermally quite isolated from the crystal lattice. Distinct differences are, however, observed at low temperatures. The exponential decrease of the relaxation rate is interrupted at low temperatures and $T_1^{-1}(T)$ passes through an x-dependent minimum at $T_\mathrm{min}(x)$. For $x = 0$ and 0.01, the relaxation rate increases slightly below T_min and smoothly reaches an x-dependent saturation value. For $x = 0.05$ a considerable enhancement of the relaxation rate indicates substantial magnetic fluctuations in the spin system. Before saturation is reached, $T_1^{-1}(T)$ exhibits a rather narrow maximum with a sharp reduction of the relaxation at lower temperatures. This feature, displayed in Fig. 4.4, clearly indicates a transition in the spin system, most likely a freezing of the impurity-induced local magnetization clouds. Although this transition was conjectured from previous experimental data, no direct evidence as the one presented here has been provided before. Below 20 K the width of the main line of the $x = 0.05$ sample increases exponentially with temperature and not, as claimed in previous work on powder specimens, in a Curie-type manner (i.e., as $1/T$).

Our ^{31}P NMR results provide the first direct evidence for the formation of local clusters with non zero magnetization induced by non magnetic impurities in an $S = 1/2$, antiferromagnetically-coupled 2-leg spin ladder and reflect the temperature dependent development of this magnetization. Results of preliminary model calculations employing advanced calculation schemes are in good general agreement with our observations. Corresponding NMR relaxation data give the first direct evidence of a magnetic phase transition among impurity-induced clusters with local non-zero magnetization in this spin-ladder system.

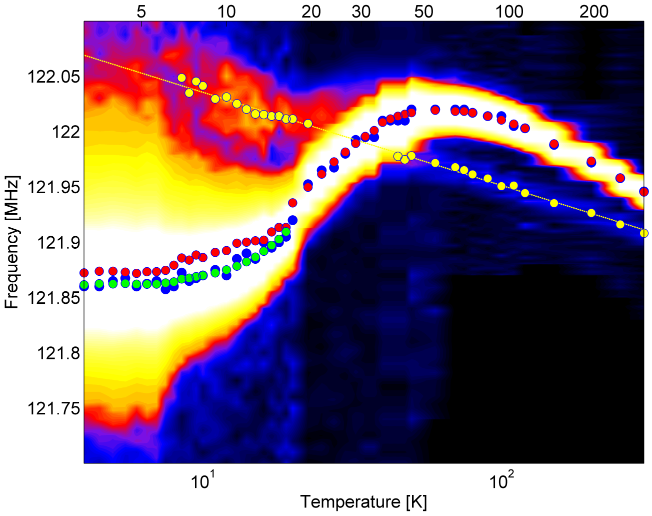

Figure 3.1: ^{31}P NMR line positions and shifts vs. temperature for Bi(Cu$_{1-x}$Zn$_x$)$_2$PO$_6$ with $x = 0.01$. Red, blue and green dots are Gaussian fits to the main line, yellow dots mark the maximum of the impurity signal.

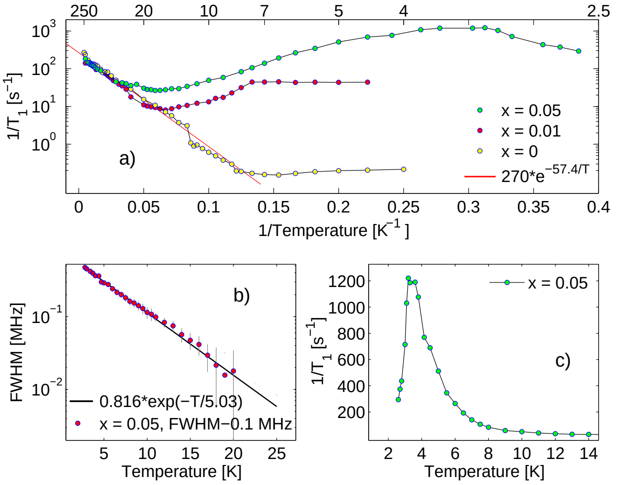

Figure 3.2: (a) $T_1^{-1}(T)$ for Bi(Cu$_{1-x}$Zn$_x$)$_2$PO$_6$ with $x = 0$, 0.01 and 0.05, respectively. (b) Temperature dependence of the NMR line width (FWHM) for the specimen with $x = 0.05$ below 20 K. (c) $T_1^{-1}(T)$ for $x = 0.05$ between 2.6 and 14 K.

Chapter 4

Microstructure research

(http://www.microstructure.ethz.ch)

Head
Prof. Dr. D. Pescia
Prof. Dr. M. Erbudak

Academic Staff
N. Saratz
Dr. U. Ramsperger
S.Burkardt
T. Kirk
Dr. A. Vindigni
L. De Pietro
Dr. O. Portmann

Technical Staff
Th. Bähler
H. Cabrera

Academic Guests
Prof. K. Sattler, University of Hawaii at Manoa, Klaus Sattler, June - July 2009,
Prof. Dr. John Xanthakis, from the National Technical University of Athens, 18.02.2009 - 21.02.2009
Dr. Chris Walker, University of York, 14.10.2009-16.10.2009
Dr. F. Cinti,University of Florence, 15. April - 15 May 2009
Prof. Stefano Ruffo, Dipartimento di Energetica ”Sergio Stecco”, Università di Firenze, 27.05.2009-29.05.2009
Prof. Orlando Vito Billoni, Universidad Nacional de Cordoba, Cordoba, Argentina, 02.09.2009-31.12.2009

4.1 Nanoscale Magnetism

Temperature induced domain shrinking in long-range-frustrated Ising ferromagnet

A. Vindigni, O. Portmann, N. Saratz, F. Cinti, D. Pescia

The competition between a short-ranged interaction favoring a uniformly ordered state and a long-range interaction preventing its realization on larger spatial scales is often assumed to be the mechanism underlying pattern formation in chemistry, biology and physics as well as opinion cluster emergence in social networks. A minimal spin model in which the ferromagnetic nearest-neighbor exchange interaction, J, competes with a long-range antiferromagnetic interaction of strength g may hopefully contain enough complexity to be paradigmatic for a variety of realistic systems. The lowest energy configuration – which is indeed realized at $T = 0$ – is given by a succession of domains with saturated positive and negative magnetization, which alternate in a sharp mono-dimensional modulation of well defined period. At finite T, the spins located at the interface between two oppositely magnetized domains are significantly more susceptible to thermal fluctuations than spins in the interior of the domains. As a result, the balance between the ferromagnetic exchange and the antiferromagnetic long-range interaction is biased in favor of the latter, which finally makes the modulation period shrink as T is increased, see Fig.1. Fig.1a shows the experimental stripe width measured in perpendicularly magnetized ultrathin Fe films on Cu(100) (data point with error bars). The dotted lines are the exact results of a Mean Field (MF) treatement of the frustrated Ising model Hamiltonian. Notice that in the shadowed region slow-dynamics effects become important so that the equilibrium-thermodynamic description does not apply anymore. In Fig.1b a typical MF magnetization profile inside a single stripe domain is reported for different T. Apart from $T \sim 0$, the average magnetization of the domain-wall spins (full triangles), is systematically lower than that of inside-domain spins. Consequently, the creation of new domain walls "costs" less and less as T is increased and domains with smaller equilibrium size are ultimately favored.

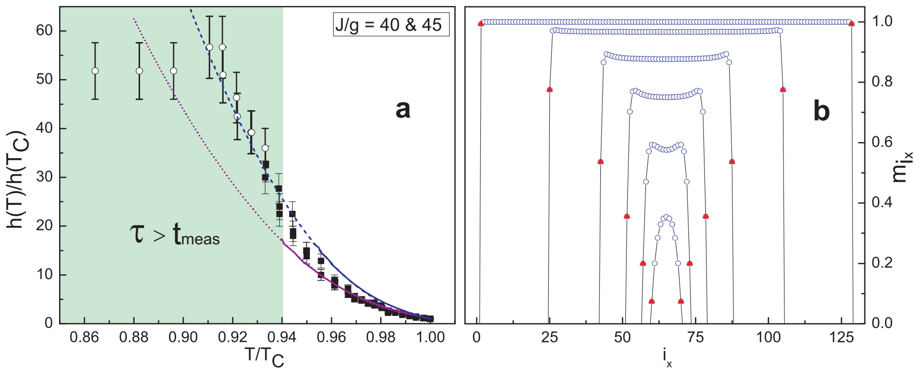

Figure 4.1: **a**: Relative domain width variation as a function of the reduced temperature, T_C being the Curie temperature. Experimental points correspond to labyrinthine (open circles) and striped (full square) patterns. Lines correspond to MF calculations performed for $\frac{J}{g} = 40$ (violet) and $\frac{J}{g} = 45$ (blue): exact (solid), parabolic extrapolation (dotted). In the shadowed region the relaxation time – estimated independently – becomes larger than the characteristic time of the measurements. **b**: MF magnetization profile inside a striped domain. The average magnetization on each site m_{i_x} is plotted versus the site index i_x itself.

Near Field Emission Scanning Electron Microscopy

T. L. Kirk, L. De Pietro, O. Scholder, U. Ramsperger, and D. Pescia

We report on further developments of ”near field emission scanning electron microscope” (NFESEM). In this instrument electrons are excited from the sample surface after undergoing interactions with a primary beam of electrons field-emitted from a polycrystalline Tungsten tip. The tip, with an emission radius of about 2nm, is scanned at less than 80nm distance to the surface. Topographic images, determined by measuring the intensity variations of backscattered electrons and of field emitted electrons, yield a vertical resolution on an atomic scale and a lateral resolution of a few nanometers. Our experimental setup consists of a homemade modified STM installed in a small ultrahigh vacuum (UHV) chamber with a base pressure of 2x10-11 mbar and a secondary electron detector (SED). Our SED is situated approximately 2cm from the sample edge and aligned to collect electrons ejected parallel to the surface. The SED cannot measure the energy of the electrons emanating from the surface, thus we are unable to verify if the electrons are inelastically or elastically scattered. We have chosen the W (110) surface for our present studies, as they are well characterized from the topographic point of view. Typically, an approach of the tip is performed using STM values for the set current and applied bias, which is used as a zero-point for the vertical positioning of the tip. After this step, the tip is retracted in the NFESEM modus, which measure both backscattered and Field emitted currents. STM measurements [Fig. 2(a)] exhibit rectangular terraces with sharp single atom step edges. The topography generated from the backscattered electrons (Fig.2b) and field emitted current [Fig. 2c)] are almost indistinguishable and also show clearly single atomic steps. Notice that, although only topographic data have been presented, the SE also contain magnetic and chemical information. We are particularly interested in applying the NFESEM to the magnetic characterization of surfaces.

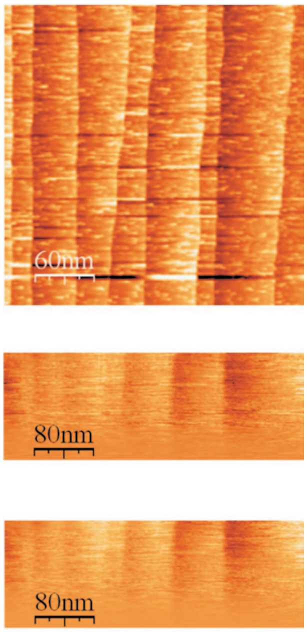

Figure 4.2: FIG. 2 (color). Micrographs of a single crystal W (110) surface. (a) The tip-sample separation was decreased for STM imaging in constant current mode after imaging in field emission mode, scanning an area of 300nm x 300nm with a tunnel current of 0.2nA and a bias of 200mV. Frequent current jumps occurred during scanning causing the horizontal stripes in the image. (b) 145nm x 400nm topographic image from the electron intensity of the backscattered electrons. The primary beam energy was 33.2eV with a field emission current of 50nA, effective emission radius 1.8nm, and the tip-sample separation was initially 50nm. (c) Resultant field emission current recorded simultaneously with the secondary electron signal.

4.2 Surface Physics

Head
Prof. Dr. M. Erbudak

Academic Staff
Dr. S. Burkardt

Academic Guests
Prof. Muhittin Mungan, Bogazici University, TR-Istanbul (7.2. - 15.2.2009)
Prof. Ahmet Oral, Sabanci University, TR-Istanbul (11.2. -14.2.2009)
Prof. Engin Özdas, Hacettepe University, TR-Ankara (21.2. - 26.2.2009) und (12.7. - 17.7.2009)
Dr. Gerald Kasner, Uni. Magdeburg (19.4. - 21.4.2009)
Selin Manukyan, Sabanci University, TR-Istanbul (25.4. - 30.4.2009)
Prof. Oguz Gülseren, Bilkent University (14.5. - 17.5.2009)
Merve Arseven, Hacettepe University (30.6 - 17.7.2009)
Dr. Zorka Papadopolos, Uni. Tübingen (7.9. - 11.9.2009)
Özlem Deveci, Samsun University, TR-Samsun (16.11. - 17.12.2009)

The surfaces of quasicrystals offer a great challenge for scientific research owing to the high degree of orientational order in the absence of periodicity. In particular, the growth of atomic overlayers on quasicrystal surfaces has attracted considerable interest. The goal is to grow a system of reduced chemical or dimensional complexity to investigate the influence of aperiodic atomic ordering on the resultant physical properties. Hence, pseudomorphic growth of single element overlayers and heterogeneously nucleated film growth have been the main focus in this field of research. One example is that, as a consequence of their structural diversities, crystalline adsorbate on a quasicrystalline substrate was found to result in a self-size-selecting growth, leading to a self-assembled, nanometer-size domain structure.

Recently, the selective oxidation of quasicrystals has contributed a further interesting surface phenomenon. Metal oxide interfaces are of great interest for many technological applications, in particular, are ideally suited as model catalysts. It was found that the Al-rich quasicrystals show a similar oxidation behavior compared to Al single crystals and ordered Al-transition-metal alloys. Experimental results have indicated that the local structure of the oxide layers grown on the quasicrystalline surfaces are related to the common phases of Al_2O_3. Nevertheless, due to the extreme shallowness of the film as well as the relatively large unit cell of the oxide structure, the detailed atomic ordering of these oxide layers has not been readily resolved and still presents a substantial challenge to surface science.

Oxygen on the decagonal AlCoNi quasicrystal: Chemisorption and oxidation

S. Burkardt, M. Erbudak

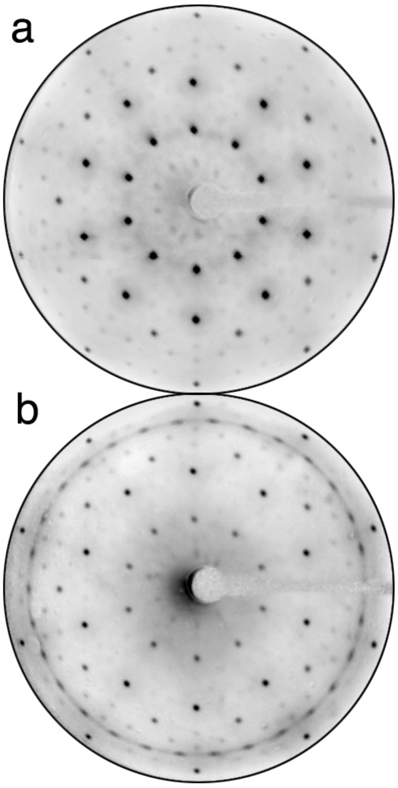

Figure 4.3: LEED patterns at 50 eV obtained from (a) the clean and (b) exposed tenfold-symmetry surface of AlCoNi to 100 Langmuirs of oxygen. The patterns are grey-scale inverted for better identification of diffraction features.

Figure 4.3 displays LEED patterns obtained from the decagonal surface (a) before and (b) after exposure to oxygen partial pressure of 1×10^{-8} mbar at 870 K for 1000 s. Oxygen exposure results in thirty new diffraction features placed on a polar circle of about 40.5°. In accordance with the local symmetry of the quasicrystalline surface, these spots represent a sixfold-symmetric pattern, repeated five times in equal azimuthal increments of $2\pi/5$. Each sixfold-symmetric pattern is due to a hexagonal mesh with an interatomic distance of 3.08 Å. We note that his value is 10% larger than the interatomic O-O distance in different phases of Al_2O_3. The polar precision of the streaks point to an unexpectedly large domain size of about 150 Å, while the azimuthal spread arises as a consequence of the relaxation of the crystalline adlayer compared to the quasicrystalline substrate. The latter facilitates the growth of the adlayer in this extraordinarily large size. The diffraction spots characteristic of the clean quasicrystalline surface are still observable indicating that the surface film is only few Å thin. The observation of these spots at the same place further indicates that the formation of the surface layer preserves the quasicrystalline order at the interface.

Auger electron spectroscopy shows no energy shift for the Al signal after oxygen adsorption, but some reduction of the intensity, indicating that there is no appreciable electron transfer from the metal site to oxygen, i.e., oxygen is in the chemisorbed state. The dissociative adsorption of oxygen has already been observed on Al(111), where the formation of a hexagonal oxygen structure is compatible with the substrate symmetry. In the present case, however, the substrate, while containing Al, has a quasicrystalline structure on which the sixfold symmetric oxygen adlayer assembles.

As the surface is more exposed to oxygen, the LEED spots from the oxide structure gradually appear and reach their best definition at around 430 L (see Figure 4.4), while the spots from the quasicrystalline substrate decrease in intensity at a constant spot profile. Apparently, the oxidation process does not destroy the quasicrystalline order at the interface. The striking feature of the pattern is 30 diffraction spots located on a polar circle corresponding to a momentum transfer of 2.414 $Å^{-1}$ and an interatomic distance of 3.01 Å, respectively. This value is very close to the distance of the interatomic O-O distance in the oxide structures grown on other Al-rich alloy surfaces.

Spot profile analysis of diffracted beams indicate a domain size of the oxide layer as large as 35 Å as a result of the self-size-selecting growth at a crystal-quasicrystal interface. Further, beside the main hexagonal diffraction feature, additional spots placed on inner as well as outer rings of constant polar angle are identified in the LEED pattern. While the Auger transition-metal signals do not indicate any change in energy and line shape after the exposure of the clean quasicrystalline substrate to oxygen, the Al-O interatomic Auger transitions are characteristic of the formation of Al-O bonds.

Therefore, LEED experiments are consistent with five pairs of oxygen domains exposing their faces parallel to the surface and rotated by 72° with respect to each other, reflecting the local symmetry of the decagonal substrate. Besides the main hexagonal feature, the details of the diffraction pattern can be ascribed to antiphase domain boundaries along high-symmetry directions of the decagonal surface as the main dislocations in the oxide layer. The domain boundary distances can be unambiguously related to the decagonal surface ordering of AlCoNi suggesting that the quasicrystalline surface acts as a template for growth of the Al-oxide domains.

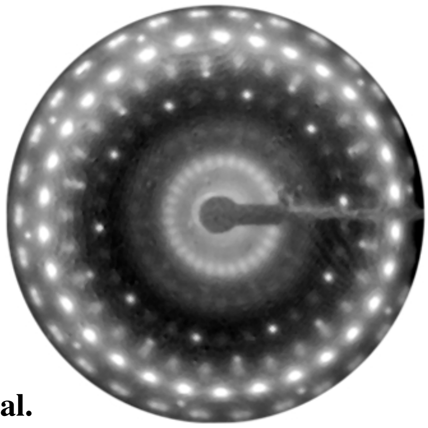

Figure 4.4: LEED pattern obtained from the tenfold-symmetry surface of AlCoNi exposed to 430 Langmuirs of oxygen.

Simulation of atomic adsorption on the decagonal AlCoNi quasicrystal.

M.Mungan, S. Burkardt, M. Erbudak

We perform molecular-dynamics simulations of how deposited adatoms diffuse on the adsorbate-substrate surface in order to understand the morphology of the growing adlayer. In our calculations, 1 ML of adatoms corresponds to about 3100 particles. In the simulations, we inject adatoms in batches of 180 particles onto the substrate. The quasicrystalline bilayer is kept rigid, but adatoms are allowed to interact with each other and with the substrate atoms. The relative strength of the adatom-adatom and adatom-substrate interactions is controlled by a dimensionless parameter η.

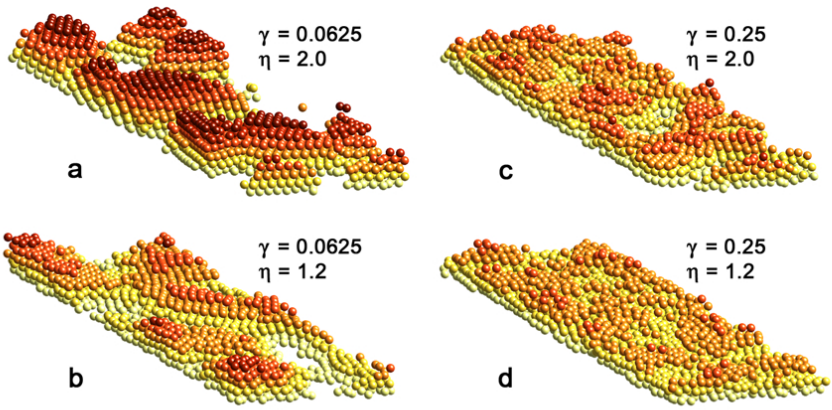

Figure 4.5: Structure of the adsorbate surface at 2.5 ML coverage for different damping rates γ and strength of adatom interactions η relative to substrate. Note that more locally ordered and more corrugated structure emerges for stronger adatom interactions.

In real experiments, hot impinging adatoms lose their excess kinetic energy to the substrate and eventually reach thermal equilibrium. In our simulations, we account for this process by introducing damping and treating the damping rate γ as a parameter by which we can change the thermal relaxation times. We were able to explain how deposition at high γ along with low η values, e.g., $\gamma = 0.25$ and $\eta = 1$, gives rise to layer-by-layer type of growth, while keeping γ constant and increasing η will increase the probability of arriving adatoms to be deposited on already present ones giving rise to a cluster-type growth. We also found that well-ordered domains can grow at lower η values if the damping rate is reduced, so that impinging adatoms can diffuse longer on the substrate surface and, moreover, with increasing coverage, there will be more accessible favorable binding sites, since they will include both already deposited adatoms as well as substrate sites that have remained exposed.

In Figure 4.5 we show 150 Å × 50 Å × 15 Å × sections of the adsorbate for values of $\gamma = 0.0625$ (left column) $\gamma = 0.25$ (right column) and $\eta = 2$ (top row) and $\eta = 1.2$ (bottom row) after deposition of 2.5 ML. Although we find comparable diffusion distances for configurations with different η (configurations in the same column), the morphology of the corresponding surfaces is different. For both $\gamma = 0.25$ and 0.0625, the surfaces with stronger relative adatom interactions, $\eta = 2$ exhibit enhanced well-ordered hexagonal domains, which are less pronounced for $\eta = 1.2$ (bottom row). The adlayer formed under low damping and strong adatom interaction shows the largest amount of corrugation along with local hexagonal order (top left).

We see, both in the experiment and simulations, that epitaxially grown oxygen on the quasicrystalline surface experience competing interactions. While they favor ordering in a stable hexagonal mesh, the quasicrystalline surface template they condense on, force them into an aperiodic order. The system finds the best compromise by partially satisfying both conditions and breaks up into domains ordered in a hexagonal structure, where each domain remains locally commensurate and in registry with the substrate. This registry results in five distinct orientations for the nanocrystals. The size of these domains is determined by the interfacial strain energy, as this size increases the island edges get rapidly out of registry with the substrate and it becomes energetically more favorable to break up into locally commensurate domains.

4.3 Thin Film Physics

Head
PD Dr. H. Zogg

Academic Staff

F. Felder	M. Fill	M. Rahim
A. Khiar		

Technical Staff
O. Meier

Mid-IR devices with epitaxial IV-VI narrow-gap semiconductor layers

F. Felder, M. Fill, M. Rahim, A. Khiar, and H. Zogg

By employing epitaxial narrow gap lead chalcogenide (IV-VI) layers, it was possible to realize mid-IR VECSEL (vertical external cavity surface emitting laser) and RCED (resonant cavity enhanced detector) for the first time. The materials are grown by solid source molecular beam epitaxy (MBE) onto Si(111)-substrates by employing a CaF$_2$ buffer layer. Despite the huge lattice and thermal expansion mismatch between the materials, device quality layers result. This is because lead-chalcogenides are fault tolerant. Typical compositions of the active mid-IR layers include Pb1-xSnxX, Pb1-xEuxX and Pb1-xSrxX (X=Te, Se). They allow to realize devices in the $< 3\mu$m up to $> 10\mu$m wavelength range by choosing appropriate compositions x. In addition, extremely high reflectivity Bragg mirrors are needed to realise such devices. Such epitaxial Bragg mirrors with very high reflectivity over a broad spectral range are again easily obtained with IV-VI materials. The mirrors consist of quarter wavelength layers with alternating high and low refractive indices. Due to the high index contrast, a few pairs only suffice.

Vertical External Cavity Surface Emitting Laser (VECSEL) on Si

A recent lay out consists mainly of a 800 nm thick PbTe active layer grown on a Si-substrate. It is followed by a $3\,\frac{1}{2}$ pair Bragg mirror and soldered on a Cu heat sink. The opposite curved mirror is again of Bragg type and serves as output coupler. Pumping is done optically with a commercial 1.55 μm wavelength laser diode. The device operates up to room temperature. At 100 K heat sink temperature, output power is above 1 W in pulsed mode, and 20 mW in continous wave (cw). Compared to the well known edge-emitting quantum cascade lasers (QCL) which consist of several hundred interfaces, the lay-out of our VECSELs is extremely simple. In addition, VECSEL exhibit a very good beam quality (emission in a 1°circular cone). This is in contrast to QCLs where the wide angle astigmatic beam requires elaborate optical beam conditioning for most applications.

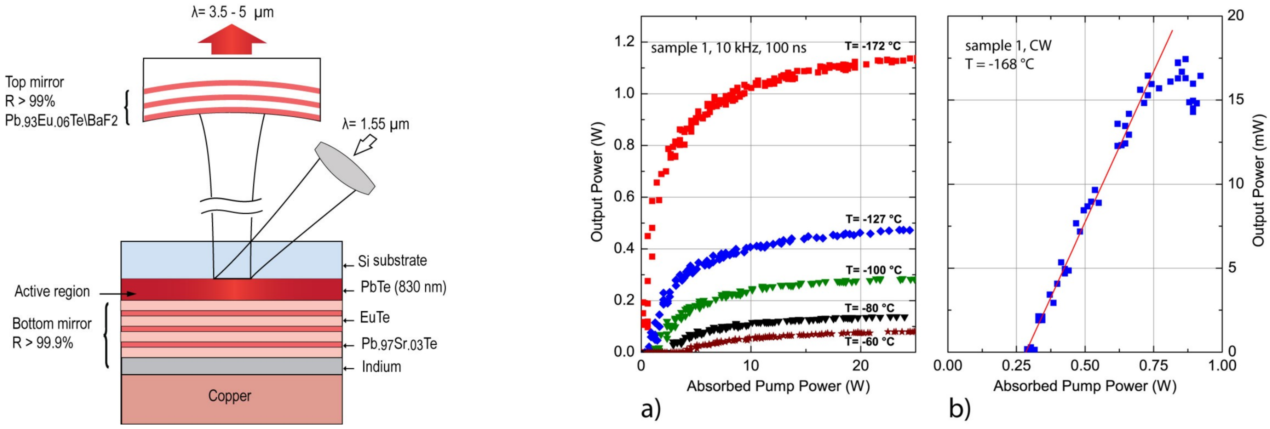

Figure 4.6: Schematic representation of a PbTe-based IV-VI VECSEL realized on a Si-substrate. The curved Bragg mirror is used as output coupler (left). Light-in/light-out characteristics at different temperatures (right) in pulsed mode (a) and cw (b).

We currently work on further improvements:

- diamond heat-spreaders will allow room temperature cw operation
- using short cavities (L $\lesssim 100\mu$m), monomode operation results. The wavelength is continuously tunable by slightly changing L with piezo-drivers across a range of up to 10%
- using quantum well structures in the active layers, threshold powers will decrease considerably

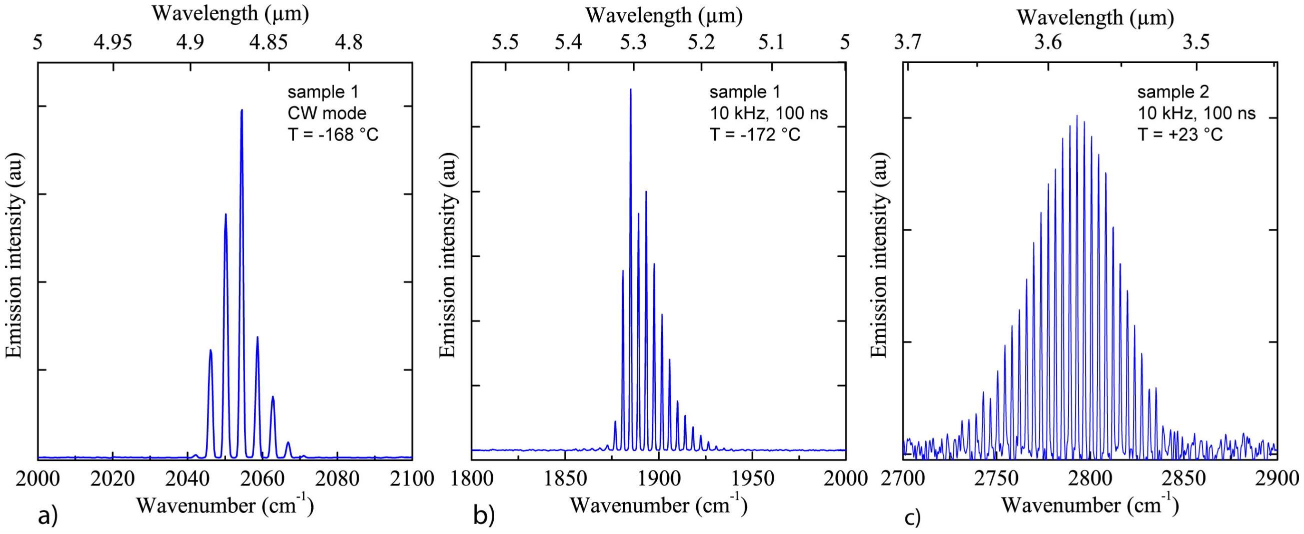

Figure 4.7: Normalized PbTe based VECSEL-on-Si lasing spectra at different heat sink temperatures

Resonant cavity enhanced detector (RCED)

Collaboration with the Center of Mechanics, ETH Zurich (J. Dual, S. Blunier, N. Quack), www.zfm.ethz.ch

A resonant cavity enhanced detector (RCED) is an embedded absorber layer within a Fabry-Perot cavity. The RCED is sensitive mainly at the resonance wavelengths, where it exhibits a high quantum efficiency. By changing the cavity length, wavelength tuning is possible. We realized RCEDs with movable MEMS micromirrors. They operate in the 3 to 7 μm range using different compositions of the absorber layer. A typical total tunable range is 0.5 μ for a specific device.

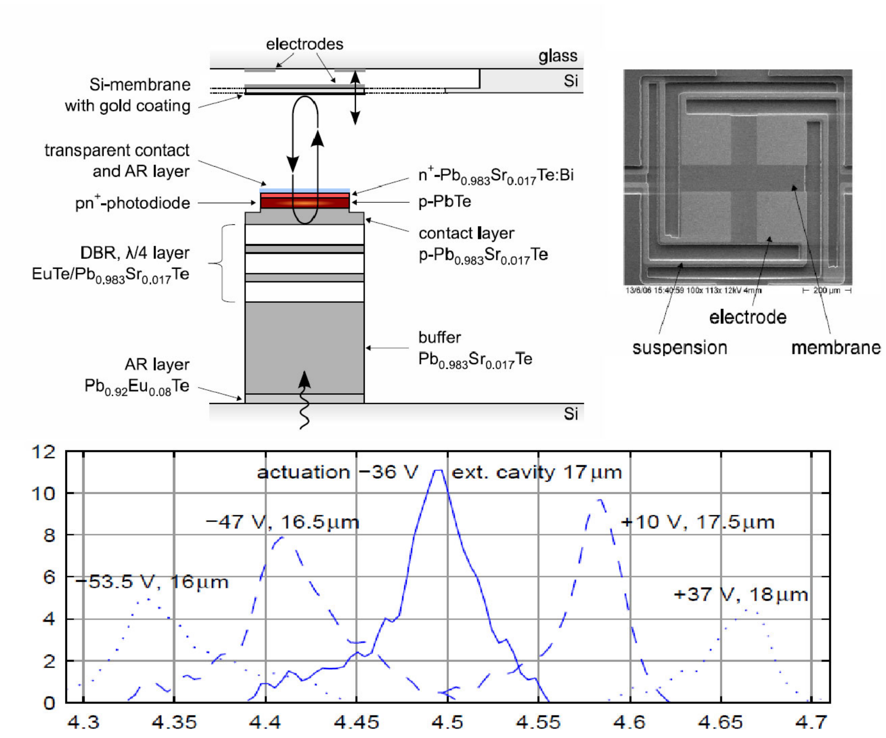

Figure 4.8: Schematics of a RCED (top left), micromirror (top right), and measured spectra for different MEMS actuation voltages (left)

Chapter 5

Optical Spectroscopy

(http://www.solidphys.ethz.ch/spectro/h)

Head
Prof. Dr. L. Degiorgi

Academic Staff
Dr. A. Lucarelli
F. Pfuner
A. Dusza (from 1.12.09 on)

Technical Staff

Academic Guests

Administrative Staff
I. Mettler

5.1 Raman scattering evidence for a cascade-like evolution of the charge-density-wave collective amplitude mode

M. Lavagnini, R. Monnier and L. Degiorgi
work in collaboration with H.-M. Eiter, L. Tassini, B. Muschler and R. Hackl, Walther-Meissner-Institut, Bayerische-Akademie der Wissenschaften, Garching, Germany, J.-H. Chu, N. Ru and I.R. Fisher, Stanford University, California, U.S.A.

Electronic instabilities are at the origin of phenomena as diverse as the formation of spin and charge density waves (SDW and CDW) or superconductivity, the interplay of which is among the most intriguing open questions of modern solid state physics. Besides determining the ground state of the quantum system in which they occur, electronic instabilities also fundamentally affect its excitation spectrum. In the CDW state, on which we focus here, a gap opens up in the single particle spectrum, and two new collective modes, associated with the oscillations of the amplitude and of the phase of the CDW, respectively, appear. The paradigm of CDW forming materials are the quasi one-dimensional compounds. But electronically driven CDW states were also found and thoroughly investigated in novel two-dimensional (2D) layered compounds, an effort motivated in part by the fact that high temperature superconductivity in the copper-oxide systems may indeed emerge from a peculiar charge-ordering through the tuning of relevant parameters.

A family of layered compounds which have attracted a lot of attention recently are the rare-earth (R) tri-tellurides RTe$_3$. They host an $unidirectional$, incommensurate CDW already well above room temperature for all R elements lighter than Dy, while in the heavy rare-earth tri-tellurides (i.e., R=Tm, Er, Ho, Dy) the corresponding transition temperature, T_{CDW1}, lies below $\sim$300 K and decreases with increasing R mass. In the latter systems, a further transition to a $bidirectional$ CDW state occurs at T_{CDW2}, ranging from 180 K for TmTe$_3$ to 50 K for DyTe$_3$.

We have presented new Raman scattering investigations as a function of temperature on DyTe$_3$ at ambient pressure (T_{CDW1}=307 K, T_{CDW2}=49 K) and on LaTe$_3$ at 6 GPa, with a lattice constant between that of DyTe$_3$ and HoTe$_3$, and $T_{CDW1} \sim$ 260 K. The covered spectral range extends from 5 to 200 cm^{-1}, thus giving access to the energy region in which the collective modes are expected to appear.

Figure 1 displays the imaginary part $\chi''(\omega, T)$ of the Raman response obtained by dividing the measured spectra by the thermal Bose factor. The general trend in temperature for both sets of data is quite similar, suggesting that by hydrostatically compressing the lattice (as for LaTe$_3$ at 6 GPa) one can recover the properties and responses of chemically compressed RTe$_3$ (i.e., through substitution of the R element). This confirms our earlier findings at 300 K as a function of pressure. At low temperatures and deep in the CDW state, we observe well distinct and rather sharp modes. Above 80 cm^{-1} the modes, previously ascribed to the Raman

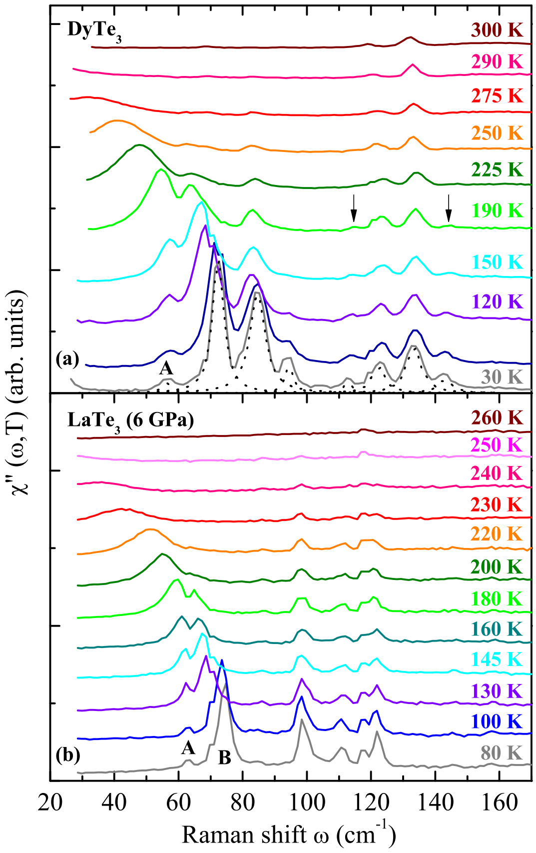

Figure 5.1: Temperature dependence of the Raman scattering spectra of DyTe$_3$ at ambient pressure (a) and of LaTe$_3$ at 6 GPa (b). The spectra have been shifted for clarity. In panel (a) the oscillators employed for the data fits are shown for the measurement at 30 K (dotted lines) and the arrows mark the weak features at 113 and 143 cm^{-1}. The labels A and B denote the weak mode at $\sim$ 60 cm^{-1} and the sharp one at $\sim$ 70 cm^{-1} at low temperatures, respectively.

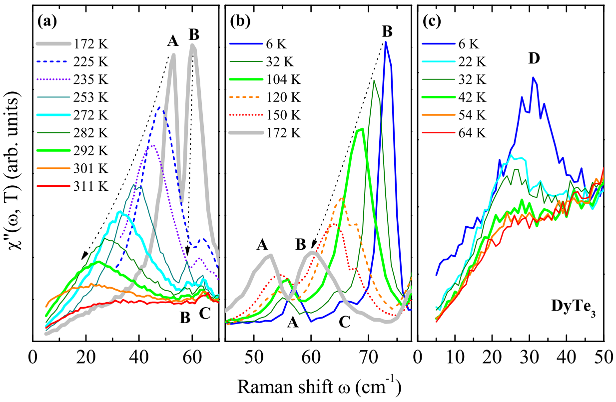

Figure 5.2: Detailed view of the temperature dependence of the A, B (see Fig. 1a) and C modes of DyTe$_3$ above (a) and below (b) T_{tr}. The arrows highlight the trend of modes A and B with increasing temperature. (c) Low frequency interval characterized by mode D for temperatures close to and below T_{CDW2}. The relative intensity ratio among panels (a-c) is 2:8:1.

active phonons with A_{1g}, and A_1 and B_1 symmetry for the undistorted (pseudotetragonal) and distorted phase respectively, lose spectral weight with increasing temperature, while their width marginally changes as a function of temperature. For $\omega \leq 80$ cm^{-1} and at low temperatures there is a weak peak close to 60 cm^{-1} and a sharp one around 70 cm^{-1} (labels A and B in Fig. 1). Their temperature dependence is specifically emphasized for DyTe$_3$ in Fig. 2a and 2b. Upon destroying the CDW state with increasing temperature the sharp B mode first softens, gets progressively broader and loses spectral intensity in favor of the A feature (Fig. 1a and 2b). At T_{tr} of about 170 (160) K for DyTe$_3$ (LaTe$_3$ at 6 GPa), the two modes roughly share the same amount of spectral intensity (Fig. 1 and 2(a-b)). Upon approaching T_{CDW1} the energy of the B mode becomes constant, while its intensity drops above T_{tr} and vanishes at T_{CDW1}, as does that of the A mode, whose resonance frequency saturates at 23 cm^{-1} (Fig. 2a). We believe, that our findings provide a clear-cut evidence for the emergence of the collective unidirectional CDW amplitude excitation, which develops as a succession of two transitions with different critical temperatures (T_{CDW} and T_{tr}). This cascade-like evolution of the collective excitation is well reflected by the redistribution of spectral intensity occurring among feature A and B. In contrast mode C, which is only seen at high resolution (Fig. 2(a-b)), exists already above T_{CDW1} and survives the transition, without displaying any temperature dependence. In the low temperature spectra of DyTe$_3$ an additional mode (D) in the range below 50 cm^{-1} (Fig. 2c) is found, which disappears upon increasing the temperature above T_{CDW2}. From the temperature dependence observed in Fig. 2c, we can safely conclude that this mode is the collective amplitude mode of the bidirectional CDW state.

In summary, our careful analysis of the temperature dependence of the collective modes in RTe$_3$, as obtained by Raman scattering, has shown that the rare-earth tri-tellurides support not only one but *two* different unidirectional CDW's, a property that follows from the presence of two adjacent Te planes in the crystal structure. In addition, we have, for the first time to our knowledge, identified the collective mode associated with the low temperature, bidirectional CDW phase, recently observed by x-ray diffraction in the heavy RTe$_3$ compounds.

5.2 Charge dynamics of the spin-density-wave state in BaFe$_2$As$_2$

F. Pfuner and L. Degiorgi
work in collaboration with J.G. Analytis, J.-H. Chu and I.R. Fisher, Stanford University, California, U.S.A.

A new field in condensed matter research was recently initiated by the discovery of superconductivity in doped iron oxyarsenides. After the first report on LaFeAs(O$_{1-x}$F$_x$) with a critical temperature T_c of 26 K, even higher transition temperatures up to 55 K were reached in fluorine doped SmFeAs(O$_{1-x}$F$_x$). This novel family of compounds has generated a lot of interest, primarily because high-temperature superconductivity is possible in materials without CuO$_2$ planes. Since these planes are essential for superconductivity in the copper oxides, its occurrence in the pnictides raises the tantalizing question of a different pairing mechanism. While the nature of such a pairing mechanism is currently in dispute, it is evident that superconductivity in the oxypnictides emerges from specific structural and electronic conditions in the (FeAs)$^{\delta-}$ layer. Therefore, it soon appears that other structure types could serve as parent material. The recently discovered BaFe$_2$As$_2$ compound with the well-known ThCr$_2$Si$_2$-type structure is an excellent candidate. It is also currently believed that the superconductivity in these systems is intimately connected with magnetic fluctuations and a spin-density-wave (SDW) anomaly within the FeAs layers. This is obviously of interest, since a SDW phase may generally compete with other possible orderings and complicated phase diagrams are often drawn due to their interplay. It is therefore of relevance to acquire deeper insight into the SDW phase and to establish how this broken symmetry ground state affects the electronic properties of these materials.

We focused our attention on BaFe$_2$As$_2$, which is a poor metal exhibiting Pauli paramagnetism and where the SDW phase transition at T_{SDW} is accompanied by anomalies in the specific heat, electrical resistance and magnetic susceptibility. We provide a thorough investigation of the optical response over an extremely broad spectral range at temperatures both above and below T_{SDW}.

Figure 3a displays the optical reflectivity in the far-infrared (FIR) energy interval (i.e., $\omega \leq 600$ cm^{-1}), emphasizing its temperature dependence. The inset of Fig. 3a shows on the other hand $R(\omega)$ over the whole measured range at 10 and 200 K. $R(\omega)$ of BaFe$_2$As$_2$ has an overall metallic behavior, characterized by a broad bump at about 5000 cm^{-1} and by the onset of the reflectivity plasma edge below 3000 cm^{-1} (inset Fig. 3a). Figure 3b then shows the real part $\sigma_1(\omega)$ of the optical conductivity at various temperatures, resulting from the KK transformation of the measured $R(\omega)$. In the inset of Fig. 3b we display the overall optical conductivity at 10 and 200 K. From the data emerges a picture in which at $T > T_{SDW}$ delocalized states (i.e., free charge carriers close to the Fermi level) coexist with more localized or low-mobility states. When lowering the temperature below T_{SDW}, a pseudogap develops and a rearrangement of states takes place in such a way that excitations pile up in the spectral range around 420 cm^{-1} as well as around 50 cm^{-1}. These latter excitations merge into the high

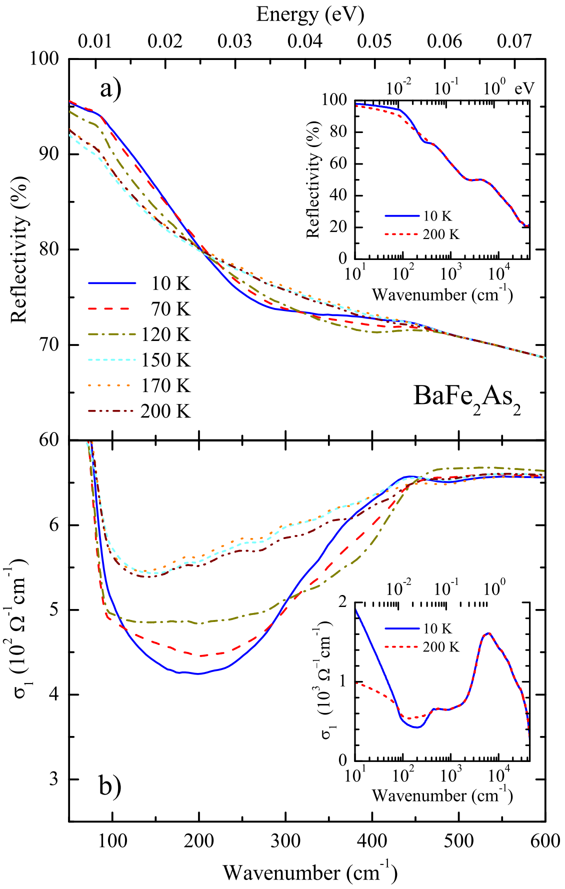

Figure 5.3: (a) Optical reflectivity and (b) real part $\sigma_1(\omega)$ of the optical conductivity as a function of temperature in the FIR spectral range. The insets in both panels show the same quantities at 10 and 200 K from FIR up to the ultraviolet spectral range with logarithmic energy scale.

frequency tail of the narrow Drude term of $\sigma_1(\omega)$. Such a redistribution of spectral weight governs the appearance of the depletion in both $R(\omega)$ and $\sigma_1(\omega)$ between 100 and 400 cm^{-1} below T_{SDW} (Fig. 3).

In conclusion, we have provided a comprehensive analysis of the excitation spectrum in BaFe$_2$As$_2$, with respect to its SDW phase transition. Our data reveal the formation of a pseudogap excitation in FIR and the narrowing of the metallic contribution in $\sigma_1(\omega)$ at T_{SDW}, which tracks the behavior of the *dc* transport properties. The opening of the pseudogap below T_{SDW} may suggest a Fermi surface nesting as driving mechanism for the SDW transition.

5.3 Optical properties of TiN thin films close to the superconductor-insulator transition

F. Pfuner and L. Degiorgi
work in collaboration with T. I. Baturina, Institute of Semiconductor Physics, Novosibirsk, Russia

The competition between localization and superconductivity can result in peculiar ground states. One of them is the so-called Bose-insulator, which is formed by localized Cooper pairs. It is a common notion that the superconducting ground state is characterized by long-range phase coherence and the possibility of non-dissipative charge transport. On the contrary, disorder acts in opposite direction, as it favors the repulsive part of the electron-electron interaction and the consequent localization of the electron wave function, so that the long-range phase coherence of the Cooper pairs is suppressed in the Bose-insulating state. At zero temperature the transition between these two phases, the so-called superconductor-insulator transition (SIT), is purely driven by quantum fluctuations and is the prime example of a quantum phase transition. Experimentally, the SIT can be realized in thin films, by decreasing their thickness and close to the critical thickness also by magnetic field. The investigation of disordered superconducting films is then of fundamental importance to understand the impact of electron-electron interaction and disorder itself on the ground state of many-body systems. Moreover, films are suitable playground to address those issues, since a system approaching the two-dimensional limit is close to the lower critical dimension for both localization and superconductivity.

TiN films recently gained a lot of attention and seem to be well-suited for the study of the above issues. Little is known about the electrodynamic response of such films at the verge of a SIT. In our work, we specifically address the normal state properties of TiN thin films from the perspective of their optical properties, covering a broad spectral range, extending well above the THz regime. We performed reflectivity ($R(\omega)$) measurements of the multilayers structure from the far infrared up to the ultraviolet (UV), i.e. 5 meV - 7 eV, as a function of temperature (2-300 K). Figure 4 displays the $R(\omega)$ spectra at 300 K of four multilayer specimens, while the inset shows the $R(\omega)$ measurement of the Si-wafer, acting as the substrate of the TiN thin films. We did not observe any temperature dependence of $R(\omega)$ in the energy interval covered by our investigations, in agreement with the weak temperature dependence of the *dc* transport properties above 4 K and suggesting that low energy scales may govern the electronic properties of TiN.

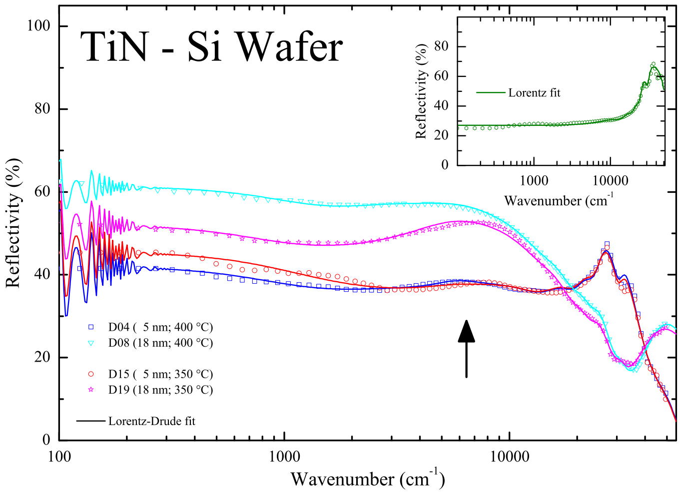

Figure 5.4: Optical reflectivity $R(\omega)$ at 300 K for the four investigated multilayer specimens. Inset: $R(\omega)$ at 300 K of the Si-wafer substrate. The thin lines in the main panel and inset correspond to the Lorentz-Drude fits. The arrow points out the mid-IR feature (see text).

The mid-infrared (IR) feature (arrow in Fig. 4), overlapped to the metallic component and below the onset of the electronic interband transitions occurring above $\sim$ 1.5x10^4 cm^{-1}, is the most characteristic feature in the electrodynamic response of TiN films. It is very much reminiscent of similar excitations seen in a large variety of correlated materials, including the copper-oxide superconductors as well as the Kondo systems. In the high-temperature superconductors, such a mid-IR feature has been identified with a pseudogap-like excitation, which seems to have important implications in pair formation and the origin of which is still matter of debate. This characteristic feature has been the subject of a wide range of theoretical proposals: from those focused on superconducting pairing correlations without phase coherence to those based on some form of competing electronic order or proximity to a Mott state. Furthermore, polaron, disorder or the charge stripes were also advocated as possible assignment for the mid-IR peak in the electrodynamic response. For the time being, we may argue that truly itinerant charge carriers coexist with more (disorder-induced) localized charges at energy states below the mobility edge, giving then rise to the mid-IR pseudogap-like excitation. It remains to be seen how one can fully reconcile this mid-IR excitation with the electronic and even the superconducting properties of TiN. Of interest in this respect might be the investigation of the spectral weight redistribution both as a function of temperature and magnetic field between high and low energy scales, when crossing the SIT.

Chapter 6

Solid-State Dynamics and Education

(http://www.eduphys.ethz.ch/)

Head
Prof. Dr. Andreas Vaterlaus

Academic Staff
Andreas Fognini
Dr. Thomas Michlmayr
Dr. Yves Acremann
Dr. Guillaume Schiltz
Martin Mohr
Dr. Audra Baleisis
Dr. Christian Helm

Technical Staff
Rouven Mühlethaler
Thomas Bähler

Administrative Staff
Brigitte Abt

Master Theses
Samuel Miesch

6.1 Ultrafast demagnetization processes observed with free electron laser radiation

Y. Acremann, A. Fognini, Th. Michlmayr, U. Ramsperger, and A. Vaterlaus

Conventional manipulation of the magnetization involves magnetic field pulses, created by current flow through wires. Today such current pulses are typically limited to timescales of tens of picoseconds and faster manipulation of the magnetization requires a different approach. One of the forefront areas in modern magnetism is the use of ultrashort infrared or optical photon pulses to manipulate the magnetization. Since optical photons trigger the sample through electronic excitations, the fundamental questions revolve around the processes and timescales associated with energy and angular momentum transfer between the three fundamental thermodynamic reservoirs of the sample: the electronic system, the spin system and the lattice. In the past, typical experiments involved optical pump-probe schemes where the laser pump excitation is probed at variable delay time by a second laser pulse.

By probing the results of optical excitations of magnetic samples via the magneto-optic Kerr-effect or x-ray circular magnetic dichroism, surprising phenomena have been observed. One phenomenon is the ultrafast loss of the spontaneous magnetization in Ni and Co after infrared pumping on the 10 - 100 femtosecond time scale. Another is ultrafast all-optical magnetic switching using circularly polarized photons. The pathway of the angular momentum from the spin system to the lattice as well as the role of the optical pump pulse is not understood.

Free electron laser radiation offers new possibilities to investigate dynamics in solids. We are preparing two experiments to investigate ultrafast magneto-dynamics in ferromagnetic solids. The first approach is based on spin polarized photoemission. The most direct way to measure the magnetization of a ferromagnet is by detecting elastically emitted photoelectrons and determining their spins. If the photon energy is sufficient the detected spin polarization of all the valence electrons only depends on the magnetization and is independent of the band structure. Therefore we will be able to directly measure the magnetization of the laser-excited sample. We successfully applied for beamtime at the free electron laser in Hamburg (FLASH) and are currently developing the experimental setup. This involves the design of the electron optic system, the vacuum chamber (including in-situ sample fabrication) as well as the integration into the data acquisition system at FLASH. The same experimental setup will be used in a laser based experiment at ETH.

The second experiment is targeted towards the nanostructure of the laser generated excitations. The coherence properties combined with the extreme peak intensity of FEL radiation offers the unique opportunity of single shot imaging with nanometer scale spatial resolution. We are involved in a collaboration with SLAC (Stanford) to image the magnetization distribution of a ferromagnet during and short after a pump laser pulse. Our contributions are in the aspects of laser to FEL synchronization, consulting in sample fabrication issues as well as software development. The first beamtime has been scheduled for July 2010.

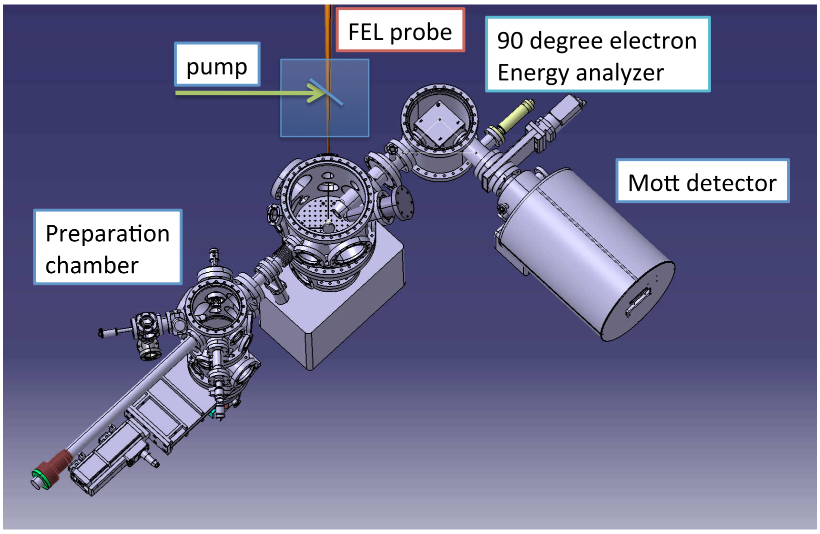

Figure 6.1: Experimental setup for the spin and time resolved photoemission experiment at the free electron laser in Hamburg (FLASH). The sample will be prepared in situ and transferred to the measurement chanber. There the 800 nm pump beam will excite the magnetization which will be probed by the FEL beam at 7 nm. Photoelectrons will be energy analyzed and their spin polarization detected by a Mott polarimeter.

6.2 Magnetic Properties of Gold-Capped and Uncapped Fe Layers on W-(110)

Th. Michlmayr, S. Miesch, A. Fognini, Y. Acremann, and A. Vaterlaus

Considering ultrathin layers of iron on tungsten W(110) as a sample for measurements at the free electron laser site FLASH in Hamburg requires elaborate studies of their magnetic properties beforehand. The FLASH experiments can be crucial for the understanding of ultrafast magnetodynamics processes such as the demagnetization of a magnetic structure within a few hundreds of femtoseconds time. The quest for answers regarding fundamental questions in solid state physic like this ultrafast spin angular momentum transfer to the lattice is assisted by preliminarily investigations in-house at the ETH Zurich. Thin film deposition - in the order of 5 to 25 monolayers (ML) - by molecular beam epitaxy (MBE) of iron on the clean and well ordered (110)-surface of a tungsten single crystal provides a reproducible sample with reliable qualities. Scanning electron microscopy with polarization analysis (SEMPA) and magnetooptical Kerr effect (MOKE) reveal that the coercive field -i.e. the smallest external magnetic field necessary to reverse the magnetization of the sample - for film thicknesses from 10 ML to 25 ML is almost constant and has a value between 15 Oe and 12 Oe. But it increases dramatically as the film thickness decreases. At a film thickness of 7 ML the necessary field is 72 Oe. A broad plateau in the coercive field dependency on the film thickness is very eligible. Exposed to air at atmospheric pressure the flimsy iron layer would oxidize within an instant and forfeit its ferromagnetic behavior. To prevent the iron film from oxidation the sample is covered with a thin layer of protective gold. This protection layer is also only a few monolayers thick. Beside this protecting property the gold layer also provokes a thickness dependent change in the coercive field of the underlaying iron film. For example a gold layer of 0.45 ML thickness leads to a change of the coercive field of +11 Oe but a gold layer of 0.73 ML changes the coercive field of the iron layer of only +4.1 Oe. And for gold layer thicknesses above 0.8 ML no changes are observed for the coercive field of the iron film. The gold layer does not provide a consummate protection against oxidation for all time. Namely the sample is still subjected to an aging process when exposed to air. An only 1.52 ML thick gold capping on 10 ML Fe on W(110) protects the sample in a way that still after 3 days on air the sample has a measurable coercive field but it increased to 125 Oe from former 42 Oe for the fresh sample. A 3.64 ML gold protection layer on 20 ML Fe on W(110) does a far better job because it has the effect that the coercive field only increased from 16 Oe to 19 Oe during exposing the sample to air for one day. Another characteristic of the sample one would like to know is the semi-static behavior of the coercive field. That is how the necessary magnetic switching field strength when applied as a single field pulse depends on the pulse length. The investigated pulse times would cover the scale from a few microseconds up to seconds.

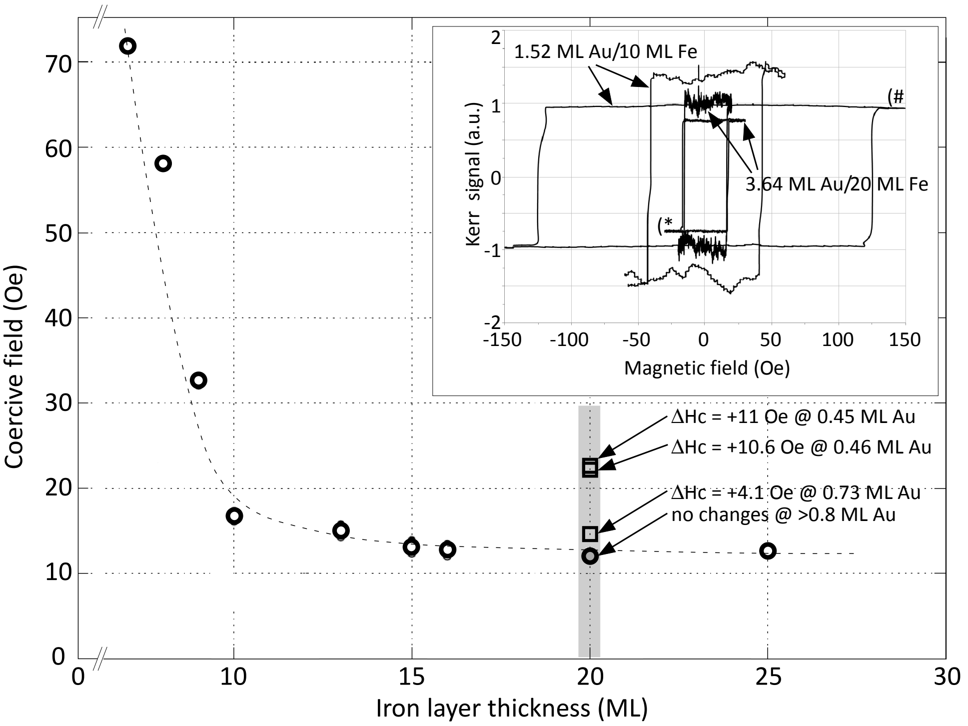

Figure 6.2: SEMPA and MOKE measurements of Fe ultrathin films evaporated on W(110). Open circles denote the coercive field for different Fe film thicknesses. For the Fe film thickness of 20 ML (gray bar) the effect on the coercive field by gold capping in the submonolayer scale is shown (open squares). The inset presents MOKE-hysteresis loops for gold capped samples on air with different exposing times that are three days (#) and one day (*).

6.3 Real World Physics

G. Schiltz, A. Lichtenberger, and A. Vaterlaus

The “filep” project “Real World Physics” was designed in order to illustrate selected concepts out of the physics 1 course for engineers in everyday life. Energy conservation and rotating reference systems were chosen as an example. In the framework of an E-Learning unit students described an everyday situation in which they observed the physical principle which was discussed in the physics course. They documented this situation with the help of pictures or short movies. In a report the observed effect was described and explained with the help of the theory, which was part of the physics curricula. The projects which were handed in ranged from the observation of a pendulum in a train running around a curve to a detailed consideration of energy conservation for a jojo. This second project turned out to be far from trivial, since the axis of rotation changes at the deepest point. In the end this group was able to simulate the measured movement of the jojo quiet accurately (Fig. 6.3). This work was counted as one experiment in the “Anfängerpraktikum”.

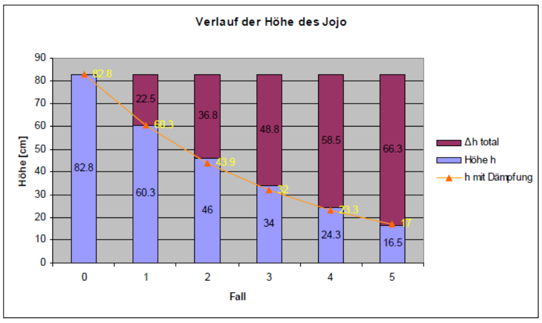

Figure 6.3: Measured and calculated maximal hights of the jojo for 5 initial swings. (source: F. Henschel and D. Heinzelmann, Physics 1, "Physik auf dem Pausenplatz")

6.4 E-Learning

G. Schiltz

6.4.1 Strategic activities

In 2009 the learning management system Moodle was introduced in 9 courses at the department. 5 introductory lectures (service and internal), 2 pedagogical lectures and 1 physics lecture with a total of 1Õ882 students were affected. Moodle was mainly used to support the course organization and to serve as a repository for course material. For some lectures, however, supplementary pedagogical scenarios, such as self-assessment tests, formative evaluations and collaborative tasks have been set up.

(in den letzten 5 Minuten)
Guillaume Schiltz

Es liegen keine neuen Mitteilungen vor
Mitteilungen...

Themen für jede Woche

Allgemeine Hinweise
- ETH Life: Selbststudium
- Übungsgruppen
- Raumverteilung
- Testatbedingung
- Link zur Webseite zu Physik I (HS 2008)

Foren
- Fragen zur Vorlesung
- Tipp-Boerse
- Gruppenforum
- Organisatorisches

Lernmaterial
- Skript Physik 1
- Skript Physik 2
- Nachlesung (Podcast mit Zusammenfassung der VL)

Umfrage zum Podcast (bitte beteiligen Sie sich auch an dieser Umfrage, wenn Sie den Podcast noch nie benutzt haben)
- Zur Podcast-Umfrage

Pruefungsstatistik Sommersession 2009

16. Februar - 22. Februar
Themen am 17. Feb 09:

Organisatorisches; Kurze Zusammenfassung der letzten VL im HS08: Vergleich klassische und relativ. Mechanik; Drehimpuls; Drehmoment; Drehimpulserhaltung, Flaechensatz; Einstieg Kap. Vielteilchensysteme

Nachlesung Woche 15
Zusammenfassung der Vorlesungen vom 26. Mai 2009
Nachlesung Woche 14
Zusammenfassung der Vorlesungen vom 19. Mai 2009

8. Okt, 19:11
Johannes Quirin Weitzel
Finaler Termin zur Klausureinsicht mehr...

10. Aug, 10:12
Isabel Vera Gudrun Braun
Klausur mehr...

5. Jun, 12:23
Guillaume Schiltz
Alle Podcast-Folgen mehr...

25. Mai, 15:46
Günther Dissertori
Testklausur mehr...

22. Mai, 18:54
Isabel Vera Gudrun Braun
Gespraechskreis 28. Mai mehr...
Ältere Beiträge ...

Figure 6.4: Moodle course

6.4.2 Filep projects

- "Real World Physics" (A. Vaterlaus) already launched in 2008 was successfully continued in 2009 (see above).
- "Brückenpodcast" (W. Wegscheider) was launched in 2009. This project aims at summarizing the physics introductory lectures by a weekly published podcast, including audio and visual material. Besides bridging the weekly lectures, students used the podcast episodes for preparing their exams. The podcast was first introduced in the physics lecture of G. Dissertori and has been positively evaluated within the project "Selbststudium an der ETH".
- "Erweiterte Physik-Vorlesungsexperimente" (B. Batlogg) could be reactivated in 2009. Jonathan Hanselmann, a teacher student from the department, was appointed at 50% to supervise the content production (videos and documentation).

Figure 6.5: Brückenpodcast on a mobile device

6.4.3 Promotion and Network

The e-learning activities pursued at the department have been communicated to a greater public and were abundantly discussed in the community at four different events (2 ETH-internal, 2 external).

6.5 Modern Physics for Schools

T. Michlmayr, T. Bähler, R. Mühlethaler, A. Vaterlaus

In an attempt to bring experiments which illustrate modern physical concepts to schools, the department of physics did purchase seven Scanning Tunneling Microscopes (STM) for the use in secondary level 2 ("Gymnasium") classes. An introductory educational unit was prepared which gives an insight into the technique and the basic physical principles. A visit at a school normally compasses a introductory lesson with examples from research in solid state physics and two hours of practical work. The aim of the practical work is to image a surface (normally graphite) with atomic resolution. This does require a careful preparation of a tunneling tip and of the sample surface. Figure 6.6 shows a 1,5 nm by 1,5 nm STM image of a graphite surface imaged in a class room. In 2009 this educational program was used at six advanced trainings for practicing teachers, it was used in 11 classes at different schools, at the "Nacht der Forschung" and in two courses at the ETH in Zürich. In addition one STM was used during a "Maturaarbeit" and the whole program was presented at the general assembly of the ZHSF (Zürcher Hochschulinstitut für Schulpädagogik und Fachdidaktik).

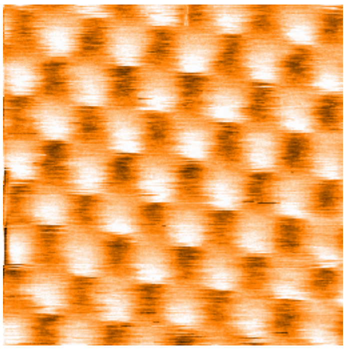

Figure 6.6: 1,5 nm by 1,5 nm STM image of a graphite surface imaged in a class room.

Chapter 7

Quantum device lab

(http://qudev.ethz.ch/)

Head

Prof. Dr. A. Wallraff

Academic Staff

M. Baur
S. Berger
R. Bianchetti
D. Bozyigit
S. Burch
C. Eichler
Dr. S. Filipp
J. Fink
T. Frey
Dr. M. Göppl
C. Lang
Dr. P. Leek
J. Mlynek
G. Puebla-Hellmann
S. Schmidlin
L. Steffen
P. Studer
A. van Loo

Technical Staff

H. Aeschbach

Administrative Staff

G. Strahm

PhD theseses

M. Göppl	FS 2009

Master theseses

S. Schmidlin	FS 2009
S. Burch	FS 2009
C. Lang	FS 2009

7.1 Autler-Townes and Mollow transitions in a strongly driven superconducting qubit

M. Baur, S. Filipp, R. Bianchetti, J. M. Fink, M. Göppl, L. Steffen, P. J. Leek and A. Wallraff
in collaboration with A. Blais, Université de Sherbrooke, Canada

When a two-level system is driven on resonance with a strong monochromatic field, the excited state population undergoes coherent Rabi oscillations. This coherent process is reflected in the appearance of two sidebands offset by the Rabi frequency from the main qubit transition in the spectrum. This leads to a three peaked fluorescence spectrum referred to as the Mollow triplet. When probing transitions into a third atomic level, two characteristic spectroscopic lines separated by the Rabi frequency appear, a feature which is called the Autler-Townes doublet.

In this work, we have used a pump-probe technique to observe these two effects in a superconducting transmon qubit acting as a multi-level artificial atom with the first three energy levels labeled as $|g\rangle$, $|e\rangle$ and $|f\rangle$. First, we drive the transition between the two lowest energy levels of the qubit at frequency $\nu_{ge} \approx 4.81\,\mathrm{GHz}$ with a strong microwave tone of a given amplitude ε. We then probe the qubit spectrum by sweeping a weak second microwave signal over a wide range of frequencies, including ν_{ge} and the frequency corresponding to the transition between the first and second excited state $\nu_{ef} \approx 4.55\,\mathrm{GHz}$, see Fig. 7.1(a). The possible transitions are detected using dispersive read-out of the qubit coupled off-resonantly to a microwave transmission line resonator. For large drive amplitudes, the Lorentzian line at frequency ν_{ef} splits into two, corresponding to the Autler-Townes doublet, see Fig. 7.2(a). Similarly, we clearly observe two sidebands emerging around ν_{ge}, corresponding to the sidebands of the Mollow triplet, see Fig. 7.2(b).

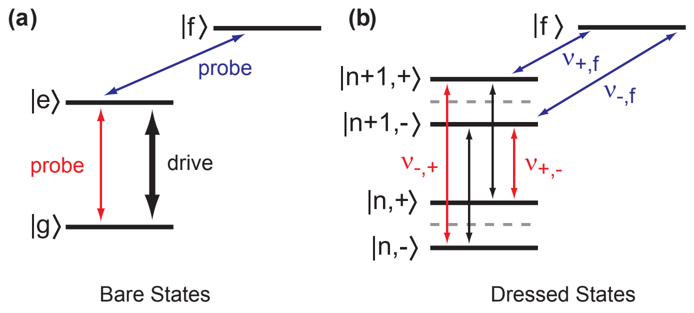

Figure 7.1: (a) Energy-level diagram of a bare three-level system. (b) Energy-level diagram of the dipole coupled dressed states with the coherent drive tone. Drive and probe transitions are indicated by black and red/blue arrows, respectively.

An intuitive model explaining those two effects can be given in the dressed state picture. In the situation, where the drive is exactly on resonance with the qubit, the bare states $|n,g\rangle$ and $|n-1,e\rangle$ of the uncoupled atom-field system are degenerate, where n is the average number of photons in the coherent drive. The dipole coupling splits the energy levels by the Rabi frequency $\hbar\Omega_R$ and forms an energy ladder of doublets separated by the energy of the drive photons $\hbar\omega_d$. The new dressed eigenstates dipole coupled to the field are symmetric and antisymmetric superpositions of the bare states $|n,\pm\rangle = |n,g\rangle \pm |n-1,e\rangle$, see Fig. 7.1(b). In the limit $n \gg \sqrt{n}$, the allowed transitions between dressed state doublets appear at frequencies $\omega_0 = \omega_{ge}, \omega_{+,-} = \omega_{ge} - \Omega_R$ and $\omega_{-,+} = \omega_{ge} + \Omega_R$ which are the central line and the two sidebands of the Mollow triplet, respectively, indicated by black and red arrows in Fig. 7.1(b). In contrast to atomic physics where these lines are usually detected in fluorescence, we do not observe the central line in our particular measurement scheme. Similarly, transitions from one pair of dressed levels $|n+1,\pm\rangle$ to the third level $|f\rangle$ at frequencies $\omega_{\pm,f} = \omega_{ef} \mp \Omega_R/2$ correspond to the Autler-Townes doublet.

In order to get a quantitative understanding of the dressed state splitting, the frequencies of the Autler-Townes doublet (blue data points) and of the Mollow triplet sidebands (red data points) have been extracted from the Lorentzian fits in Fig. 7.2(a) and (b) are plotted in Fig. 7.2(c). The splitting of the spectral lines in pairs separated by Ω_R and $2\Omega_R$, respectively, is observed for Rabi frequencies up to $\Omega_R/2\pi \approx 300\,\mathrm{MHz}$. The resulting frequencies can be perfectly explained for all driving amplitudes by a generalized Jaynes-Cummings model, which takes into account higher excited qubit states and level shifts (solid black lines). This work demonstrates the good understanding of this quantum system beyond the two-level approximation. It also indicates the potential of using higher excited states for new quantum optics experiments and new schemes for gate operations in quantum information processing.

7.2 Dynamics of dispersive single qubit read-out in circuit quantum electrodynamics

R. Bianchetti, S. Filipp, M. Baur, J. M. Fink, M. Göppl, P. J. Leek, L. Steffen and A. Wallraff
in collaboration with A. Blais, Université de Sherbrooke, Canada

High-fidelity readout of the qubit state is an important aspect of all experimental efforts in quantum information science. In the circuit quantum electrodynamics (QED) architecture, where a superconducting qubit is strongly coupled to a transmission line resonator, the qubit can be both controlled and read-out via the cavity using microwave signals. The system of the qubit described by the operators $\hat{\sigma}_{\mathrm{i}}$ ($\mathrm{i} = \mathrm{x,y,z}$), dispersively coupled to the resonator field operators $\hat{a}^{(\dagger)}$ is described by the dispersive Jaynes-Cummings Hamiltonian

$$H_{\mathrm{disp}} = \hbar(\omega_{\mathrm{r}} + \chi\hat{\sigma}_{\mathrm{z}})\hat{a}^{\dagger}\hat{a} + \frac{\hbar}{2}(\omega_{\mathrm{a}} + \chi)\hat{\sigma}_{\mathrm{z}}, \tag{7.1}$$

where the read-out is accomplished by detecting the dispersive qubit-state dependent shift χ of the resonator frequency ω_r in a transmission amplitude measurement. The dynamics of the resonator-qubit system is probed by performing a time resolved, phase sensitive measurement of the resonator transmission at different frequencies ω_{m}. Figure 7.3a) shows the pulse scheme used for the measurement. A 10 ns long resonant π pulse is applied to excite the qubit while the resonator is constantly driven. Figure 7.3b) and c) show the transmitted in-phase (I) and quadrature (Q) amplitudes, averaged 650'000 times. The dependence of the quadrature components I and Q on the detuning Δ_{mr} of the measurement frequency from the bare resonator frequency is plotted in Figs. 7.3d) and e). The shift of the resonance frequency by χ during the qubit lifetime γ is clearly visible in this representation.

To quantitatively study the dynamics of the system, we derive Bloch-like equations of motions for the expectation value of the qubit and the resonator field operators. The time and frequency dependence of the measurement signal is accurately described by this theory with a single set of independently measured, non adjustable parameters as indicated by the solid lines.

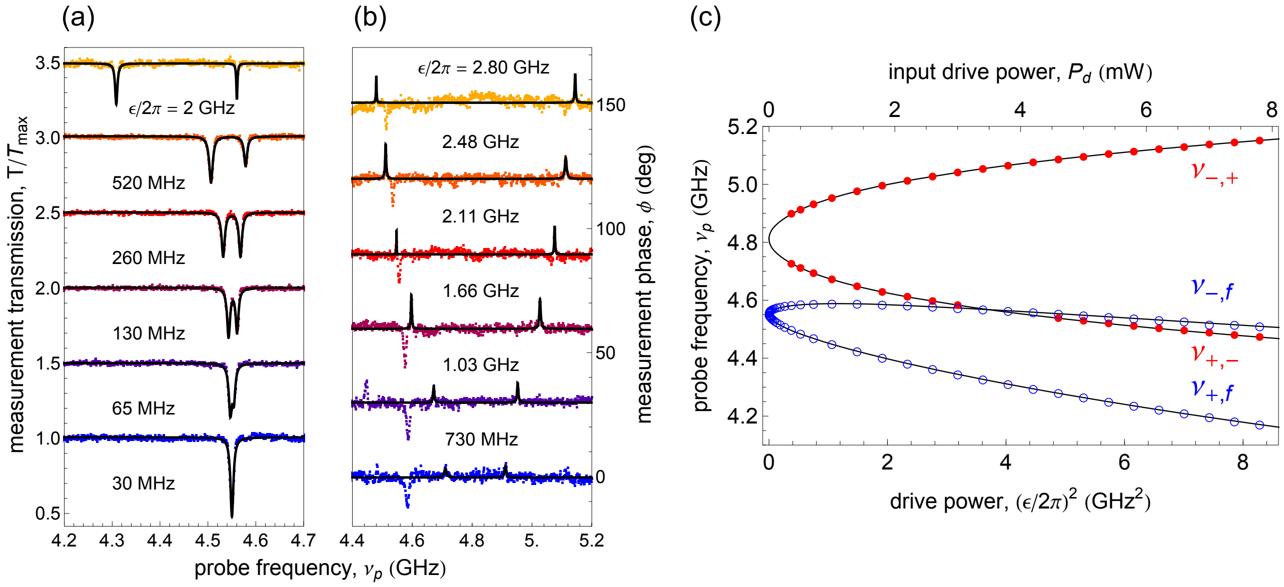

Figure 7.2: Autler-Townes (a) and Mollow spectrum (b) for selected drive amplitudes ε. (c) Autler-Townes doublet (open blue dots) and Mollow triplet sideband frequencies (solid red dots) versus drive power ε^2. Black solid lines are transition frequencies calculated by numerically diagonalizing a generalized Jaynes Cummings Hamiltonian taking into account the lowest 5 transmon levels.

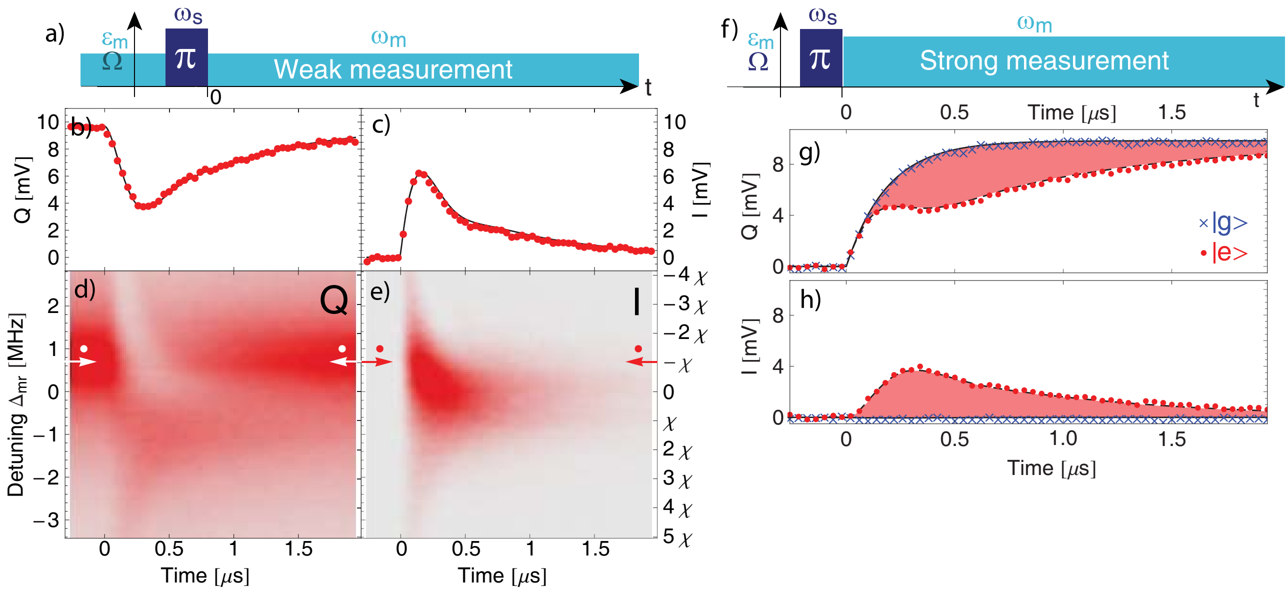

Figure 7.3: a) In a continuous measurement, the cavity is weakly driven with the qubit in its ground state. The qubit is then prepared in the excited state with a π-pulse ending at $t = 0$. b) and c) averaged measurement response Q, I versus time t for a continuous weak measurement at the frequency $\omega_{\mathrm{m}} = \omega_{\mathrm{r}} - \chi$. Solid lines show the calculated response. Time resolved data taken at different detunings Δ_{mr} is shown in d) and e). The arrows indicate the detuning at which the data shown in b) and c) is taken. f) Pulsed measurement scheme where the strong measurement starts after the qubit excitation. g),h) Measurement response versus time for a pulsed averaged measurement for the Q and I quadrature, respectively. Red points show the response for the qubit being prepared in the excited state $|e\rangle$. The blue crosses are the measured response to the qubit prepared in $|g\rangle$.

To avoid measurement-induced dephasing during the qubit manipulation most of the recent circuit QED experiments have been performed by probing the qubit state with pulsed measurements. In contrast to a continuous measurement, the measurement tone is switched on only after the qubit state preparation is completed, see Fig. 7.3f) for the pulse scheme. With the qubit in $|g\rangle$ the resonator response reaches its steady state at the rate κ, which is seen in the exponential rise of the Q quadrature, see blue crosses in Fig. 7.3g). Since the resonator is measured on resonance at its pulled frequency $\Delta_{\mathrm{mr}} = -\chi$, the I quadrature is left unchanged, see blue crosses in Fig. 7.3h). As in the continuous case, the resonator frequency is pulled to $\omega_{\mathrm{r}} + \chi$ when the qubit is prepared in $|e\rangle$, see red dots in Figs. 7.3g) and h).

The detailed understanding of the dynamics of the dispersively coupled qubit/resonator system can be used to infer the qubit excited state population $p_e =$

$(\langle\hat{\sigma}_z\rangle + 1)/2$. Indeed, the difference in the measured response for a given unknown state $s_\rho(t)$ and the ground state response $s_g(t)$, which corresponds to the shaded area indicated in Fig. 7.3g) and h), is directly proportional to p_e. In the linear regime, with only a few photons populating the resonator, mixing transitions between the two qubit states can be neglected and thus, this method implements a projective quantum non-demolition measurement.

To test our method experimentally, we perform a Rabi-oscillation experiment, where a pulse of variable length τ and amplitude Ω is applied at the effective qubit transition frequency $\omega_{\mathrm{s,res}}$. The expected population of the qubit in the limit of large driving fields ($\Omega \gg \gamma_1, \gamma_\phi$) is:

$$p_e(t) \cong \frac{1}{2} - \frac{1}{2}e^{-\frac{t}{4}(3\gamma_1+2\gamma_\phi)}\cos(\Omega t/2). \tag{7.2}$$

Indeed, the population p_e obtained with the area method (Fig. 7.4, points) has an rms deviation of less than 1% from the population predicted by Eq. (7.2) (Fig. 7.4, solid line).

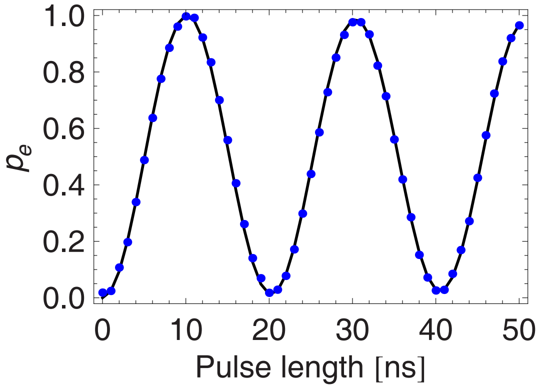

Figure 7.4: Rabi oscillations of the qubit population p_e reconstructed by analyzing the pulsed Q response of the resonator (dots). The black line corresponds to the theoretical prediction.

In this work, we have presented a simple set of equations describing the dynamics of the average values of the quadrature amplitudes of the transmitted microwave fields in dependence on the qubit state in a circuit QED setup operated in the dispersive regime finding excellent agreement with the measured data. From the time dependent measurement response we reconstruct the qubit excited state population that is used in tomographic measurements to accurately measure both single and two-qubit density matrices.

7.3 Two-qubit state tomography using a joint dispersive read-out

S. Filipp, P. Maurer, P. J. Leek, M. Baur, R. Bianchetti, J. M. Fink, M. Göppl, L. Steffen and A. Wallraff
in collaboration with J. Gambetta, University of Waterloo, Canada and A. Blais, Université de Sherbrooke, Canada

In solid state systems, recent advances have enabled the precise coherent control of individual quantum two-level systems embedded in a superconducting environment. In particular, the coupling of superconducting qubits to a coplanar transmission line resonator, an architecture known as circuit QED, allows for strong coupling between qubits and the electromagnetic field generated by single photons in the resonator, while providing at the same time efficient shielding from the environment. In this system, high fidelity qubit manipulations enable the creation of two-qubit entangled states by addressing transitions of individual qubits via directly applied microwave signals and by using resonator photons to mediate interactions for two-qubit quantum operations.

Precise coherent control of quantum states relies on the ability to complete characterize an a priori unknown state. The availability of a high-fidelity state tomography, a method that allows for the full reconstruction of the quantum state from a set of measurements on identically prepared systems, is therefore a crucial requirement for applications in quantum information processing. In our experiments we have generated a complete set of Bell states using a pulse sequence based on sideband transitions that entangles first one qubit with the resonator and subsequently distributes the entanglement between two qubits (see section 7.6). These entangled states are then characterized by a joint readout based on a transmission measurement of the dispersively coupled resonator.

In circuit QED the read-out is accomplished by a transmission measurement of the dispersively coupled resonator, which distinguishes between different states of the qubit (see section 7.2). For two qubits coupled to the same resonator mode, this scheme allows to assess the combined state of the qubits employing the resonator as a single measurement apparatus. The coupling between the qubits and the resonator leads to a dispersive shift of the resonance frequency depending on the state of both qubits, see Figure 7.5(a). For the successful measurement of correlations between two spatially separated qubits it is essential that the measured signal depends non-trivially on the qubit states. The measurement response to a state change in one qubit must be correlated to the state of the respective other qubit; only in this case information can be obtained about qubit-qubit correlations without individual qubit-readout. Indeed, as shown in Figure 7.5(b), a measurement of the transmission amplitude Q at a frequency ω_m depends non-linearly on the shifts, i. e. the observed amplitude difference after exciting one qubit with the other in the ground state, δQ^g, differs from the amplitude difference δQ^e, when the other qubit was in its excited state before ($\delta Q^e \neq \delta Q^g$). This difference leads to an entanglement-sensitive measurement and can be used to reconstruct the full density matrix of the state. In order to determine all parameters of the density matrix representing the qubit state, the experiment has to be repeated at least 15 times with identically prepared states, but different measurements, see Figure 7.5(b). Although the measurement itself is fixed, determined by the dynamics of the system, we utilize the fact that a rotation of the state prior to the measurement is equivalent to performing a different measurement. From the outcomes of these 15 measurements, i. e. different rotations, the state can be determined unambiguously. The reconstructed density matrices (Figure 7.5(c)) confirm the successful preparation of entangled quantum states between two superconducting circuits.

In conclusion, we have demonstrated a method to jointly and simultaneously read-out the quantum state of two qubits dispersively coupled to a microwave resonator. In this way two-qubit correlations can be extracted from an averaged measurement of the transmission amplitude without the need for single shot and single-qubit read-out, which enables the reconstruction of any correlated two-qubit state from a quantum non-demolition measurement. This method can also be extended to the read-out of higher qubit excitations and multiple qubits coupled to the same resonator mode.

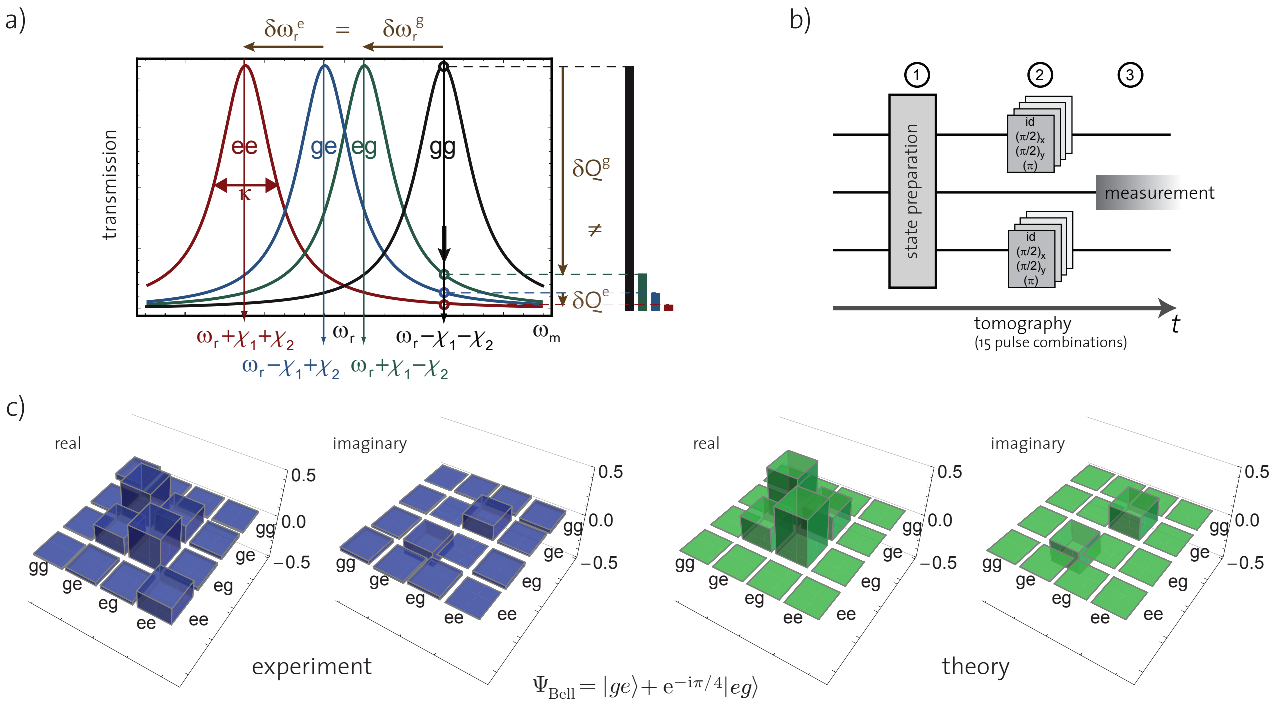

Figure 7.5: (a) The dispersive coupling of two qubits to a transmission line resonator of linewidth κ leads to a shift $\delta\omega_r$ of the resonance frequency ω_r depending on the respective states of the qubits. Each qubit i shifts the resonator by $-\chi_i$ or $+\chi_i$ if in its ground or excited state, respectively. In (b) the scheme for the state tomography is shown. The state preparation (1) is followed by a specific rotation of the state (2) prior to measurement (3). The whole sequence is repeated 15 times with different rotations on identically prepared input states. From these measurement results the density matrix of the input state, a maximally entangled Bell-state, is reconstructed. Its entries are graphically shown and compared to the theoretically expected state in Figure (c).

7.4 Collective multi-qubit interaction

J. M. Fink, R. Bianchetti, M. Baur, M. Göppl, L. Steffen, S. Filipp, P. J. Leek and A. Wallraff
in collaboration with A. Blais, Université de Sherbrooke, Canada

Collective phenomena are well known in physics and some prominent examples include Cooper pairs in a superconductor, photons in a laser beam and atoms in a Bose-Einstein condensate. Already in the early 1950's R. H. Dicke realized that similarly a gas of radiating molecules can under appropriate circumstances show collective behavior and thus the properties of all atoms have to be collectively described as a single joint quantum system.

We report an experiment which shows the coherent interaction of multiple artificial atoms (N) - up to three superconducting electrical circuits fabricated on a microchip with ground states $|g\rangle$ and excited states $|e\rangle$ - with one microwave photon (n) contained in an on-chip transmission line resonator (circuit QED). Here both the atoms and the photons form a new entangled system - half matter half light - where the resonator and the individual atom exchange a single quantum of energy 170 million times per second. Quantum theory predicts this rate to be enhanced by a factor $\sqrt{N}$ if multiple atoms couple collectively to the photon. This effect was observed in the reported work by adding interacting atoms (A, B and C) one-by-one in a fully controlled fashion, see Fig. 7.6 to the cavity mode.

While previous investigations suffered from the difficult spatial control of individual natural atoms in a cavity, we demonstrate this effect in a fully locally and globally controlled matter-light quantum system. The development of such electrical quantum circuits represents a promising route towards the realization of a future quantum information processor since they provide the high degree of control that is needed to repeatedly manipulate individual quantum bits. At the same time the reported experiment shows that collective interactions provide a very convenient and scalable way to create nontrivial collective quantum states interesting both for quantum information processing and quantum communication.

7.5 Thermal excitation of multi-photon dressed states

J. M. Fink, M. Baur, R. Bianchetti, S. Filipp, M. Göppl, P. J. Leek, L. Steffen and A. Wallraff
in collaboration with A. Blais, Université de Sherbrooke, Canada

The exceptionally strong coupling realizable between superconducting qubits and photons stored in an on-chip microwave resonator allows for the detailed study of matter-light interactions in the realm of circuit quantum electrodynamics (QED). Here we investigate the resonant interaction between a single transmon-type multilevel artificial atom and weak thermal and coherent fields. While the observation of the simple vacuum Rabi mode splitting for $n = 1$ photons could in principle be interpreted as a normal mode splitting using a classical model, the observation of additional transitions to higher excited dressed states is an unambiguous signature for the quantum nature of the system. We report a direct spectroscopic observation of this characteristic quantum nonlinearity. In the

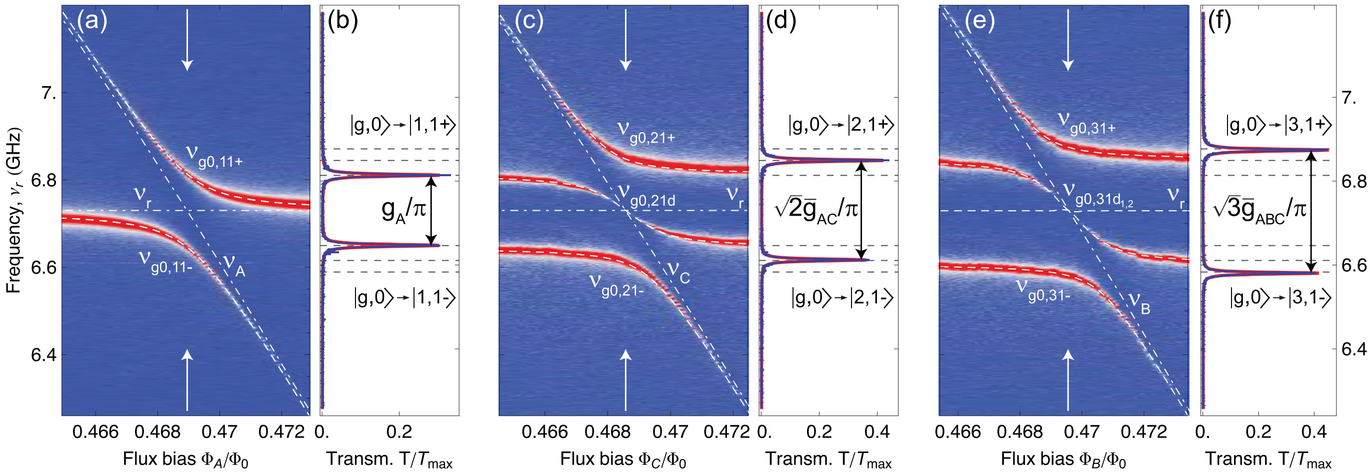

Figure 7.6: Vacuum Rabi mode splitting with one, two and three qubits. (a) Measured resonator transmission spectrum T (blue, low and red, high transmission) versus normalized external flux bias Φ_A/Φ_0 of qubit A. Dash-dotted white lines indicate bare resonator ν_r and qubit ν_A frequencies and dashed white lines are calculated transition frequencies $\nu_{g0,Nn\pm}$ between $|g,0\rangle$ and $|N,n\pm\rangle = 1/\sqrt{2}(|g,1\rangle \pm |e,0\rangle)$. (b) Resonator transmission T/T_{max} at degeneracy normalized to the maximum resonator transmission T_{max} measured at $\Phi_{A,B,C} = \Phi_0/2$ (not shown), as indicated with arrows in (a). Red line is a fit to two Lorentzians. (c) Resonator transmission spectrum T/T_{max} versus external flux bias Φ_C/Φ_0 of qubit C with qubit A degenerate with the resonator ($\nu_A = \nu_r$). (d) Transmission spectrum T/T_{max} at flux as indicated in (c). (e) Transmission spectrum versus flux Φ_B/Φ_0 with both qubits A and C at degeneracy ($\nu_A = \nu_C = \nu_r$). The white dashed line at frequency $\nu_{g0,31d_{1,2}} = \nu_r$ indicates the dark state occurring at degeneracy. (f) Transmission spectrum T/T_{max} at flux as indicated in (e).

presence of weak thermal fields we explore up to three photon dressed states $|n\pm\rangle = (|g,n\rangle \pm |e,n-1\rangle)/\sqrt{2}$ of the resonantly coupled system in a linear response heterodyne transmission measurement.

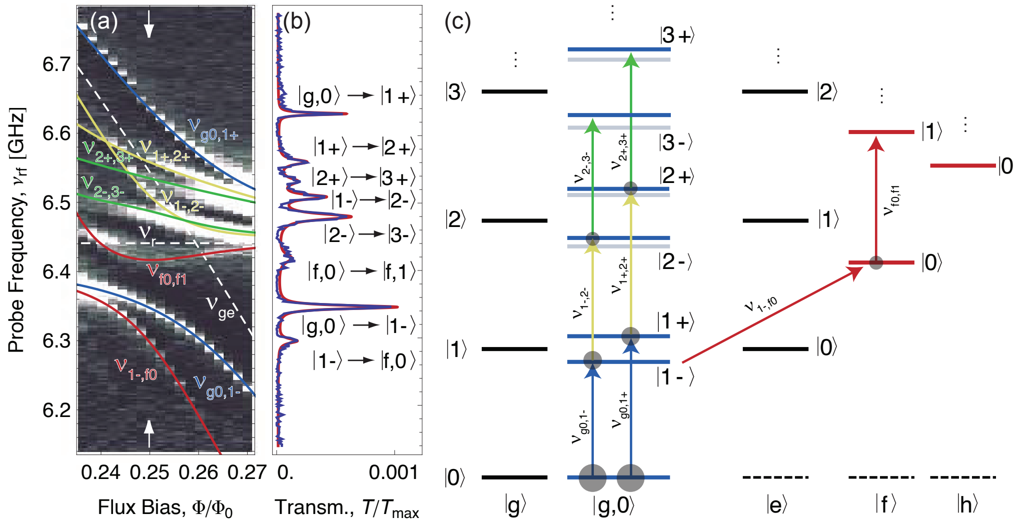

Figure 7.7: Vacuum Rabi mode splitting in the presence of a thermal field. (a) Measured resonator transmission spectra versus normalized external flux Φ/Φ_0 close to degeneracy with an additional quasi-thermal field applied to the resonator input populating the $|1\pm\rangle$, $|2\pm\rangle$ and $|f,0\rangle$ states. Black indicates low and white high transmission T. The solid lines show dressed state energies as obtained numerically and the dashed lines indicate the bare resonator frequency ν_r and the qubit transition frequency $\nu_{g,e}$. (b) Transmission spectrum at $\Phi/\Phi_0 = 0.25$, indicated by arrows in (a). (c) Corresponding energy level diagram of a resonant ($\nu_r = \nu_{g,e}$) cavity QED system. The uncoupled qubit states $|g\rangle$, $|e\rangle$, $|f\rangle$ and $|h\rangle$ (from left to right) and the photon states $|0\rangle$, $|1\rangle$, $|2\rangle$, $|3\rangle$, ... (from bottom to top) are shown with black and red solid lines. The dipole coupled dressed states including (not including) the shifts due to the $|f,0\rangle$ and $|h,0\rangle$ levels are shown in blue lines (gray lines). The observed transitions are indicated by arrows and the induced thermal population is indicated with gray circles.

Experimentally, the coupled circuit QED system is prepared in its ground state $|g,0\rangle$ by cooling it to temperatures below < 20 mK in a dilution refrigerator. In the presence of externally applied broadband quasi-thermal fields, we probe the cavity transmission spectrum as a function of flux in the anticrossing region, see Fig. 7.7a, with a weak probe tone ν_{rf} in the linear response limit. In this limit the weak probe tone is only a small perturbation to the field with a mean thermal photon number $\bar{n}_{\text{th}} \sim 0.3$ and no multi-photon transitions are induced. In this measurement we resolve all allowed transitions between the thermally occupied dipole coupled states in the generalized Jaynes-Cummings ladder. The solid lines are the calculated dressed state transition energies which agree well with the observed spectral lines. In Fig. 7.7b, a cavity transmission measurement at flux $\Phi/\Phi_0 = 0.25$ is shown. We identify 8 allowed transitions, compare with Fig. 7.7c. It follows that the states $|1\pm\rangle$, $|2\pm\rangle$ and also $|f, 0\rangle$ are thermally populated.

The results are in good quantitative agreement with a generalized Jaynes-Cummings model. It has been shown that cavity QED with superconducting circuits can be a sensitive probe for thermal fields. A more detailed quantitative analysis of the thermally excited vacuum Rabi spectra could be of interest in the context of environmentally induced dissipation and decoherence, thermal field sensing and the cross-over from the quantum to the classical regime of cavity QED.

7.6 Using sideband transitions for two-qubit operations in superconducting circuits

P. J. Leek, S. Filipp, P. Maurer, M. Baur, R. Bianchetti, J. M. Fink, M. Göppl, L. Steffen and A. Wallraff

Superconducting circuits are a promising candidate for realizing scalable solid state quantum computation. The architecture of circuit quantum electrodynamics (QED) is of particular importance in this field due to the potential to couple qubits over millimeter distances via photons on a transmission line resonator. In this work we investigate the use of sideband transitions to couple two qubits together via resonator photons, in a situation in which the qubit transition frequencies and resonator are all off-resonant from each other. This has the advantage that the on/off ratio of the coupling can be large (due to the systems being off-resonant), and that qubit frequencies can be separately chosen for good coherence. The level scheme for the qubit-resonator system is shown in Fig. 7.8. Blue sideband transitions involve simultaneous excitation of both qubit and resonator, while the red sideband would involve the exchange of an excitation between the two systems.

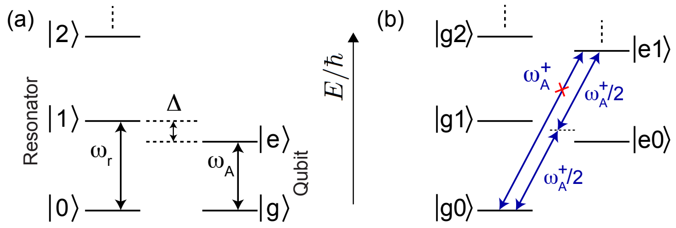

Figure 7.8: (a) Schematic of the resonator and qubit energy levels. (b) Combined level diagram, indicating the two-photon blue sideband transition.

In circuit QED, the sideband transitions are forbidden to first order, but may be accessed using two photons. Here we drive the blue sideband with two photons of equal energy, using a single microwave drive of frequency $\omega_{\text{A}}^{+}/2 = (\omega_{\text{r}} + \omega_{\text{A}})/2$ (see Fig. 7.8(b)), where ω_{r} and ω_{A} are the frequencies of the resonator and qubit respectively. Applying large amplitude pulses of microwave radiation resonant with the blue sideband transition of one qubit to a drive line (selectively coupled to the chosen qubit) shows coherent Rabi oscillations, as shown in Fig. 7.9(a). This allows the calibration of pulse length and amplitude for specific operations (for example a $\pi/2$ pulse entangles qubit and resonator), and was carried out also for the second qubit. We then implemented a pulse sequence to generate qubit-qubit entangled states (see fig. 7.9(b)). A resonant π-pulse is first applied to qubit B, generating the state $|ge0\rangle$. A $\pi/2$-pulse on the blue sideband of qubit A then generates the entangled state $(|ge0\rangle + e^{i\phi'}\,|ee1\rangle)/\sqrt{2}$. A π-pulse on the blue sideband of qubit B then generates the Bell state $|\Psi\rangle = (|ge\rangle + e^{i\phi}\,|eg\rangle)/\sqrt{2}$, with the resonator back in its ground state. Full reconstruction of the two-qubit state was then achieved using quantum state tomography disussed in section 7.3. An example of an experimental two-qubit density matrix corresponding to preparation of the state $|\Psi_{+}\rangle = (|ge\rangle + |eg\rangle)/\sqrt{2}$ is shown in Fig. 7.9(c).

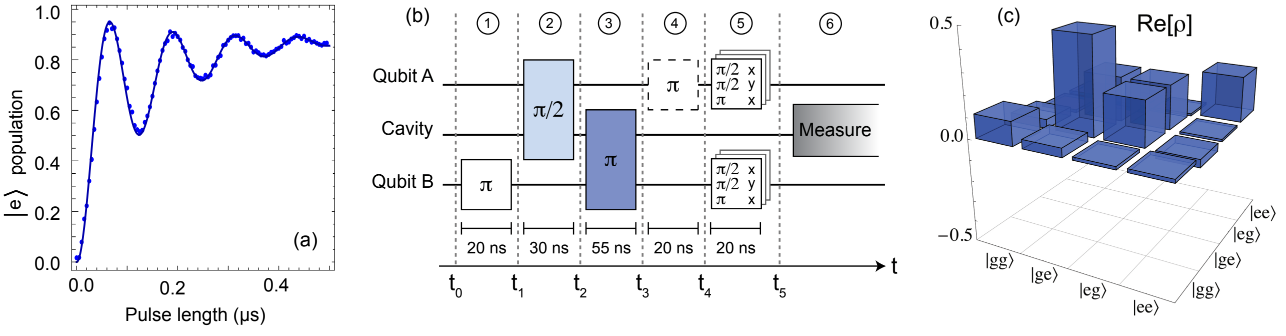

Figure 7.9: (a) Rabi oscillations on the blue sideband. (b) Pulse sequence for generation of a two qubit entangled state using sidebands. (c) Experimental density matrix of one of the generated states.

The fidelity of Bell states generated in 33 separate experimental runs was found to be $\mathcal{F} = 75 \pm 2\%$, and results showed very close agreement with simulations, indicating that we have a good understanding and control of the system. The dominant loss mechanism in the experiments was the photon lifetime, which has in later experiments already been improved. The scheme is potentially extendable to the implementation of a universal CNOT gate, and should scale well to a system with a larger number of qubits.

Chapter 8

Semiconductor Quantum Materials

Head
Prof. Dr. W. Wegscheider

Academic Staff
Dr. T. Feil
S. Peters
Ch. Charpentier
Ch. Reichl
A. Maier
W. Wüster

Technical Staff
J. Gmür

Administrative Staff
Ch. Egli

Overall Introduction

Werner Wegscheider

The newly formed group focuses on the design and fabrication of highest-purity semiconductor heterostructures utilizing molecular beam epitaxy (MBE). In addition, these heterostructures are studied by employing lasers, low-temperature cryostates and high magnetic fields. Examples of these heterostructures are highest-mobility two-dimensional charge carrier systems and other lower-dimensional systems (quantum dots) with applications in the field of quantum computing. While a large number of experiments are carried out either within the group or within ETH Zurich, samples are also provided for dedicated experiments to external collaborators.

8.1 Development of a New Inelastic Light Scattering Experiment

The recently renovated laboratories will host a novel type of inelastic light scattering experiment performed on ultracold ($\approx$ 10mK) high-mobility two-dimensional electron gas samples. The main parts of the experiment in form of a triple-spectrometer and a cryogen-free dilution refrigerator (equipped with a superconducting magnet) have been ordered and the overall setup has been fully designed. The objective of the experiment ist to gain insight into the elementary excitations of quasi-particles in the fractional quantum Hall effect regime.

8.2 Installation of a Facility for Molecular Beam Epitaxy of Highest Purity Semiconductor Structures

In the end of 2009, a MBE system previously installed at the University of Regensburg was transferred to ETH Zurich and installed. This MBE system allows epitaxial growth in the III-V material system (AlGaAs/GaAs/InAs) onto 2”-GaAs wafers. Available dopants are Si (n-doping) and C (p-doping). Excellent samples have already been produced with this MBE system at its previous location; electron mobilities reaching 20.000.000 cm^2/Vs - a value close to the current world record - were achieved. In addition to these conventional semiconductor heterostrucures, our lab will be able to produce self-assembled quantum dots as well as structures grown by cleaved edge overgrowth (CEO). So far, the system has been reassembled and cleaned and is now (March 2010) ready for bake out and recalibration. We expect to resume sample growth in early summer 2010. During summer 2010, an additional MBE system will be delivered to our labs, designed for the production of antimonide based high-mobility heterostructures (AlGaSb/GaSb/InAs).

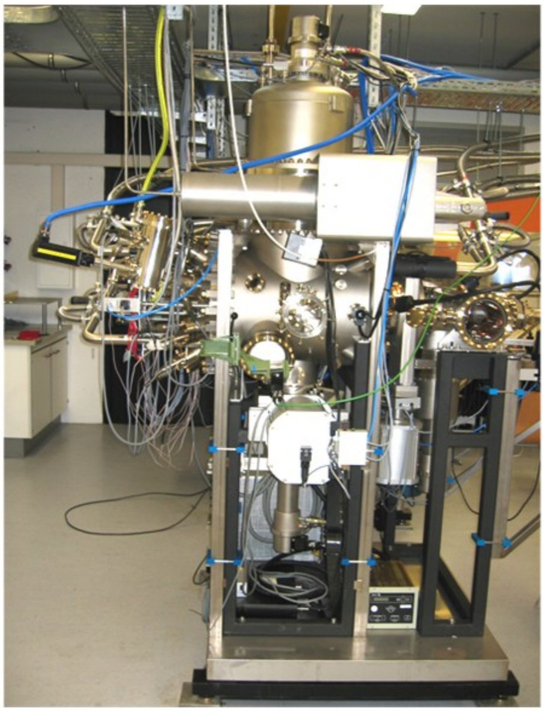

Figure 8.1: MBE Facility

8.3 Micro-Photoluminescence and Electroluminescence Investigations

Several optical setups were moved from the University of Regensburg to ETH Zurich to form a new optics laboratory. In addition to standard optical characterization in a wide temperature and wavelength window, the analysis of samples by photoluminescence with micrometer resolution (μPL) and the optical detection of spin accumulation created by the Spin-Hall effect in GaAs two-dimensional hole-gases are of particular interest.

8.4 Laboratory for Magnetotransport Characterization of Samples

An essential part in the development of semiconductor heterostructures is the characterization of samples with respect to impurities, interface smoothness etc. In this laboratory the characteristic quantities, mobility and electron density of the high-mobility two-dimensional electro gas samples are determined by means of magnetotransport measurements. The data obtained here is used as direct feedback for the MBE-laboratory and allows for the adjustment of growth parameters. The data is stored and indexed in a database such that all sample characteristics are easily accessible. We have assembled a measurement setup for the rapid determination of mobilities and densities at temperatures of 4.2 and 1.3 K. In addition, a 3He-cryostat has been installed in which samples can be investigated at magnetic fields up to 16 T and a base temperature of less then 300 mK. For the sample preparation another three workplaces are available. They provide means for making electric contacts, optically investigating sample surfaces, computer-controlled scribing and cleaving of the samples.

Chapter 9

Publications

M. Baur, S. Filipp, R. Bianchetti, J.M. Fink, M. Goeppl, L. Steffen, P.J. Leek, A. Blais, and A. Wallraff
Measurement of Autler-Townes and Mollow transitions in a strongly driven superconducting qubit
Physical Review Letters **102**, 243602 (2009)

A. Belousov, S. Katrych, J. Jun, J. Karpinski, B. Batlogg, D. Günther, J. Zhang, J. Zhang, and R. Sobolewski
Bulk single crystal growth of the ternary $Al_xGa_{1-x}N$ from solution in gallium under high pressure
Journal of Crystal Growth **311**, 3971 (2009)

K. Bernot, J. Luzon, A. Caneschi, D. Gatteschi, R. Sessoli, L. Bogani, A. Vindigni, A. Rettori, and M.G. Pini
Spin canting in a Dy-based single-chain magnet with dominant next-nearest-neighbor
Phys. Rev. B **79**, 134419 (2009)

R. Bianchetti, S. Filipp, M. Baur, J.M. Fink, M. Goeppl, P.J. Leek, L. Steffen, A. Blais, and A. Wallraff
Dynamics of dispersive single qubit read-out in circuit quantum electrodynamics
Physical Review A **80**, 043840 (2009)

Z. Bukowski, S. Weyeneth, R. Puzniak, P. Moll, S. Katrych, N.D. Zhigadlo, J. Karpinski, H. Keller, and B. Batlogg
Superconductivity at 23K and low anisotropy in Rb-substituted $BaFe_2As_2$ single crystals
Phys. Rev. B **79**, 104521 (2009)

S. Burkardt
Oxide and oxide-supported nanoclusters on quasicrystals
Logos Verlag, Berlin, ISBN 978-3-8325-2341-1

S. Burkardt, M. Erbudak
Oxygen-induced surface faceting of the threefold-symmetry surface of icosahedral AlPdMn quasicrystal
Surface Science **603**, 2248 (2009)

S. Burkardt, M. Erbudak, and R. Mäder
High-temperature surface oxidation of the decagonal AlCoNi quasicrystal
Surface Science **603**, 866 (2009)

M. Calamiotou, A. Gantis, E. Siranidi, D. Lampakis, J. Karpinski, and E. Liarokapis
Pressure-induced lattice instabilities and superconductivity in $YBa_2Cu_4O_8$ and optimally doped $YBa_2Cu_3O_7$
Phys. Rev. B **80**, 214517 (2009)

J. Chang, N. B. Christensen, Ch. Niedermayer, K. Lefmann, H.M. Rønnow, D.F. McMorrow, A. Schneidewind, P. Link, A. Hiess, M. Boehm, R. Mottl, S. Pailhés, N. Momono, M. Oda, M. Ido, and J. Mesot
Magnetic-Field-Induced Soft-Mode Quantum Phase Transition in the High-Temperature Superconductor $La_{1.855}Sr_{0.145}CuO_4$: An Inelastic Neutron-Scattering Study
Phys. Rev. Lett. **102**, 177006 (2009)

T. Choi, I. Shorubalko, S. Gustavsson, S. Schön, and K. Ensslin
Correlated counting of single electrons in a nanowire double quantum dot
N. J. Phys. **11**, 013005 (2009)

F. Cinti, O. Portmann, D. Pescia, and A. Vindigni
One-dimensional Ising ferromagnet frustrated by long-range interactions at finite temperatures
Phys. Rev. B **79**, 214434 (2009)

M. Ciorga, A. Einwanger, U. Wurstbauer, D. Schuh, W. Wegscheider, and D. Weiss
Electrical Spin Injection and Detection in Lateral All-semiconductor Devices
Phys. Rev. B **79**, 165321 (2009)

T. Claesson, M. Månsson, A. Önsten, M. Shi, Y. Sassa, S. Pailhés, J. Chang, A. Bendounan, L. Patthey, J. Mesot, T. Muro, T. Matsushita, T. Kinoshita, T. Nakamura, N. Momono, M. Oda, M. Ido, and O. Tjernberg
Electronic structure of La1.48Nd0.4Sr0.12CuO4 probed by high- and low-energy angle-resolved photoelectron spectroscopy
Phys. Rev. B **80**, 094503 (2009)

R. Cywinski, A.E. Bungau, M.W. Poole, S. Smith, P.D. de Reotier, R. Barlow, R. Edgecock, P.J.C. King, J.S. Lord, F. Pratt, K.N. Clausen, and T. Shiroka
Towards a dedicated high-intensity muon facility
Physica B **404**, 1024 (2009)

D. Daghero, M. Tortello, R.S. Gonnelli, V.A. Stepanov, N.D. Zhigadlo, and J. Karpinski
Evidence for two-gap nodeless superconductivity in SmFeAsO$_{1-x}$F$_x$ from point-contact Andreev-reflection spectroscopy
Phys. Rev. B **80**, 060502 (2009)

D. Daghero, M. Tortello, R.S. Gonnelli, V.A. Stepanov, N.D. Zhigadlo, and J. Karpinski
Possible multigap superconductivity in SmFeAsO$_{0.8}$F$_{0.2}$: A point-contact Andreev-reflection spectroscopy study
J. Supercond. Nov. Magn. **543**, 22 (2009)

A. Einwanger, M. Ciorga, U. Wurstbauer, D. Schuh, W. Wegscheider, and D. Weiss
Tunneling Anisotropic Spin Polarization in Lateral (Ga,Mn)As/GaAs Spin Esaki Diode Devices
App. Phys. Lett. **95**, 152101 (2009)

M. Erbudak, M. Mungan, and S. Burkardt
Nanoepitaxy on quasicrystal surfaces
Applied Surface Science **256**, 1284 (2009)

S. Filipp, P. Maurer, P.J. Leek, M. Baur, R. Bianchetti, J.M. Fink, M. Goeppl, L. Steffen, J.M. Gambetta, A. Blais, and A. Wallraff
Two-Qubit State Tomography using a Joint Dispersive Read-Out
Physical Review Letters **102**, 200402 (2009)

J.M. Fink, R. Bianchetti, M. Baur, M. Goeppl, L. Steffen, S. Filipp, P.J. Leek, A. Blais, and A. Wallraff
Dressed Collective Qubit States and the Tavis-Cummings Model in Circuit QED
Physical Review Letters **103**, 083601 (2009)

J.M. Fink, M. Baur, R. Bianchetti, S. Filipp, M. Goeppl, P.J. Leek, L. Steffen, A. Blais and A. Wallraff
Thermal Excitation of Multi-Photon Dressed States in Circuit Quantum Electrodynamics
submitted to Physica Scripta T137 (2009), (arXiv:0911.3797)

S.M. Frolov, A. Venkatesan, W. Yu, J.A. Folk, and W. Wegscheider
Electrical Generation of Pure Spin currents in a Two-Dimensional Electron Gas
Phys. Rev. Lett. **102**, 116802 (2009)

S.M. Frolov, S. Lüscher, W. Yu, Y. Ren, J.A. Folk, and W. Wegscheider
Ballistic spin resonance
Nature **458**, 868 (2009)

M. Fuechsle, J. Bentner, D.A. Ryndyk, M. Reinwald, W. Wegscheider, and C. Strunk
Effect of Microwaves on the Current-Phase Relation of Superconductor-Normal-Metal-Superconductor Josephson Junctions
Phys. Rev. Lett. **102**, 1217001 (2009)

A. Furrer, J. Mesot, and Th. Strässle
Neutron Scattering in Condensed Matter
Series on Neutron Techniques and Applications - Vol. **4**, 301 pages, World Scientific (2009)

U. Gasser, S. Gustavsson, B. Küng, K. Ensslin, T. Ihn, D.C. Driscoll, and A.C. Gossard
Statistical electron excitation in a double quantum dot induced by two independent quantum point contacts
Phys. Rev. B **79**, 035303 (2009)

R.S. Gonnelli, D. Daghero, M. Tortello, G.A. Ummarino, V.A. Stepanov, R.K. Kremer, J.S. Kim, N.D. Zhigadlo, and J. Karpinski
Point-contact Andreev-reflection spectroscopy in ReFeAsO$_{1-x}$F$_x$ (Re = La, Sm): Possible evidence for two nodeless gaps
Physica C **469**, 512 (2009)

M. Griesbeck, M.M. Glazov, T. Korn, E. Ya. Sherman, D. Waller, C. Reichl, D. Schuh, and W. Wegscheider
Cyclotron Effect on Coherent Spin Precession of Two-dimensional Electrons
Phys. Rev. B **80**, 241314 (2009)

S. Gustavsson, R. Leturcq, T. Ihn, K. Ensslin, and A. C. Gossard
Electrons in quantum dots: One by one
J. Appl. Phys. **105**, 122401 (2009)

S. Gustavsson, R. Leturcq, M. Studer, I. Shorubalko, T. Ihn, K. Ensslin, D.C. Driscoll, and A.C. Gossard
Electron counting in quantum dots
Surface Science Reports **64**, 191 (2009)

J. Güttinger, C. Stampfer, T. Frey, T. Ihn and K. Ensslin
Graphene quantum dots in perpendicular magnetic fields
Phys. Status Solidi **246**, 2553 (2009)

J. Güttinger, C. Stampfer, F. Libisch, T. Frey, J. Burgdoerfer, T. Ihn, and K. Ensslin
Electron-Hole Crossover in Graphene Quantum Dots
Phys. Rev. Lett. **103**, 046810 (2009)

D. Haug, V. Hinkov, A. Suchaneck, D.S. Inosov, N.B. Christensen, Ch. Niedermayer, P. Bourges, Y. Sidis, J.T. Park, A. Ivanov, C.T. Lin, J. Mesot, and B. Keimer
Magnetic-Field-Enhanced Incommensurate Magnetic Order in the Underdoped High-Temperature Superconductor $YBa_2Cu_3O_{6.45}$
Phys. Rev. Lett. **103**, 017001 (2009)

F. Hoffmann, G. Woltersdorf, W. Wegscheider, A. Einwanger, D. Weiss, and C.H. Back
Mapping the Magnetic Anisotropy in (Ga,Mn)As Nanostructures
Phys. Rev. B **80**, 054417 (2009)

T. Hong, R. Custelcean, B.C. Sales, B. Roessli, D.K. Singh, and A. Zheludev
A novel metal-organic compound with Heisenberg antiferromagnetic S=1/2 chains
Phys. Rev. B **80**, 132404 (2009)

M. Huefner, F. Molitor, A. Jacobsen, A. Pioda, C. Stampfer, K. Ensslin, and T. Ihn
Investigation of the Aharonov Bohm effect in a gated graphene ring
Phys. Status Solidi **246**, 2756 (2009)

M. Huefner, C. May, S. Kièin, K. Ensslin, T. Ihn, M. Hilke, K. Suter, and N.F. de Rooij
Scanning gate microscopy measurements on a superconducting single-electron transistor
Phys. Rev. B **79**, 134530 (2009)

T. Ihn, S. Gustavsson, U. Gasser, B. Küng, T. Müller, R. Schleser, M. Sigrist, I. Shorubalko, R. Leturcq, and K. Ensslin
Quantum dots investigated with charge detection techniques
Solid St. Comm. **149**, 1419 (2009)

W. Jiang, A. Wirthmann, Y.S. Gui, X.Z. Zhou, M. Reinwald, W. Wegscheider, C.-M. Hu, and G. Williams
Critical Behavior from the Anomalous Hall Effect in (GaMn)As
Phys. Rev. B **80**, 214409 (2009)

Y.J. Jo, J. Jaroszynski, A. Yamamoto, A. Gurevich, S.C. Riggs, G.S. Boebinger, D. Larbalestier, H.H. Wen, N.D. Zhigadlo, S. Katrych, Z. Bukowski, J. Karpinski, R.H. Liu, H. Chen, X.H. Chen, and L. Balicas
High-field phase-diagram of Fe arsenide superconductors
Physica C **469**, 566 (2009)

W.L. Kalb, A.F. Stassen, B. Batlogg, U. Berens, B. Schmidhalter, F. Bienewald, A. Hafner, and T. Wagner
Quinoid heteropentacenes as promising organic semiconductors for field-effect transistor applications
Journal of Applied Physics **105**, 043705 (2009)

J. Karpinski, N.D. Zhigadlo, S. Katrych, Z. Bukowski, P. Moll, S. Weyeneth, H. Keller,3R. Puzniak, M. Tortello, D. Daghero, R. Gonnelli, I. Maggio-Aprile, Y. Fasano, Ø. Fischer, and B. Batlogg
Single crystals of LnFeAsO1-xFx (Ln=La, Pr, Nd, Sm, Gd) and Ba1-xRbxFe2As2: growth, structure and superconducting properties
Physica C **469**, 370 (2009)

S. Katrych, Q.F. Gu, Z. Bukowski, N.D. Zhigadlo, G. Krauss, and J. Karpinski
A new triclinic modification of the pyrochlore-type KOs_2O_6 superconductor
J. Solid State Chem. **182**, 428 (2009)

S. Katrych, W. Steurer
Stability range of the ternary W-phase in the system Al-Co-Ni
Journal of Alloys and Compounds **481**, 258 (2009)

T. Kirk, L.G. DePietro, D. Pescia, and U. Ramsperger
Electron beam confinement and image contrast enhancement in near field emission scanning electron microscopy
Ultramicroscopy **109**, 463 (2009)

T. Kirk, O. Scholder, L.G. De Pietro, U. Ramsperger, and D. Pescia
Evidence of nonplanar field emission via secondary electron detection in near field emission scanning electron microscopy
Appl. Phys. Lett. **94**, 153502 (2009)

T. Kirk, U. Ramsperger, and D. Pescia
Near field emission scanning electron microscopy
J. Vac. Sci. Technol. B **27**, 152 (2009)

T. Kirk, L. De Pietro, U. Ramsperger, and D. Pescia
Near Field Emission SEM
Imaging and Microscopy **1**, 35 (2009)

T. Kondo, R. Khasanov, Y. Sassa, A. Bendounan, S. Pailhes, J. Chang, J. Mesot, H. Keller, N.D. Zhigadlo, M. Shi, Z. Bukowski, J. Karpinski, and A. Kaminski
Anomalous Asymmetry in the Fermi Surface of the High-Temperature Superconductor $\mathrm{YBa_2Cu_4O_8}$ Revealed by Angle-Resolved Photoemission Spectroscopy
Phys. Rev. B **80**, 100505R (2009)

T. Korn, D. Stich, R. Schulz, D. Schuh, W. Wegscheider, and C. Schuller
Spin Dynamics in High-mobility Two-dimensional Electron Systems
Advances in Solid State Physics **48**, 143 (2009)

M. Kugler, T. Andlauer, T. Korn, A. Wagner, S. Fehringer, R. Schulz, M. Kubova, C. Gerl, D. Schuh, W. Wegscheider, P. Vogl, and C. Schuller
Gate Control of Low-temperature Spin Dynamics in Two-dimensional Hole Systems
Phys. Rev. B **80**, 035325 (2009)

B. Küng, S. Gustavsson, T. Choi, I. Shorubalko, T. Ihn, S. Schön, F. Hassler, G. Blatter, and K. Ensslin
Noise-Induced Spectral Shift Measured in a Double Quantum Dot
Phys. Rev. B **80**, 115315 (2009)

B. Küng, O. Pfä?i, S. Gustavsson, T. Ihn, K. Ensslin, M. Reinwald, and W. Wegscheider
Time-resolved Charge Detection with Cross-Correlation Techniques
Phys. Rev. B **79**, 035314 (2009)

C. Latta, A. Högele, Y. Zhao, A.N. Vamivakas, P. Maletinsky, M. Kroner, J. Dreiser, I. Carusotto, A. Badolato, D. Schuh, W. Wegscheider, M. Atature, and A. Imamoglu
Confluence of Resonant Laser Excitation and Bidirectional Quantum-dot Nuclear-spin Polarization
Nature Physics **5**, 758 (2009)

M. Lavagnini, A. Sacchetti, C. Marini, M. Valentini, R. Sopracase, A. Perucchi, P. Postorino, S. Lupi, J.-H. Chu, I.R. Fisher, and L. Degiorgi
Pressure dependence of the single particle excitation in the charge-density-wave $\mathrm{CeTe_3}$ system
Phys. Rev. B **79**, 075117 (2009)

V. Lechner, L.E. Golub, P. Olbrich, S. Stachel, D. Schuh, W. Wegscheider, V.V. Bel'kov, and S.D. Ganichev
Tuning of Structure Inversion Asymmetry by the Delta-doping Position in (001)-grown GaAs Quantum Wells
App. Phys. Lett. **94**, 242109 (2009)

P.J. Leek, S. Filipp, P. Maurer, M. Baur, R. Bianchetti, J.M. Fink, M. Goeppl, L. Steffen, and A. Wallraff
Using Sideband Transitions for Two-Qubit Operations in Superconducting Circuits
Physical Review B **79**, 180511(R) (2009)

M. Le Tacon, T.R. Forrest, Ch. Rüegg, A. Bosak, A.C. Walters, R. Mittal, H.M. Rønnow, N.D. Zhigadlo, S. Katrych, J. Karpinski, J.P. Hill, M. Krisch, and D.F. McMorrow
Inelastic x-ray scattering study of superconducting $\mathrm{SmFeAsO}_{1-x}\mathrm{F}_y$ single crystals: Evidence for strong momentum-dependent doping-induced renormalizations of optical phonons
Phys Rev B **80**, 220504(R) (2009)

R. Leturcq, C. Stampfer, K. Inderbitzin, L. Durrer, C. Hierold, E Mariani, M. G. Schultz, F. von Oppen, and K. Ensslin
Franck-Condon blockade in suspended carbon nanotube quantum dots
Nature Physics **5**, 327 (2009)

S. Lizzit, A. Baraldi, Ch. Grütter, J.H. Bilgram, and Ph. Hofmann
The surface phase transition and low-temperature phase of a-Ga(010) studied by SPA-LEED
Surface Science **603**, 3222 (2009)

J.-N. Longchamp, S. Burkardt, M. Erbudak, and Y. Weisskopf
Erratum: Formation of a well-ordered ultrathin aluminum-oxide film on icosahedral AlPdMn quasicrystal
Phys. Rev. B **80**, 149901(E) (2009)

L. Malone, J.D. Fletcher, A. Serafin, A. Carrington, N.D. Zhigadlo, S. Katrych, Z. Bukowski, and J. Karpinski
Magnetic penetration depth of single crystal $\mathrm{SmFeAsO_{0.8}F_{0.2}}$: a fully gapped superconducting state
Phys. Rev. B **79**, 140501(R) (2009)

T. Masuda, K. Kakurai, and A. Zheludev
Spin dimers in the quantum ferrimagnet $\mathrm{Cu_2Fe_2Ge_4O_{13}}$ under staggered and random magnetic fields
Phys. Rev. B **80**, 180412 (2009)

M. Matusiak, T. Plackowski, Z. Bukowski, N.D. Zhigadlo, and J. Karpinski
Thermoelectric Power as an Evidence of the Spin Density Wave Order in the SmFeAsO and NdFeAsO
Phys. Rev. B **79**, 212502 (2009)

M. Matusiak, T. Plackowski, Z. Bukowski, N.D. Zhigadlo, and J. Karpinski
Evidence of spin-density-wave order in $\mathrm{RFeAsO}_{1-x}\mathrm{F}_x$ from measurements of thermoelectric power
Phys. Rev. B **79**, 212502 (2009)

T. Mertelj, V.V. Kabanov, C.Gadermaier, J.Karpinski, and D. Mihailovic
Distinct pseudogap and superconducting state quasiparticle relaxationdynamics in nearly-optimally doped $\mathrm{SmFeAsO}_{0.8}\mathrm{F}_{0.2}$ single crystals
Phys. Rev. Lett. **102**, 117002 (2009)

T. Mertelj, V.V. Kabanov, C. Gadermaier, N.D. Zhigadlo, S. Katrych, Z. Bukowski, J. Karpinski, and D. Mihailovic
Photoinduced quasiparticle relaxation dynamics in near-optimally doped $\mathrm{SmFeAsO}_{0.8}\mathrm{F}_{0.2}$ single crystals
J. Supercond. Nov. Magn. **22**, 575 (2009)

F. Molitor, S. Dröscher, J. Güttinger, A. Jacobsen, C. Stampfer, T. Ihn, and K. Ensslin
Transport through graphene double dots
Appl. Phys. Lett. **94**, 222107 (2009)

F. Molitor, A. Jacobsen, C. Stampfer, J. Güttinger, T. Ihn, and K. Ensslin
Transport gap in side-gated graphene constrictions
Phys. Rev. B **79**, 075426 (2009)

V. Moshchalkov, M. Menghini, T. Nishio, Q.H. Chen, A.V. Silhanek, V.H. Dao, L.F. Chibotaru, N.D. Zhigadlo, and J. Karpinski
Type-1.5 Superconductivity
Phys. Rev. Lett. **102**, 117001 (2009)

D. Neumaier, M. Turek, U. Wurstbauer, A. Vogl, M. Utz, W. Wegscheider, and D. Weiss
All-Electrical Measurement of the Density of States in (Ga,Mn)As
Phys. Rev. Lett. **103**, 087203 (2009)

M. Oestreich, M. Romer, G. Muller, D. Schuh, W. Wegscheider, and J. Hubner
Spin Noise Spectroscopy in Semiconductors
Proc. SPIE **7398**, 739802 (2009)

P. Olbrich, J. Allerdings, V.V. Bel'kov., S.A. Tarasenko, D. Schuh, W. Wegscheider, T. Korn, C. Schuller, D. Weiss, and S.D. Ganichev
Magnetogyrotropic Photocalvanic Effect and Spin Dephasing in (110)-grown $\mathrm{GaAs/Al}_x\mathrm{Ga}_{1-x}\mathrm{As}$ Quantum Well Structures
Phys. Rev. B **79**, 245329 (2009)

P. Olbrich, E.L. Ivchenko, R. Ravash, T. Feil, S.D. Danilov, J. Allerdings, D. Weiss, D. Schuh, W. Wegscheider, and S.D. Ganichev
Ratchet Effects Induced by Terahertz Radiation in Heterostructures with a Lateral Periodic Potential
Phys. Rev. Lett. **103**, 090603 (2009)

G. Panaccione, I. Vobornik, J. Fujii, D. Krizmancic, E. Annese, L. Giovanelli, F. Maccherozzi, F. Salvador, A. De Luisa, D. Benedetti, A. Gruden, P. Bertoch, F. Polack, D. Cocco, G. Sostero, B. Diviacco, M. Hochstrasser, U. Maier, D. Pescia, C.H. Back, T. Greber, J. Osterwalder, M. Galaktionov, M. Sancrotti, and G. Rossi
Advanced photoelectric effect experiment beamline at Elettra: A surface science laboratory coupled with Synchrotron radiation
Rev. Sci. Instruments **80**, 043105 (2009)

P. Parisiades, E. Liarokapis, N.D. Zhigadlo, S. Katrych, and J. Karpinski
Raman invesigations of C-, Li- and Mn-doped MgB_2
J. Supercond. Nov. Magn. **22**, 169 (2009)

F. Pfuner, J.G. Analytis, J.-H. Chu, I.R. Fisher, and L. Degiorgi
Charge dynamics of the spin-density-wave state in $\mathrm{BaFe}_2\mathrm{As}_2$
Eur. Phys. J. B **67**, 513 (2009)

F. Pfuner, L. Degiorgi, J.-H. Chu, N. Ru, K.Y. Shin, and I.R. Fisher
Optical properties of the charge-density-wave rare-earth tri-telluride compounds: a view on PrTe_3
Physica B **404**, 533 (2009)

A. Pfund, I. Shorubalko, K. Ensslin, and R. Leturcq
Dynamics of coupled spins in quantum dots with strong spin-orbit interaction
Phys. Rev. B **79**, 121306R (2009)

F. Pfuner, L. Degiorgi, H. Berger, and L. Forro
Infrared investigation of the phonon spectrum in the frustrated spin cluster compound $\mathrm{FeTe}_2\mathrm{O}_5\mathrm{Cl}$
J. Phys.: Condens. Matter **21**, 375401 (2009)

F. Pfuner, L. Degiorgi, T.I. Baturina, V.M. Vinokur, and M.R. Baklanov
Optical properties of TiN thin films close to the superconductor-insulator transition
New J. Phys. **11**, 113017 (2009)

O. Portmann, A. Vindigni, and D. Pescia
Scaling in modulated systems
Complex Sciences **4**, 865 (2009)

K. Prsa, H.M. Rønnow, O. Zaharko, N.B. Christensen, J. Jensen, J. Chang, S. Streule, M. Jiménez-Ruiz, H. Berger, M. Prester, and J. Mesot
Anomalous Magnetic Excitations of Cooperative Tetrahedral Spin Clusters
Phys. Rev. Lett. **102**, 177202 (2009)

V. Puller, Y. Meir, M. Sigrist, K. Ensslin, and T. Ihn
Breaking of Phase Symmetry in Non-Equilibrium Aharonov-Bohm Oscillations through a Quantum Dot
Phys. Rev. B **80**, 035416 (2009)

N. Quack, P. Rüst, S. Blunier, J. Dual, F. Felder, M. Rahim, M.Fill, M. Arnold, and H. Zogg
A Comb Drive Actuated Vertically Moving Micromirror for Mid-Infrared Resonant Cavity Enhanced Detectors
Sensors 2008 **8**, 5466 (2008)

K. Rachor, T.E. Raab, D. Heitmann, C. Gerl, and W. Wegscheider
Cyclotron Resonance of Carbon-doped Two-dimensional Hole systems: From the Magnetic Quantum Limit to Low Magnetic Fields
Phys. Rev. B **79**, 125417 (2009)

M. Rahim, A. Khiar, F. Felder, M. Fill, and H. Zogg
4.5 μm wavelength vertical external cavity surface emitting laser operating above room temperature
Appl. Phys. Lett. **94**, 201112 (2009)

M. Rahim, M. Fill, F.Felder, D. Chappuis,M. Corda, and H. Zogg
Mid-infrared PbTe vertical external cavity surface emitting laser on Si-substrate with above 1 W output power
Appl. Phys. Lett. **95**, 241107 (2009)

A. Rudolph, M. Soda, M. Kiessling, T. Wojtowicz, D. Schuh, W. Wegscheider, J. Zweck, C. Back, and E. Reiger
Ferromagnetic GaAs/GaMnAs Core-Shell Nanowires Grown by Molecular Beam Epitaxy
Nano Letters **9**, 3860 (2009)

A. Sacchetti, C.L. Condron, S.N. Gvasaliya, F. Pfuner, M. Lavagnini, M. Baldini, M.F. Toney, M. Merlini, M. Hanfland, J. Mesot, J.-H. Chu, I. R. Fisher, P. Postorino, and L. Degiorgi
Pressure-induced quenching of the charge-density-wave state in rare-earth tritellurides observed by x-ray diffraction
Phys. Rev. B **79**, 201101(R) (2009)

S. Sanna, R. De Renzi, G. Lamura, C. Ferdeghini, A. Palenzona, M. Putti, M. Tropeano, T. Shiroka
Magnetic-superconducting phase boundary of SmFeAsO$_{1-x}$F$_x$ studied via muon spin rotation: Unified behavior in a pnictide family
Phys. Rev. B **80**, 052503 (2009)

S. Sanna, R. De Renzi, G. Lamura, C. Ferdeghini, A. Martinelli, A. Palenzona, M. Putti, M. Tropeano, and T. Shiroka
Intrinsic Ferromagnetic Impurity Phases in SmFeAsO$_{1-x}$F$_x$ Detected by μSR
J. Supercond. Nov. Magn. **22**, 585 (2009)

A. Schilling, R Dell'Amore, J. Karpinski, M. Medarde, K. Conder, and K. Pomjakushina
LaBaNiO$_4$: a Fermi glass
J.Phys.:Condens. Matter **21**, 015701 (2009)

G. Schiltz
Studieren mit digitalen Medien - ein Status Quo
E-Learning Dossier (2009)

G.J. Schinner, H.P. Tranitz, W. Wegscheider, J.P. Kotthaus, and S. Ludwig Phonon-Mediated Nonequilibrium Interaction between Nanoscale Devices
Phys. Rev. Lett. **102**, 186801 (2009)

J. Schlappa, T. Schmitt, F. Vernay, V.N. Strocov, V. Ilakovac, B. Thielemann, H.M. Rønnow, S. Vanishri, A. Piazzalunga, X. Wang, L. Braicovich, G. Ghiringhelli, C. Marin, J. Mesot, B. Delley, and L. Patthey
Collective Magnetic Excitations in the Spin Ladder Sr$_{14}$Cu$_{24}$O$_{41}$ Measured Using High-Resolution Resonant Inelastic X-Ray Scattering
Phys. Rev. Lett. **103**, 047401 (2009)

M. Schlapps, T. Lermer, S. Geissler, D. Neumaier, J. Sadowski, D. Schuh, W. Wegscheider, and D. Weiss
Transport Through (Ga,Mn)As Nanoislands: Coulomb Blockade and Temperature Dependence of the Conductance
Phys. Rev. B **80**, 125330 (2009)

S. Schnez, F. Molitor, C. Stampfer, J. Guettinger, I. Shorubalko, T. Ihn, and K. Ensslin
Observation of excited states in a graphene quantum dot
Appl. Phys. Lett. **94**, 012107 (2009)

S. Schöder, H. Reichert, H. Schröder, M. Mezger, J. Okasinski, V. Honkimäki, J. Bilgram, and H. Dosch
Radiation-induced interface melting of ice
Phys. Rev. Lett. **103**, 095502 (2009)

K. Sedlak, T. Shiroka, A. Stoykov, and R. Scheuermann
GEANT4 simulation of the upgraded ALC spectrometer
Physica B **404**, 974 (2009)

T. Shiroka, S.P. Cottrell, P.J.C. King, and N.J. Rhodes
Scintillating fibres for future μSR spectrometers
Physica B **404**, 982 (2009)

T. Shiroka, T. Prokscha, E. Morenzoni, and K. Sedlak
GEANT4 as a simulation framework in μSR
Physica B **404**, 966 (2009)

A. Siddiki, J. Horas, J. Moser, W. Wegscheider, and S. Ludwig
Interaction Mediated Asymmetries of the Quantized Hall Effect
Eur. Phys. Lett. **88**, 17007 (2009)

H.M. Singer, I. Singer, and J.H. Bilgram
Experimental observation and computer simulations of 3D triplet structures in diffusion limited growth of xenon crystals
Phys. Rev. Lett. **103**, 015501 (2009)

C. Stampfer, J. Guettinger, S. Hellmueller, F. Molitor, K. Ensslin, and T. Ihn
Energy gaps in etched graphene nanoribbons
Phys. Rev. Lett. **102**, 056403 (2009)

A. Stoykov, R. Scheuermann, K. Sedlak, T. Shiroka, and V. Zhuk
A new detector system for the ALC spectrometer: First experience with G-APDs in μSR instrumentation
Physica B **404**, 986 (2009)

M. Studer, G. Salis, K. Ensslin, D.C. Driscoll, and A.C. Gossard
Gate-controlled spin-orbit interaction in a parabolic GaAs/AlGaAs quantum well
Phys. Rev. Lett. **103**, 027201 (2009)

M. Studer, S. Schön, K. Ensslin, and G. Salis
Spin-orbit interaction and spin relaxation in a two-dimensional electron gas
Phys. Rev. B **79**, 045302 (2009)

B. Thielemann, Ch. Rüegg, K. Kiefer, H.M. Rønnow, B. Normand, P. Bouillot, C. Kollath, E. Orignac, R. Citro, T. Giamarchi, A.M. Läuchli, D. Biner, K.W. Krämer, F. Wolff-Fabris, V.S. Zapf, M. Jaime, J. Stahn, N.B. Christensen, B. Grenier, D.F. McMorrow, and J. Mesot
Field-controlled magnetic order in the quantum spin-ladder system (Hpip)$_2$CuBr$_4$
Phys. Rev. B **79**, 020408 (2009)

B. Thielemann, Ch. Rüegg, H.M. Rønnow, A.M. Läuchli, J.-S. Caux, B. Normand, D. Biner, K.W. Krämer, H.-U. Güdel, J. Stahn, K. Habicht, K. Kiefer, M. Boehm, D.F. McMorrow, and J. Mesot
Direct Observation of Magnon Fractionalization in the Quantum Spin Ladder
Phys. Rev. Lett. **102**, 107204 (2009)

L. Tielmann, Y. Yoon, W. Dietsche, K. Von Klitzing, and W. Wegscheider
Dominant Parameters for the Critical Tunneling Current in Bilayer Exciton Condensates
Phys. Rev. B **80**, 165120 (2009)

R. Troc, Z. Bukowski, J. Stepien-Damm, and C. Sulkowski
Anisotropy of Magnetic and Transport Properties of UAuSb$_2$ Single Crystals
Acta Phys. Polon. A **115**, 181 (2009)

A. Vindigni, M.G. Pini
Selection rules for single-chain-magnet behaviour in non-collinear Ising systems
J. Phys.: Condens. Matter **21**, 236007 (2009)

A. Vindigni, O. Portmann, N. Saratz, F. Cinti, P. Politi, and D. Pescia
Tempertaure-induced domain shrinking in Ising ferromagnets frustrated by a long-range interaction
Complex Sciences **4**, 783 (2009)

L.Ya. Vinnikov, T.M. Artemova, I.S. Veshchunov, N.D. Zhigadlo, J. Karpinski, P. Popovich, D.L. Sun, C.T. Lin, and A.V. Boris
Vortex Structure in Superconducting Iron Pnictide Single Crystals
JETP Letters **90**, 299 (2009)

X.P. Vögele, D. Schuh, W. Wegscheider, J.P. Kotthaus, and A.W. Holleitner
Density Enhanced Diffusion of Dipolar Excitons within a One-Dimensional Channel
Phys. Rev. Lett. **103**, 126402 (2009)

P. Wachter
Cu, Pu and Fe high Tc superconductors: spin holes in antiferromagnetic clusters form nonmagnetic bipolarons
Physica C **469**, 199 (2009)

M.P. Walser, W.L. Kalb, T. Mathis, T.J. Brenner, and B. Batlogg
Stable complementary inverters with organic field-effect transistors on Cytop fluoropolymer gate dielectric
Applied Physics Letters **94**, 053303 (2009)

M.P. Walser, W.L. Kalb, T. Mathis, and B. Batlogg
Low-voltage organic transistors and inverters with ultrathin fluoropolymer gate dielectric
Applied Physics Letters **95**, 233301 (2009)

S. Weyeneth, R. Puzniak, U. Mosele, S. Kohout, J. Roos, N.D. Zhigadlo, S. Katrych, Z. Bukowski, J. Karpinski, and H. Keller
Evidence for two distinct anisotropies in the oxypnictade superconductors $\mathrm{SmFeAsO_{0.8}F_{0.2}}$ and $\mathrm{NdFeAsO_{0.8}F_{0.2}}$
J. Supercond Nov Magn **22**, 347 (2009)

S. Weyeneth, R. Puzniak, U. Mosele, S. Kohout, J. Roos, N.D. Zhigadlo, S. Katrych, Z. Bukowski, J. Karpinski, and H. Keller
Anisotropy of superconducting single crystal $\mathrm{SmFeAsO_{0.8}F_{0.2}}$ studied by torque magnetometry
J. Supercond. Nov. Magn. **22**, 325 (2009)

J.S. White, V. Hinkov, R.W. Heslop, R.J. Lycett, E.M. Forgan, C. Bowell, S. Strässle, A.B. Abrahamsen, M. Laver, C.D. Dewhurst, J. Kohlbrecher, J.L. Gavilano, J. Mesot, B. Keimer, and A. Erb
Fermi Surface and Order Parameter Driven Vortex Lattice Structure Transitions in Detwinned $\mathrm{YBa_2Cu_3O_7}$
Phys. Rev. Lett. **102**, 097001 (2009)

M. Wimmer, M. Lobenhofer, J. Moser, A. Matos-Abiague, D. Schuh, W. Wegscheider, J. Fabian, K. Richter, and D. Weiss
Orbital Effects on Tunneling Anisotropic Magnetoresistance in Fe/GaAs/Au Junctions
Phys. Rev. B **80**, 121301 (2009)

U. Wurstbauer, W. Wegscheider
Magnetic Ordering Effects in a Mn-modulation-doped High Mobility Two-dimensional Hole System
Phys. Rev. B **79**, 155444 (2009)

U. Wurstbauer, M. Soda, R. Jakiela, D. Schuh, D. Weiss, J. Zweck, and W. Wegscheider
Coexistence of Ferromagnetism and Quantum Hall Effect in Mn modulation-doped Two-dimensional Hole Systems
J. Cryst. Growth **311**, 2160 (2009)

Y. Yamauchi, M. Hashisaka, S. Nakamura, K. Chida, S. Kasai, T. Ono, R. Leturcq, K. Ensslin, D.C. Driscoll, A.C. Gossard, and K. Kobayashi
Universality of bias- and temperature-induced dephasing in ballistic electronic interferometers
Phys. Rev. B **79**, 161306R (2009)

J. Zhang, A. Belousov, S. Katrych, J. Jun, J. Karpinski, B. Batlogg and R. Sobolewski
Femtosecond pump-probe characterization of high-pressure grown $\mathrm{Al}_x\mathrm{Ga}_{1-x}\mathrm{N}$ single crystals
Gallium Nitride Materials and Devices IV, Proc. of SPIE **7216**, 721623-1 (2009)

J. Zhang, A. Belousov, J. Karpinski and R. Sobolewski
Femtosecond pump-probe characterization of high-pressure grown $\mathrm{Al}_x\mathrm{Ga}_{1-x}\mathrm{N}$ single crystals
J.Phys.: Conf. Ser. **193**, 012058 (2009)

A. Zheludev, V.O. Garlea, A. Tsvelik, L.-P. Regnault, K. Habicht, K. Kiefer, and B. Roessli
Excitations from a chiral magnetized state of a frustrated quantum spin liquid
Phys. Rev. B **80**, 214413 (2009)

H. Zogg, M. Rahim, A. Khiar, M. Fill, F. Felder, N. Quack, S. Blunier, and J. Dual
IV-VI Mid-IR Tunable Lasers and Detectors with External Resonant Cavities
Proc. SPIE **7453**, 74530R, Infrared Spaceborne Remote Sensing and Instrumentation XVII, 2009

H. Zogg, M. Rahim, F. Felder, M. Fill, D. Boye, and A. Khiar
Leadchalcogenide VECSELs on Si and BaF2 for 5 um emission
Proc. SPIE **7193**, 71931G, Photonics West Solid State Lasers XVIII: Technology and Devices, San Jose, CA, USA, Jan. 2529, 2009

Chapter 10

Presentations

(⋆ = invited talk)

Acremann, Y.
Magnetization Dynamics on the Nanoscale
Frontiers in optics 2009, San Jose, USA, 12.10.2009

Acremann, Y.
Imaging spin current driven dynamics
MAXYMUS workshop, Berlin, Germany, 11.11.2009

Acremann, Y.
DC spin current driven vortex dynamics
3rd International Symposium on the Dynamics of Magnetic Vortices, Hamburg, Germany, 30.11.2009

Acremann, Y.
Magnetization dynamics: from spin injection to ultrafast switching
Probing magnetic dynamics with ultrashort coherent x-ray pulses, Triest, Italy, 18.12.2009

⋆ Batlogg, B.
Mit wie viel Technik ist unsere Gesellschaft zufrieden?
Lions Club, Feldkirch, Oesterreich, 09.01.2009

⋆ Batlogg, B.
Introduction to electron correlation
MaNEP Winter School ”Exploring New Phases of Electronic Matter”, Saas Fee, Switzerland, 11.01.2009

⋆ Batlogg, B.
Correlated electrons: transition metal compounds
MaNEP Winter School ”Exploring New Phases of Electronic Matter”, Saas Fee, Switzerland, 12.01.2009

⋆ Batlogg, B.
CMR Manganates, HTS cuprates and layered cobaltates as examples of electron correlation materials
MaNEP Winter School ”Exploring New Phases of Electronic Matter”, Saas Fee, Switzerland,12.01.2009

⋆ Batlogg, B.
Interface effects in organic field-effect devices
Int. Forum of Printed Active Displays, Seoul, Korea, 16.01.2009

⋆ Batlogg, B.
Electronic anisotropy and critical currents in Fe-As superconductors
Int. Workshop on Novel Materials and Superconductivity, Planneralm, Austria, 21.02.2009

⋆ Batlogg, B.
Fast spectroscopy for materials with strong electron correlation
PSI-XFEL Science Workshop, University of Zurich, Switzerland, 06.03.2009

⋆ Batlogg, B.
Physik und Eigenschaften organischer Transistoren
Fachtagung Elektronik der Zukunft, Winterthur, Switzerland, 02.07.2009

⋆ Batlogg, B.
Na_xCoO_2: switching between magnetic ground states
Int. Conference on Magnetism, Karlsruhe, Germany, 30.07.2009

⋆ Batlogg, B.
Interfaces and surfaces in organic molecular crystals: key to organic electronic devices
Joint Annual Meeting SPG-ÖPG-ÖGAA 2009, Innsbruck, Austria, 03.09.2009

⋆ Batlogg, B.
Wieviel Technik ist genug?
Erfahrungswoche Technik und Gesellschaft, Pädagogische Hochschule Wallis, Brig, Switzerland, 07.09.2009

⋆ Batlogg, B.
Critical currents and high magnetic field scales in SmFeAs(O,F) single crystals: promising for applications
New Developments in Strongly Correlated Electron Systems, Zurich, Switzerland, 21.09.2009

Baur, M.
Measurement of Autler-Townes and Mollow transitions in a strongly driven superconducting qubit
APS March Meeting, Pittsburgh, USA, 16.03.2009

Belousov, A.
High pressure growth of bulk single $\mathrm{Al}_x\mathrm{Ga}_{1-x}\mathrm{N}$ crystals
SPIE Photonics West, San Jose, CA, USA, 24.01.2009

⋆ Belousov, A.
High pressure growth of bulk single $\mathrm{Al}_x\mathrm{Ga}_{1-x}\mathrm{N}$ crystals
Seminar at University of Rochester, Laboratory for Laser Energetics, Rochester, USA, 12.03.2009

⋆ Belousov, A.
High pressure thermodynamics and crystal growth of $\mathrm{Al}_x\mathrm{Ga}_{1-x}\mathrm{N}$
IWBNS-VI, 6th Int. Workshop on Bulk Nitride Semiconductors, Galindia Mazurski Eden, Poland, 23.08.2009

⋆ Belousov, A.
Single crystals of $\mathrm{Al}_x\mathrm{Ga}_{1-x}\mathrm{N}$: high pressure growth and properties
IWBNS-VI, 6th Int. Workshop on Bulk Nitride Semiconductors, Galindia Mazurski Eden, Poland, 24.08.2009

Bianchetti, R.
Dynamics of dispersive single qubit read-out in circuit quantum electrodynamics
APS March Meeting, Pittsburgh, USA, 16.03.2009

Bianchetti, R. (Poster)
Dynamics of dispersive single qubit read-out in circuit quantum electrodynamics
Quantum Measurement and Metrology with Solid State Devices, Physikzentrum Bad Honnef, Bonn, Germany, 01.11.2009

Bukowski, Z. (Poster)
Superconductivity in $\mathrm{RbFe_2As_2}$ and $\mathrm{Ba}_{1-x}\mathrm{Rb}_x\mathrm{Fe_2As_2}$
9th Int. Conference on Materials and Mechanisms of Superconductivity (M2S-IX), Tokyo, Japan, 08.09.2009

Burkardt, S.
High-temperature surface oxidation of the decagonal AlCoNi
SAOG Annual Meeting, Fribourg, France, 23.1.2009

Burkardt, S.
Novel substrates of nanometer size Al-oxide layers grown on AlCoNi and AlPdMn quasicrystals
ECASIA ’09, TR-Antalya, 18.10.2009

Choi, T.
Self-aligned charge read-out for InAs nanowire quantum dots
Quantum Systems and Technology (QSIT) Meeting 2009, Arosa, Switzerland, 21.01.2009

Choi, T.
Time-resolved Single-Electron Detection in InAs Nanowire Quantum Dots
QSIT junior meeting, Passugg, Switzerland, 02.06.2009

Choi, T.
Time-resolved Single-Electron Detection in InAs Nanowire Quantum Dots
International Conference on Noise and Fluctuations, Pisa, Italy, 15.6.2009

Choi, T.
Time-resolved single-electron detection in semiconductor nanostructures
Joint Annual Meeting of SPS, ÖPG and ÖGAA, Innsbruck, Austria, 4.9.2009

Csontos, M.
0.7 feature in p-type quantum point contacts tuned by combined in-plane and top gates
Spintech, Krakau

⋆ Degiorgi, L.
Charge dynamics of the spin-density-wave state in $BaFe_2As_2$
Internal MaNEP Workshop 2009, Neuchatel, Switzerland, 20.01.2009

⋆ Degiorgi, L.
Spectroscopic investigations of two-dimensional charge-density-wave systems
Conference on Study of Matter at Extreme Conditions (SMEC), Miami, USA, 28.03.2009

⋆ Degiorgi, L.
Infrared and Raman study of the charge-density-wave ground state
Solid State Physics Seminar at the National Laboratory INFN in Frascati, Frascati, Italy, 20.04.2009

⋆ Degiorgi, L.
Charge dynamics of the spin-density-wave state in $BaFe_2As_2$
Summer School on Correlated Behavior and Quantum Criticality in Heavy Fermion and Related Systems, Aspen Center for Physics, USA,31.08.2009

Degiorgi, L.
Evidence for coupling between charge-density-wave and phonons in two-dimensional rare-earth tri-tellurides
March Meeting of the American Physical Society, Pittsburgh, USA, 16.03.2009

Degiorgi, L.
Pressure dependence of the single particle excitation in the charge- density-wave $CeTe_3$ system
March Meeting of the American Physical Society, Pittsburgh, USA, 17.03.2009

Degiorgi, L.
Charge dynamics of the spin-density-wave state in $BaFe_2As_2$
March Meeting of the American Physical Society, Pittsburgh, USA, 18.03.2009

Dröscher, S.
Local Oxidation of Graphene
Graphene Meeting, Obergurgl, Austria, 02.03.2009

⋆ Ensslin, K.
Electrons in quantum dots - one by one
Physics colloquium, Yale University, USA, 09.02.2009

⋆ Ensslin, K.
Quantum dots: from semiconductors to graphene
Condensed Matter Seminar, Columbia University, USA, 10.02.2009

⋆ Ensslin, K.
Graphene quantum dots
Solid State and Optics seminar, Yale University, USA, 11.02.2009

⋆ Ensslin, K.
Electrons in quantum dots - one by one
Physics Colloquium, Univ. of Freiburg, Germany, 27.04.2009

⋆ Ensslin, K.
Time-resolved electron transport through quantum dots
Seminar, Max-Planck-Institut für Festkörperforschung, Stuttgart, Germany, 13.05.2009

⋆ Ensslin, K.
Electrons in quantum dots - one by one
Dean of Natural Science Podium, Ben Gurion University, Israel, 02.06.2009

⋆ Ensslin, K.
Graphene quantum dots
Seminar, University of British Columbia, Vancouver, Canada, 03.07.2009

⋆ Ensslin, K.
Graphene quantum circuits
Seminar, Harvard University, Boston, USA, 30.07.2009

⋆ Ensslin, K.
0.7 feature in p-type quantum point contacts
Seminar, Harvard University, Boston, USA, 06.08.2009

⋆ Ensslin, K.
Quantum dots: from semiconductors to graphene
Condensed Matter Seminar, MIT, Boston, USA, 10.08.2009

⋆ Ensslin, K.
Graphene quantum circuits
Seminar, Physics Department, Stanford University, USA, 04.12.2009

⋆ Ensslin, K.
Quantum physics in quantum dots
Winter school of NCCR MANEP, Saas-Fee, Switzerland, 12.01.2009

⋆ Ensslin, K.
Graphene quantum dots
Workshop on ”Trends in Nanoscience”, Kloster Irsee, Germany, 28.02.2009

⋆ Ensslin, K.
Graphene constrictions and quantum dots
ESF Research Conference, ”Graphene week”, Obergurgl, Austria, 02.03.2009

⋆ Ensslin, K.
Correlated electron transport through quantum dots
Meeting of the German Physical Society (DPG), Dresden, Germany, 23.03.2009

⋆ Ensslin, K.
Graphene quantum dots
Meeting of the EU network CARDEQ, Dresden, Germany, 24.03.2009

⋆ Ensslin, K.
Time-resolved electron transport through quantum dots
WE-Heraeus-Seminar on ”Noise and Full Counting Statistics in Mesoscopic Transport”, Bad Honnef, Germany, 18.05.2009

⋆ Ensslin, K.
Single charge detection and back action in quantum circuits
Conference on ”Perspectives of Mesoscopic Physics” on the occasion of the 70th Birthday of Professor Joe Imry, Weizmann Institute, Israel, 31.05.2009

⋆ Ensslin, K.
Correlated charge detection and backaction in quantum dots
Advanced Research Workshop ”Meso-09”, Landau Institute for Theoretical Physics, Chernogolovka, Russia, 11.06.2009

⋆ Ensslin, K.
Graphene quantum circuits
International Workshop on Recent Progress in Graphene Research, Korea Institute for Advanced Study, Seoul, Korea, 29.06.2009

⋆ Ensslin, K.
Time-resolved electron transport through nanostructures
Research Workshop ”Quantum transport in electronic nanosystems”, Karlsruhe, Germany, 20.09.2009

⋆ Ensslin, K.
Electronic properties of nanostructures
Perspectives in Nanoscience and Nanotechnology - NANO2009, San Sebastian, Spain, 28.09.2009

⋆ Ensslin, K.
Phase coherent electrons in rings
Plenary talk, International conference 50 years after the discovery of the Aharonov-Bohm effect, Tel Aviv, Israel, 11.11.2009

⋆ Ensslin, K.
Time-resolved correlated electron transport through quantum dots
Fermions 2009, International conference ”From Correlated Electrons to Cold Atoms”, Obergurgl, Austria, 13.10.2009

⋆ Ensslin, K.
Graphene quantum dots
Workshop on Advanced Nanodevices and Nanotechnology (ISANN2009), Hawaii, USA, 29.11.2009

⋆ Erbudak, M.
Ordered oxide layers on decagonal Al-Co-Ni and icosahedral Al-Pd-Mn quasicrystals
16th Conference on Statistical Physics, Istanbul, Turkey, 26.6.2009

⋆ Erbudak, M.
Structure of surface oxides grown on the icosahedral Al-Pd-Mn quasicrystals
16th European Crystall. Meeting, Istanbul, Turkey, 21.8.2009

⋆ Erbudak, M.
Nanoepitaxy on quasicrystal surfaces
Seminar, Physikdepartement, METU, Ankara, Turkey, 22.12.2009

Felder, F.
Lead Salt Resonant Cavity Enhanced Detector with MEMS Mirror
NGS-14, 14th International Conference on Narrow Gap Semiconductors, Sendai, Japan, 13.07.2009

⋆ Filipp, S.
Probing entanglement of two-qubit states
Seminar invited by Alexandre Blais, Universite de Sherbrooke, Sherbrooke, QC, Canada, 01.07.2009

Filipp, S. (Poster)
Preparation and measurement of entangled states in circuit QED
Quantum Engineering, Centro Stefano Franscini, Monte Verita 224;, TI, Switzerland, 14.06.2009

Filipp, S.
Two-qubit tomography with joint dispersive read-out in circuit QED
APS March Meeting, Pittsburgh, USA, 16.03.2009

Filipp, S.
Generation and measurement of entangled two-qubit states in superconducting electronic circuits
Joint Annual Meeting of ÖPG,SPS and ÖGAA 2009, University of Innsbruck, Innsbruck, Austria, 02.09.2009

Fill, M.
IV-VI Mid-IR Tunable Lasers and Detectors with External Resonant Cavities
39. Freiburg Infrared Colloquium, Freiburg, Germany, 17.02.2009

⋆ Fink, J.M.
Quantum Optics Experiments with Multiple Qubits and Multiple Photons in Superconducting Electronic Circuits
TCM (Theory of Condensed Matter) seminar, Cavendish Laboratory, University of Cambridge, UK, 04.12.2009

⋆ Fink, J.M.
Quantum Optics Experiments with Multiple Qubits and Multiple Photons in Superconducting Electronic Circuits
MIDAS midterm research workshop, Capri, Villa Orlandi, Italy, 30.09.2009

Fink, J.M.
Exploration of the Tavis-Cummings Model with Multiple Qubits in Circuit QED
APS March Meeting, Pittsburgh, USA, 16.03.2009

Fink, J.M.
Multi-Photon Cavity QED with Superconducting Circuits
Quantum Engineering, Centro Stefano Franscini, Monte Verita 224;, TI, Switzerland, 14.06.2009

Fognini, F.
Formation of Self Assembled PbTe Quantum Dots in CdTe on Si(111)
NGS-14, 14th International Conference on Narrow Gap Semiconductors, Sendai, Japan, 13.07.2009

Francesco, C.
Neutron scattering investigation of the quantum disordered phase of $(C_5D_{12}N)_2CuBr_4$
Swiss Workshop on Materials with Novel Electronic Properties, Les Diablerets, Switzerland, 26.08.2009

Francesco, C. (Poster)
Neutron scattering investigation of the quantum disordered phase of $(C_5D_{12}N)_2CuBr_4$
The International Conference on Magnetism - ICM 2009, Karlsruhe, Germany 26.07.2009

Fragner, A.
Resolving Vacuum Fluctuations in an Electrical Circuit by Measuring the Lamb Shift
APS March Meeting, Pittsburgh, USA, 16.03.2009

⋆ Gasser, U.
Electron-phonon interaction in a double quantum dot
”Solid-State Based Quantum Information Processing: Physical Concepts and Materials Aspects”, Ludwig Maximilians University, Munich, Germany, 19.01.2009

Gasser, U.
Phonon driven current in a double quantum dot
Workshop at Quantum Systems and Technology (QSIT) Meeting 2009, Arosa, Switzerland, 21.01.2009

Gustavsson, S.
Time-resolved detection of single-electron interference
APS March meeting, Pittsburgh, USA, 16.03.2009

⋆ Güttinger, J.
Graphene Quantum Dots
International Conference on Excited State Processes in Elecronic and Bio Nanomaterials, Santa Fe, New Mexico, USA, 2.7.2009

⋆ Güttinger, J.
Transport Experiments on Graphene
Workshop on Transport in Interacting Disordered Systems, Ráckeve, Hungary, 31.8.2009

⋆ Güttinger, J.
Graphene Quantum Dots
International Conference on Transport in Interacting Disordered Systems, Ráckeve, Hungary, 2.9.2009

Güttinger, J.
Graphene Quantum Dots
QSIT Meeting, Passugg, Switzerland, 5.06.2009

Güttinger, J.
Graphene Quantum Dots
Graphene Tokyo 2009, Tokyo, Japan, 25.06.2009

Güttinger, J.
Electron-hole crossover in Graphene Quantum Dots
EP2DS, Kobe, Japan, 19.07.2009

Güttinger, J.
Time-resolved single-electron counting in a graphene quantum dot
EP2DS, Kobe, Japan, 19.07.2009

Güttinger, J. (Poster)
Electron hole crossover in graphene quantum dots
Graphene Meeting, Obergurgl, Austria, 02.03.2009

Güttinger, J. (Poster)
Electron hole crossover in graphene quantum dots
EP2DS, Kobe, Japan, 20.07.2009

Güttinger, J. (Poster)
Time-resolved single-electron counting in a graphene quantum dot
EP2DS, Kobe, Japan, 20.07.2009

Güttinger, J. (Poster)
Graphene quantum dots
Graphene Tokyo 2009, Tokyo, Japan, 25.06.2009

Hellmüller, S.
Shunt Stub Impedance Matching for Time-Resolved Charge Readout in a Quantum Dot
Quantum Systems and Technology (QSIT) Meeting 2009, Arosa, Switzerland, 21.01.2009

Hellmüller, S. (Poster)
Graphene single electron transistor with integrated charge detector
MNSP grand challenge 09

Helm, C.
Mentorierte Arbeiten in Physik
Weiterbildungsveranstaltung Praktikumslehrer, Emmetten, Switzerland, 10.02.2009

Hüfner, M.
Aharonov-Bohm effect in a side-gated graphene ring
XXIIIrd International Winterschool/Euroconference on Electronic Properties of Novel Materials, Kirchberg, Austria, 09.03.2009

Hüfner, L. (Poster)
Aharonov-Bohm effect in a side-gated graphene ring
XXIIInd International Winterschool on Electronic Properties of Novel Materials

⋆ Ihn, T.
Time-resolved charge detection and back-action in quantum circuits
Int. Conf. on the Electronic Properties of Two-Dimensional Systems (EP2DS), Kobe, Japan, July 2009

Ihn, T.
Using a double quantum dot as a mesoscopic detector
International Conference on Quantum Communication and Quantum Networking, Vico Equense, Italy, October 2009

Ihn, T.
Quantum point contact charge detectors and their back-action on double quantum dots
16th Int. Conf. on Electron Dynamics in Semiconductors, Optoelectronics and Nanostructures (EDISON16), Montpellier, France, August 2009

Ihn, T.
Graphene quantum dots
Int. Workshop and School on Solid State Based Quantum Information Processing, Herrsching, Germany, July 2009

Ihn, T.
Graphene Quantum Dots
Int. Conf. on Quantum Engineering, Ascona, Switzerland, June 2009

Ihn, T.
Single atom functionality in electronic devices: Quantum circuits with artificial atoms
Science beyond Fiction, The European Future Technologies Conference, Prague, Czech Republic, April 2009

Ihn, T.
Back-action of quantum point contact charge detectors
Int. Conference on the Science of Complexity, Eilat, Israel, March 2009

Ihn, T.
Electronic Transport in Graphene Nanostructures
Annual meeting of the German Physical Society, Condensed Matter Division, Dresden, Germany, March 2009

Ihn, T.
Back-action of quantum point contact charge detectors
Int. Symposium on Nanoscale Transport and Technology (ISNTT2009), Atsugi, Japan, January 2009

⋆ Joel, M.
Small Science at Large Scale Facilities
Inauguration lecture, ETH Zurich, Zurich, Switzerland, 10.03.2009

⋆ Joel, M.
Electronic and magnetic excitations of high-temperature cuprate superconductors probed by ARPES and neutron scattering
Colloquium, Bristol, UK, 12.03.2009

⋆ Joel, M.
Electronic and magnetic excitations of high-temperature cuprate superconductors probed by ARPES and neutron scattering
Colloquium, Birmingham, UK, 13.03.2009

⋆ Joel, M.
Nanotechnologie am Paul Scherrer Institut
Nanotechday Nordwestschweiz 2009, Aarau, Switzerland, 20.05.2009

⋆ Joel, M.
Surface Reconstruction and Band Folding in Underdoped YBCO Films
Martin Peter Colloquium, Geneva, Switzerland, 19.06.2009

⋆ Joel, M.
Neutron and Angle Resolved Photoemission Spectroscopy Studies of the Underdoped Regime of Cuprate Superconductors
Workshop on emergence of inhomogeneous phases in strongly correlated electron systems, Paris, France, 30.06.2009

⋆ Joel, M.
Surface Reconstruction and Band Folding in Underdoped $YBa_2Cu_3O_7$-Films
International Workshop on Strong Correlations and Angle-Resolved Photoemission Spectroscopy (CORPES), Zurich, Switzerland, 19.07.2009

Joel, M.
The dichotomy of the dispersion in the pseudogap phase of cuprates as studied by ARPES
International Workshop on Strong Correlations and Angle-Resolved Photo-emission Spectroscopy (CORPES), Zurich, Switzerland, 19.07.2009

Joel, M.
Neutron scattering investigation of the quantum disordered phase of $(C_5D_12N)_2CuBr_4$
MaNEP workshop, Les Diablerets, Switzerland, 26.08.2009

Kalb, W.
Oxygen-related traps in pentacene thin films: Energetic position and implications for transistor performance
March Meeting of the American Physical Society, Pittsburgh, USA, 18.03.2009

Kalb, W. (Poster)
Low-voltage organic transistors and inverters with ultra-thin fluoropolymer gate dielectric
Plastic Electronics Europe, Dresden, Deutschland, 26.10.2009

Kanter, J.
Various magnetic ground states linked to sodium ordering pattern via controlled cooling in Na_xCoO_2 (x = 0.75-0.85)
March Meeting of the American Physical Society, Pittsburgh, USA, 18.03.2009

Kanter, J. (Poster)
Switching Magnetic Transitions in Na_xCoO_2: Changing the Coulomb Potential Landscape by Defined Cooling
Manep Swiss Workshop on Materials with Novel Electronic Properties, Les Diablerets, Switzerland, 26.08.2009

Kanter, J. (Poster)
Switching Magnetic Transitions in Na_xCoO_2 Changing the Coulomb Potential Landscape by Defined Cooling
M2S-IX - 9th International Conference on Materials and Mechanisms of Superconductivity, Tokyo, Japan, 07.09.2009

⋆ Karpinski, J.
Single crystals of $LnFeAsO_{1-x}F_x$ (Ln=La, Pr, Nd, Sm, Gd) and $Ba_{1-x}Rb_xFe_2As_2$: growth, structure and superconducting properties
SMEC2009 Study of Matter at Extreme Conditions, Miami, USA, 28.03.2009

⋆ Karpinski, J.
Single crystals of MgB_2 and $LnFeAsO_{1-x}F_x$ (Ln=La, Pr, Nd, Sm, Gd): High-pressure growth, structure and superconducting properties
Seminar at ETH Crystallography Dept. HCI, Zürich, Switzerland,17.04.2009

⋆ Karpinski, J.
Single crystals of $LnFeAsO_{1-x}F_x$ (Ln=La, Pr, Nd, Sm, Gd) and $Ba_{1-x}Rb_xFe_2As_2$: growth, structure and superconducting properties
Seminar, Atom Institute, Technical University, Vienna, Austria, 25.05.2009

⋆ Karpinski, J.
Single crystals of $LnFeAsO_{1-x}F_x$ (Ln=La, Pr, Nd, Sm, Gd) and $Ba_{1-x}Rb_xFe_2As_2$: high pressure growth, structure and superconducting properties
Seminar, Institute of Low Temperature and Structure Research, Wroclaw, Poland, 27.05.2009

⋆ Karpinski, J.
Single crystals of $LnFeAsO_{1-x}F_x$ (Ln=La, Pr, Nd, Sm, Gd) and $Ba_{1-x}Rb_xFe_2As_2$: growth, structure and superconducting properties
ICMAT2009, International Conference o Materials for Advance Technologies, Singapore 23.06.2009

⋆ Karpinski, J.
Single crystals of $LnFeAsO_{1-x}F_x$ (Ln=La, Pr, Nd, Sm, Gd) and $Ba_{1-x}Rb_xFe_2As_2$: growth, structure and superconducting properties
VORTEX VI, Vortex Matter in Nanostructured Superconductors , Rhodes, Greece 17.09.2009

⋆ Karpinski, J.
Single crystals of $LnFeAsO_{1-x}F_x$ (Ln=La, Pr, Nd, Sm, Gd) and $Ba_{1-x}Rb_xFe_2As_2$: growth, structure and superconducting properties
Seminar, PSI, Villigen, Switzerland, 09.10.2009

⋆ Karpinski, J.
Investigations of basic properties relevant for applications on single crystals of new FeAs based superconductors
EU-Japan Experts Workshop on Novel Superconducting Materials, Brussels, Belgium, 10.11.2009

Karpinski, J.
Single crystals of $LnFeAsO_{1-x}F_x$ (Ln=La, Pr, Nd, Sm, Gd) and $Ba_{1-x}Rb_xFe_2As_2$: growth, structure and superconducting properties
2009 Swiss Workshop on Materials with Novel Electronic Properties, Les Diablerets, Switzerland, 26.08.2009

Karpinski, J.
Single crystals of $LnFeAsO_{1-x}F_x$ (Ln=La, Pr, Nd, Sm, Gd) and $Ba_{1-x}Rb_xFe_2As_2$: growth, structure and superconducting properties
EUCAS 2009, European Conference on Applied Superconductivity, Dresden, Germany, 13.09.2009

⋆ Katrych, S.
A new allotropic modification of the cubic KOs_2O_6 pyrochlore
25 th European Crystallographic Meeting, Istanbul, Turkey, 16.08.2009

Katrych, S.
Stability range of the ternary W-phase in the system Al-Co-Ni
4th MRC Graduate Symposium, Zurich, Switzerland, 10.06.2009

Katrych, S.
Crystal structure studies of LnFeAs(O,F) and $(Ba,Rb)Fe_2As_2$ superconductors
Swiss Workshop on Materials With Novel Electronic Properties, Les Diablerets, Switzerland, 26.08.2009

Komijani, Y.
Spin-Splitting and Correlations in p-GaAs Quantum Point Contacts
Gordon Godfrey Workshop on Spin and Strong Correlations, Sydney, Australia 25.10.2009

Komijani, Y.
0.7 Feature in p-GaAs Quantum Point Contacts
ESF Fone Workshop, Madrid, Spain, 09.09.2009

Komijani, Y.
0.7 Feature in p-GaAs Quantum Point Contacts
SwissNano 2009 Workshop, Basel, Switzerland, 11.6.2009

Komijani, Y. (Poster)
Quantum Point Contacts and Quantum Dots in p-GaAs
Quantum Systems and Technology (QSIT) Meeting 2009, Arosa, Switzerland, 21.01.2009

Küng, B. and Gasser, U.
Back action of charge sensors on a double quantum dot
Workshop at Quantum Systems and Technology (QSIT) Meeting 2009, Arosa, Switzerland, 21.01.2009

Küng, B.
Quantum point contact noise detection with an on-chip sensor
QSIT lunch seminar, 02.04.2009

Küng, B. (Poster)
Noise-induced spectral shift measured in a double quantum dot
431. WE-Heraeus-Seminar ”Noise and Full Counting Statistics in Mesoscopic Transport“, Bad Honnef, Germany, 19.05.2009

⋆ Küng, B.
Semidoncutor nanostructures fabricated by AFM lithography
Euro AFM Forum 2009, Garching, Germany, 02.06.2009

Küng, B. (Poster)
Time-resolved charge detection with cross-correlation techniques
EP2DS, Kobe, Japan, 19.07.2009

Leek, P.J.
Generation of entangled states in circuit QED using sideband transitions
APS March Meeting, Pittsburgh, USA, 16.03.2009

Leek, P.J.
Coupling superconducting qubits using sideband transitions in circuit QED
Seminar by Dr. A. Marx, Walther-Meissner-Institut, Garching, Germany, 08.05.2009

Leek, P.J.
Coupling superconducting qubits using sideband transitions in circuit QED
Advanced Research Workshop Meso-09: Non-equilibrium and coherent phenomena at nanoscale, Chernogolovka, Russia, 11.06.2009

Leturcq, R.
Franck-Condon blockade in suspended carbon nanotube quantum dots
EP2DS, Kobe, Japan, 19.07.2009

Lucarelli, A. (Poster)
Charge dynamics of Co-doped $BaFe_2As_2$
Quantum Criticality and Novel Phases 2009 (QCNP09), Dresden, Germany, 04.08.2009

May, Ch.
Characterization of AFM defined quantum wires - simulation and experiment
Workshop at Quantum Systems and Technology (QSIT) Meeting 2009, Arosa, Switzerland, 21.01.2009

Miklos, C.
Electron-electron interactions in low dimensional hole systems
Seminar of the European Graduate Collage on Electron-electron Interactions in Solids, Rackeve, Hungary, 06.04.2009

Miklos, C. (Poster)
Electron-electron interactions in low dimensional hole systems
QSIT Meeting, Passugg, Switzerland, 02.06.2009

Miklos, C.
0.7feature in p-type quantum point contacts tuned by combined in-plane and top-gates
5th International School and Conference on Spintronics and Quantum Information Technology, Krakow, Poland, 07.07.2009

Miklos, C. (Poster)
Observation of excited states in a p-type GaAs quantum dot
14th International Conference on Modulated Semiconductor Structures, Kobe, Japan, 19.07.2009

Miklos, C. (Poster)
0.7feature in p-type quantum point contacts tuned by combined in-plane and top-gates
14th International Conference on Modulated Semiconductor Structures, Kobe, Japan, 19.07.2009

Miklos, C.
Evidence for Localization and 0.7 Anomaly in Hole Quantum Point contacts
International Conference on Quantum Phenomena at Nanoscale, Przno, Montenegro, 31.08.2009

⋆ Molitor, F.
Graphene Double Quantum Dots
Graphene Tokyo 2009, Tokyo, Japan, 26.06.2009

Molitor, F.
Transport gap in graphene constrictions
Graphene Week, Obergurgl, Austria, 02.03.2009

Molitor, F.
Transport gap in graphene constrictions
EP2DS, Kobe, Japan, 19.07.2009

Molitor, F. (Poster)
Graphene double quantum dots
EP2DS, Kobe, Japan, 19.07.2009

Molitor, F. (Poster)
Graphene double quantum dots
SwissNano Conference 2009, 11.-12.6.2009, Basel, Switzerland
Moll, P.
Electronic anisotropy near T$_c$ from magneto-transport in SmFeAs($O_{0.7}F_{0.25}$) and (Ba,Rb)Fe_2As_2 single crystals
APS March meeting, Pittsburgh, USA, 16.03.2009

Moll, P.
Low Anisotropy of SmFeAs(O,F) in High Magnetic Fields up to 65 T: promising for applications
Manep Swiss Workshop on Materials with Novel Electronic Properties, Les Diablerets, Switzerland, 26.08.2009

Moll, P. (Poster)
Exploring the Potential for Application of the New Iron Pnictide Superconductors in High Magnetic Fields
Joint Annual Meeting SPG-ÖPG-ÖGAA 2009, Innsbruck, Austria, 03.09.2009

Moll, P. (Poster)
High magnetic field scales and critical currents in SmFeAs(O,F) single crystals: promising for applications
M2S-IX - 9th International Conference on Materials and Mechanisms of Superconductivity, Tokyo, Japan, 07.09.2009

Moll, P. (Poster)
New Iron-Pnictide Superconductors : Prospect for Applications?
4th MRC Graduate Symposium, Zurich, Switzerland, 10.06.2009

Müller, Th. (Poster)
Counting Statistics with a Radio-Frequency Quantum Point Contact Charge Read-Out
"Microwaves for Condensed Matter Physics", Bad Honnef, Germany, April 2009

Pfuner, F.
Charge dynamics of Co-doped $BaFe_2As_2$
International Conference on Magnetism (ICM) 2009, Karlsruhe, Germany, 26.07.2009

Pfuner, F. (Poster)
Charge dynamics of $Ba(Fe_{1-x},Co_x)_2As_2$
2009 Swiss Workshop on Materials With Novel Electronic Properties, Les Diablerets, Switzerland, 26.08.2009

Preden, R. (Poster)
Correlated Counting of Single Electrons in a Nanowire Double Quantum Dot
WE-Heraeus-Seminar, Bad Honnef, Germany, 18.05.2009

Preden, R. (Poster)
Correlated Counting of Single Electrons in a Nanowire Double Quantum Dot
Quantum Systems and Technology (QSIT) Meeting 2009, Arosa, Switzerland, 21.01.2009

Quack, N.
Micro Gas Analyzer for the mid-Infrared
CTI Micro and Nano Technologies: The Impact of Miniaturization, Neuchatel, Switzerland, 11.11.2009

Quack, N.
Electrostatically Actuated Micromirror for Resonant Cavity Enhanced Detector
MicroNanoFabrication Annual Review Meeting, Lausanne, Switzerland, 19.05.2009

Rahim, M.
5 μm Vertical External Cavity Surface Emitting Lasers (VECSEL) for Spectroscopic Applications
TDLS 2009, 7th International Conference on Tunable Diode Laser Spectroscopy, Zermatt, Switzerland, 13.07.2009

Rahim, M.
Above Room Temperature Lead Salt VECSEL
NGS-14, 14th International Conference on Narrow Gap Semiconductors, Sendai, Japan, 13.07.2009

Schnez, S. (Poster)
Graphene Quantum Dots
Quantum Systems and Technology (QSIT) Meeting 2009, Arosa, Switzerland, 21.01.2009

Schnez, S. (Poster)
Electronic Transport in Graphene Quantum Dots
Graphene Week 2009, Obergurgl, Austria, 02.03.2009

Schnez, S. (Poster)
Electronic Transport in Graphene Quantum Dots
Quantum Engineering, Monte Verita (Ascona), 14.06.2009

Schiltz, G.
Studieren mit digitalen Medien - ein Status Quo
E-Learning Dossier (2009)

Schiltz, G.
Brücken-Podcast NET à la carte, ETH Zürich, 08.10.2009

Schiltz, G.
Nachlesung - ein synoptischer Podcast
Switch, Zürich, 16.10.2009

Schiltz, G.
Schreibanleitungen in der Physik
Forum wissenschaftliches Schreiben, 24.11.2009

Schiltz, G.
Keiner schreibt in das Forum! Wie motiviere ich Studierende zur Partizipation?
NET à la carte, ETH Zürich, 05.05.2009

⋆ Stampfer, C.
Graphene quantum dots
XXIIIrd International Winterschool/Euroconference on Electronic Properties of Novel Materials, Kirchberg, Austria, 09.03.2009

⋆ Stampfer, C.
Carbon nanomatrials: from nano electromechanical systems to quantum dots
215th Electrochemical Society (ECS) Meeting, San Francisco, USA, 25.05.2009

⋆ Stampfer, C.
Transport in Graphene Quantum Dots
Graphene 2009 Meeting, Centro de Ciencas de Benasque Pedro Pascual, Benasque, Spain, 04.08.2009

⋆ Stampfer, C.
Graphene Quantum Dots
INT-09-02b Program ”From Femtoscience to Nanoscience: Nuclei, Quantum Dots, and Nanostructures”, University of Washington, Seattle, USA, 13.08.2009

Stampfer, C.
Graphene and Nanotube Quantum Dots
Institute for Theoretical Physics, Vienna University of Technology, Vienna, Austria, 28.04.2009

Stampfer, C.
Electromechanical blockade in carbon nanotube quantum dots
WE-Heraeus-Seminar on ”Quantum Optics of Nano- and Micromechanical Systems”, Bad Honnef, Germany, 19.07.2009

Stampfer, C.
Carbon Nanomaterials: from Nano Electromechanical Systems to Quantum Dots
Seminar Talk, Phyiscs Faculty of the University of Vienna, Austria, 30.04.2009

Stampfer, C.
Graphene Quantum Dots
Seminar Talk, Department of Physics, University of Basel, Basel, Switzerland, 11.05.2009

Stampfer, C.
Electromechanical blockade in nanotube quantum dots
QSIT Seminar, ETH Zurich, Zurich, Switzerland (02.07.2009)

Stampfer, C.
Roadmap of carbon nanoelectronics
Workshop ”Tubes and Wires”, Julich, Germany, 06.10.2009

Stampfer, C.
Graphene Quantum Dots and Nanoribbons
Seminar Talk, Freie University Berlin, Berlin, Germany, 30.10.2009

Stampfer, C.
Graphene Quantum Devices
Seminar Talk, Institute of Bio and Nanosystems (IBN-3/4), Research Center Julich, Germany, 25.11.2009

Stampfer, C. (Poster)
Graphene quantum dots
SwissNano2009, Workshop on Nanocience, Basel, Switzerland, 11.06.2009

Stampfer, C. (Poster)
Electromechanical blockade in carbon nanotube quantum dots
438. Weheraus-Seminar on ”Quantum Optics of Nano- and Micromechanical Systems”, Bad Honnef, Germany, 19.07.2009

Steffen, L. (Poster)
Single Qubit Control in Circuit QED
Quantum Engineering, Centro Stefano Franscini, Monte Verita 224;, TI, Switzerland, 14.06.2009

⋆ Studer, M.
Gate-controlled Rashba spin-orbit interaction SFB Seminar - Spin Phenomena in Reduced Dimensions, University of Regensburg, Regensburg, 30.11.2009

Studer, M.
Spin-Orbit Interaction as a Tool for Spin Manipulation in Semiconductors
Workshop at Quantum Systems and Technologie (QSIT) Meeting 2009, Arosa, Switzerland, 21.01.2009

Studer, M.
Gate-controlled spin-orbit interaction in a parabolic GaAs/AlGaAs quantum well
Spintech, Krakau

Studer, M.
Electric-Field-Controlled Spin Dynamics in Nanostructures
Project Day Swiss National Science Foundation - KTI, Berne, Switzerland, 24.06.2009

Studer, M. (Poster)
Gate-controlled Spin-Orbit Interaction in a Parabolic GaAs/AlGaAs Quantum Well
Swiss Nano 2009 - Workshop on Nanoscience and NCCR Nano Annual Meeting, Basel, Switzerland, 11.06.2009

Studer, M. (Poster)
Gate-controlled Spin-Orbit Interaction in a Parabolic GaAs/AlGaAs Quantum Well
Int'l Conf. on Quantum Engineering, Monte Verita, Switzerland, 14.6.2009

Toni, S. (Poster)
Investigation of the pristine and Li-doped CaC_6 superconductor through the MuSR technique
Swiss Workshop on Materials with Novel Electronic Properties MaNEP annual meeting, Les Diablerets, Switzerland, 26.08.2009

Vaterlaus, A.
Physik und Ausbildung
Einführungsvorlesung an der ETH Zürich, 14.05.2009

Vaterlaus, A.
Können wir Atome sehen?
Lehrerweiterbildung an der Kantonsschule Wetzikon, 20.05.2009

Vaterlaus, A.
Können wir Atome sehen?
Lehrerweiterbildung an der Kantonsschule Oerlikon, 27.05.2009

Vaterlaus, A.
Moderne Physik an Mittelschulen
Vortrag am Forschungskolloquium der COHEP, 12.06.2009

Vaterlaus, A.
Moderne Physik an Mittelschulen
Vortrag an der Institutsvollversammlung des ZHSF (Zürcher Hochschulinstitut für Schulpädagogik und Fachdidaktik), 10.12.2009

Vaterlaus, A.
Schulexperimente (STM)
Weiterbildungsveranstaltung Praktikumslehrer, Emmetten, Switzerland, 10.02.2009

Vaterlaus, A.
E-Learning Projekt beschleunigte Bezugssysteme
Weiterbildungsveranstaltung Praktikumslehrer, Emmetten, Switzerland, 11.02.2009

⋆ Wachter, P. Cu, Pu and Fe high Tc superconductors: spin holes in antiferromagnetic clusters form nonmagnetic bipolarons
39èmes Journées des Actinides, La Grande Motte, France, 28.03.2009

⋆ Wallraff, A.
Photons, Qubits and Computers - A Quantum Mechanics Lab on a Chip
3rd International Vienna Symposium FUNCTIONAL MATTER, TU-Wien, Vienna, Austria, 06.11.2009

⋆ Wallraff, A.
Control and Measurement of Multiple Qubits in Circuit Quantum Electrodynamics
Quantum Measurement and Metrology with Solid State Devices, Physikzentrum Bad Honnef, Bonn, Germany, 01.11.2009

⋆ Wallraff, A.
Generating and Probing Entanglement in Circuit Quantum Electrodynamics (QED)
Scalable Quantum Computing with Light and Atoms organized by the European Integrated Project SCALA, Cortina d'Ampezzo, Italy, 15.02.2009

⋆ Wallraff, A.
Observing Vacuum Fluctuations in Electronic Circuits- or why Engineers may soon have to use quantum field theory
QSIT Seminar, Department of Physics, ETH Zurich, Zurich, Switzerland, 18.05.2009

⋆ Wallraff, A.
Quantenmechanik mit Schaltkreisen: Elektrische Atome, Photonen und Computer
Physik-Kolloquium der FU Berlin, Berlin, Germany, 12.06.2009

⋆ Wallraff, A.
Cavity Quantum Electrodynamics with Superconducting Circuits
Int. Workshop and School on Solid State Based Quantum Information Processing 2009, Herrsching, Germany, 28.06.2009

⋆ Wallraff, A.
Controlling Photons, Qubits and their Interactions in Superconducting Circuits
Quantum Computing, Control, and Communication Excellence Cluster of LMU, TU and MPQ Munich QCCC-Symposium, Bad Toelz, Germany, 10.10.2009

⋆ Wallraff, A.
Controlling Photons, Qubits and their Interactions in Superconducting Circuits
QIPC 2009 International Conference, Physics Department, Sapienza Universita di Roma, Rome, Italy, 21.09.2009

⋆ Wallraff, A.
Exploring the Interactions of Microwave Photons and Superconducting Qubits in Circuit Quantum Electrodynamics
Atoms, Cavities and Photons, College de France, Paris, France, 10.09.2009

⋆ Wallraff, A.
Circuit Quantum Electrodynamics
SCALA SUMMER SCHOOL, Cargese, France, 17.08.2009

⋆ Wallraff, A.
Cavity Quantum Electrodynamics with Superconducting Circuits
International Workshop and School on Solid State Based Quantum Information Processing 2009, Herrsching, Germany, 28.06.2009

⋆ Wallraff, A.
Zero, One, Two, and Many Photons: Cavity QED in Superconducting Circuits
Nobel Symposium on qubits for future quantum computers, Chalmers, Gothenburg, Sweden, 25.05.2009

⋆ Wallraff, A.
Measuring the vacuum, single and multiple photons in microwave frequency quantum optics experiments with superconducting circuits
Microwaves for Condensed Matter Physics Physikzentrum Bad Honnef, Bad Honnef, Germany, 05.04.2009

⋆ Wallraff, A.
Photons, Qubits and Computers - A Quantum Mechanics Lab on a Chip
73. Annual Meeting of the DPG and DPG Spring Meeting of the Condensed Matter Division, Dresden, Germany, 22.03.2009

⋆ Wallraff, A.
Controlling Photons, Qubits and their Interactions in Superconducting Electronic Circuits
APS March Meeting, Pittsburgh, USA, 16.03.2009

Wallraff, A.
Controlling Photons, Qubits and their Interactions in Superconducting Circuits
CIFAR Meeting on Advances in the Experimental Realization of Quantum Computation, Banff, Alberta, Canada, 27.10.2009

Yamauchi, Y.
Nonequilibrium dephasing in ballistic interferometers
EDISON-16

Yamauchi, Y.
Size dependence of the dephasing of the Aharonov-Bohm effect in ballistic interferometers
International Symposium on Advanced Nanodevices and Nanotechnology, Hawaii, USA, 29.11.2009

Yamauchi, Y.
Observation of the ”lobe structure” in the ballistic interferometers
EP2DS, Kobe, Japan, 19.07.2009

Zheludev, A.
Magnetism of non-magnetic quantum magnets
Colloquium, Stuttgart, Germany, 12.10.2009

Zheludev, A.
Bosonic quasiparticles in quantum spin ladders
Seminar, München, Germany, 09.11.2009

Zheludev, A.
Magnetism of non-magnetic quantum magnets
Colloquium, Lausanne, Switzerland, 07.12.2009

Zheludev, A.
Bosons, Condensation and Glass in quantum spin ladders
SPG/OPG annual meeting, Innsbruck, Austria, 04.09.2009

Zheludev, A.
Spin liquid-to-helimagnet quantum phase transition
JUM@P, Villigen, Switzerland, 09.10.2009

Zhigadlo, N.
High pressure synthesis and single crystal growth of FeAs based superconductors
4th Materials Research Center (MRC) Graduate Symposium, ETH Zurich, Switzerland, 10.06.2009

Zhigadlo, N.
Exploratory synthesis and crystal growth of FeAs based superconductors
Swiss Workshop on Materials With Novel Electronic Properties (MaNEP), Les Diablerets, Switzerland, 26.08.2009

Zhigadlo, N.
High-pressure synthesis, single crystal growth and superconductivity of F substituted SmFeAsO
9th European Conference on Applied Superconductivity (Eucas 2009), Dresden, Germany, 13.09.2009

Zhigadlo, N.
High pressure synthesis and single crystal growth of FeAs based superconductors
9th International Conference on Materials and Mechanisms of Superconductivity (M2S), Tokyo, Japan, 07.09.2009

Zhigadlo, N.
Crystal growth of superconducting compounds under high pressure
6th International Conference ”Vortex Matter in Nanostructured Superconductors”, Rhodes, Greece, 17.09.2009

Zhigadlo, N.
Single crystals of FeAs-based superconductors: growth, structure and physical properties
I.F. Schegolev Memorial Conference ”Low-Dimensional Metallic and Superconducting Systems”, Chernogolovka, Russia, 11.10.2009

Zhigadlo, N.
Synthesis and Crystal Growth of Superconducting Compounds Under High Pressure
Seminar at AIST, Tsukuba, Japan, 03.08.2009

Zhigadlo, N.
Superconducting single crystals from high-pressure experiments
Seminar at NIMS, Tsukuba, Japan, 04.08.2009

⋆ Zogg, H.
Narrow band tunable resonant cavity enhanced detectors for 3 - 10 tm wavelength
11th European Symposium on Semiconductor Detectors, Wildbad Kreuth, Germany, 07.06.2009

⋆ Zogg, H.
Mid-infrared lead-chlacogenide VECSELs emitting up to above RT at 4-6 μm wavelength
LEOS 2009, 22nd annual Lasers and Electro Optics Society meeting, Belek-Antalya, Turkey, 04.10.2009

⋆ Zogg, H.
Mid infrared resonant cavity detectors and lasers with epitaxial lead-chalcogenides
EMRS, Warsaw, Poland, 14.09.2009

⋆ Zogg, H.
Lead chalcogenide mid-IR tunable lasers and narrow band detectors
AITA 10, 10th International Workshop on Advanced Infrared Technology and Applications, Florence, Italy, 08.09.2009

⋆ Zogg, H.
IV-VI Mid-IR Tunable Lasers and Detectors with External Resonant Cavities
Optics and Photonics, San Diego, CA, USA, 02.08.2009

⋆ Zogg, H.
Lead-chalcogenide VECSELs on Si and BaF_2 for 5 μm emission
Photonics West Solid State Lasers XVIII: Technology and Devices, San Jose, CA, USA, 25.01.2009

Zogg, H.
4.5 μm VECSEL (vertical external cavity surface emitting laser) at room temperature
SPG 2009, Innsbruck, Austria, 02.09.2009